

ULTRATHIN OXIDE FILMS AS TEMPLATES FOR MAGNETIC
NANOSTRUCTURES

by

Xumin Chen

A DISSERTATION

Presented to the Faculty of
The Graduate College at the University of Nebraska
In Partial Fulfillment of Requirements
For the Degree of Doctor of Philosophy

Major: Physics & Astronomy

Under the Supervision of Professor Axel Enders

Lincoln, Nebraska

December 14, 2012

ULTRATHIN OXIDE FILMS AS TEMPLATES FOR MAGNETIC NANOSTRUCTURES

Xumin Chen, Ph.D.

University of Nebraska, 2012

Advisor: Axel Enders

The study of ultrathin oxide film as templates for magnetic nanostructures is presented. The ultrathin oxide thin films are investigated for the surface morphology, electronic properties, surface terminations, and ferroelectric properties by the combination of various local and non-local surface science techniques. Ultrathin oxide films, only a few unit cells in thickness, have significant advantages over bulk oxides, such as atomically defined, unreconstructed and stoichiometric surfaces. The high structural quality makes them suitable templates for the fabrication of metal-oxide heterostructures with unprecedented interface quality. This is expected to enable the studies of fundamental interactions between the oxide and metallic adsorbates, such as the theoretically predicted magnetoelectric coupling based on interfacial Fe-Ti bonds. Two kinds of oxide films, BaTiO_3 and Cr_2O_3 , are discussed. Scanning tunneling microscopy is utilized to investigate their structure and electronic properties. Firstly, studies of magnetism of Fe nanoclusters deposited on BaTiO_3 by X-ray absorption and photoelectron spectroscopy demonstrate that the oxidization of Fe is largely suppressed by the molecular beam epitaxy growth at low temperature so that even isolated Fe atoms on the BaTiO_3 have significant magnetic moments. As a second example, the growth and

characterization of ultrathin chromia film are discussed. The thin chromia films exhibit highly ordered and atomically smooth surfaces. The electronic structure is locally explored with scanning tunneling spectroscopy, to resolve surface termination and polarization. The presented studies on the ultrathin oxide films are expected to advance the fundamental understanding of interface effects in multiferroics and may help improving magneto-electric effects. In a third example, the formation of magnetic Co nanoclusters on boron nitride nanotemplates is analyzed. The analytic models and Monte-Carlo simulations for the analysis of the coverage of Co clusters show that interactions between particles are the determining factor in template-assisted cluster deposition experiments. Growth models are discussed that include inter-cluster interaction to describe the layer formation and predict layer filling.

ACKNOWLEDGMENTS

I would like to thank the great aid of my advisor, Professor Axel Enders. When I first meet Axel about joining his group for my Ph.D. study about 5 years ago, I was highly impressed by his excitement and enthusiasm about the fabrication of magnetic nanostructures and investigation with state-of-art surface science technique—scanning tunneling microscopy. I also enjoyed the coffee time in the morning when we discussed both scientific and non-scientific topics. While my research life in the Axel group has been filled with both happiness and frustration, I never lose my confidence in research and always hold my love for the science.

Many thanks are given to Professor JaeSung Kim for productive collaboration in both barium titanate film measurement and the XMCD characterization of magnetism of Fe nanostructures. Great appreciation is also given to Professor Alexei Gruverman and his student, Haidong Lu, for performing the piezoresponse force microscopy (PFM) measurements on the BaTiO₃ films. Many thanks are also given to Professor Christian Binek for his helpful discussion about surface structure of chromia film. Many thanks are given to Professor Peter Dowben for detailed explanations for the XPS spectra.

I also want to extend my great thanks to many collaborators who helped in this study of metal-oxide system---Matthias Bode, Tiffany Santos, Nathan Guisinger, Anand Bhattacharya, Jan Honolka, Violetta Sessi, Sabrina Hoffmann, Ihor Ketsman, Seolun

Yang, Ji-Hyun Kim, Hyund-Do Kim, Ralph Skomski, Juan Colon and Ning Wu. In addition, I am indebted to all of my coworkers and labmates for their effort in operating and maintaining of our laboratory in my pursuit of these projects----Donna A. Kunkel, Sumit Beniwal, Justin Nitz, and Mark Plano-Clark. Special thanks is given to Geoffrey Rojas for making coffee for our group, fruitful discussions, and many American style jokes, which fulfills my research life with smiles.

Without the help and suggestion from all of above professors and colleagues, My Ph.D life will be much more difficult. I would like to say “谢谢” (Chinese word for thanks) to all of you. Last but not the least, I would like to thank my family: my parents Zhi Xiu Chen and Xixian Liao, for giving birth to me at the first place and supporting me spiritually throughout my life.

Table of Contents

Chapter 1—Introduction	1
Chapter 2— Experimental	6
2.1 Scanning tunneling microscope and spectroscopy	7
2.2 Scanning tunneling microscopy on oxide film	18
2.3 Experimental setup and sample preparation	27
2.4 XMCD data analysis at low Fe coverage.....	32
Chapter 3— Ultrathin BaTiO ₃ templates for multiferroic nanostructures.....	39
3.1 Introduction.....	39
3.2 Experimental aspects specific to these studies.....	42
3.3 Results and discussion	44
3.3.1 Surface structure studies with LEED & STM.....	44
3.3.2 PFM and dielectric properties.....	46
3.3.3 Polarization switching and detection with STM.....	48
3.3.4 Photoelectron spectroscopy and surface termination.....	53
3.4 Conclusions.....	60
Chapter 4—Growth and characterization of ultrathin chromia films	61
4.1 Introduction.....	61
4.2 Experimental aspects specific to these studies.....	63
4.3 Results and discussion	64
4.4 Conclusions.....	71
Chapter 5— Magnetism of Fe nanostructures on ultrathin BaTiO ₃ films	73
5.1 Introduction.....	73

5.2 Experimental aspects specific to these studies.....	<u>75</u>
5.3 Results and discussion	<u>77</u>
5.4 Conclusions.....	<u>88</u>
Chapter 6— Ordered layers of Co clusters on BN template layers	<u>89</u>
6.1 Introduction.....	<u>89</u>
6.2 Experimental aspects specific to these studies.....	<u>90</u>
6.3 Results and discussion	<u>92</u>
6.4 Conclusions.....	<u>98</u>
Chapter 7— Summary	<u>99</u>
Bibliography	<u>102</u>

List of Tables

Table 3.1 Fitting parameters and best-fit results of the photoelectron spectra	57
Table 5.1 Spin and orbital moments for 2ML and 4ML Fe clusters.....	87

List of Figures

Figure 2.1 Schematic operation principle of STM	7
Figure 2.2 Tunnel effect in one dimension.	8
Figure 2.3 Schematic band structure of the tunnel contact	11
Figure 2.4 Electronic structure of materials and their spectroscopy curves	13
Figure 2.5 Cobalt islands on Cu(111)	16
Figure 2.6 SP-STM measurement on the Cr(001) surface.....	18
Figure 2.7 Potential energy diagrams for STM junction	22
Figure 2.8 Schematically potential energy profiles in BaTiO ₃ film	24
Figure 2.9 Potential energy diagrams for STM on oxide surface	25
Figure 2.10 STM images of an Al ₂ O ₃ island on NiAl(110).....	27
Figure 2.11 The UHV systems for STM and preparation chambers	28
Figure 2.12 Omicron LT-STM	31
Figure 2.13 Raw XAS spectra of Fe impurities and background	34
Figure 2.14 Normalized XAS spectra of Fe impurities and background	35
Figure 2.15 The XAS spectra after Fe background subtraction.....	35
Figure 2.16 XAS spectra after removing the split at height energy region	36
Figure 2.17 XAS spectra and a two-step function	36
Figure 2.18 XAS spectra after subtracting the two-step function.....	37
Figure 2.19 Sum of XAS spectra and its integral	37
Figure 2.20 XMCD signal and its integral.....	38

Figure 3.1 The structure and the surface termination of bulk BaTiO ₃	41
Figure 3.2 RHEED images at different stages during the growth of BaTiO ₃	44
Figure 3.3 LEED patterns of BaTiO ₃ film	45
Figure 3.4 STM images and LEED patterns of BaTiO ₃ films	46
Figure 3.5 PFM measurements on 8 u.c. BaTiO ₃ films	47
Figure 3.6 PFM measurements on 13 u.c. BaTiO ₃ films	48
Figure 3.7 I-V curves measured on BaTiO ₃ films by STM	49
Figure 3.8 I-V curves measured on BaTiO ₃ films by C-AFM.....	52
Figure 3.9 Photoelectron spectra of BaTiO ₃	54
Figure 3.10 Photoelectron spectra of BaTiO ₃ and Cu near Fermi edge	58
Figure 4.1 Side view of a unit cell and spin structure of Cr ₂ O ₃	61
Figure 4.2 STM images of metal Cr clusters and chromium oxide film	64
Figure 4.3 XPS spectra of chromium oxide.....	65
Figure 4.4 STM image and dI/dV map of one chromium oxide island	67
Figure 4.5 Calculated surface structure and phase diagram for Cr ₂ O ₃	69
Figure 4.6 STM image and dI/dV map of another chromium oxide island.....	71
Figure 5.1 Buffer-layer assisted growth process.....	77
Figure 5.2 XPS spectra of Fe on BaTiO ₃ film	78
Figure 5.3 XAS and XMCD spectra of Fe impurities on BaTiO ₃ film.....	79
Figure 5.4 Hysteresis curves of Fe impurities on BaTiO ₃ film.....	81
Figure 5.5 Magnetic moments of Fe impurities on BaTiO ₃ film.....	82
Figure 5.6 STM images Fe clusters deposited by LBAG method	83
Figure 5.7 XAS and XMCD spectra of Fe clusters	85

Figure 5.8 XAS near L_3 -edge of Fe clusters	<u>86</u>
Figure 6.1 Co clusters on BN layer with repeat BLAG cycles	<u>91</u>
Figure 6.2 Models of the BN occupation.....	<u>95</u>

List of Symbols and Abbreviations

Abbreviation	Description	Definition
AFM	Atomic Force Microscopy	Page 3
APXPS	Angle-Resolved X-ray Photoelectron Spectroscopy	Page 28
BLAG	Buffer-layer assisted growth	Page 76
BN	Boron Nitride	Page 90
Cu(111)	Copper surface along the <111> direction	Page 15
DOS	Density of States	Page 11
dI/dV	the first derivative of tunneling current	Page 12
E_F	Fermi energy	Page 14
EELS	Electron Energy Loss Spectroscopy	Page 3
e	Electron charge	Page 10
GIXD	Grazing-incidence X-ray Diffraction	Page 3
IPES	Inverse Photo Electron Spectroscopy	Page 12
I_T	Tunneling current	Page 11
$J_>$	Tunneling current density in BaTiO ₃ film with an out-of-plane polarization	Page 24
$J_<$	Tunneling current density in BaTiO ₃ film with an into-plane polarization	Page 24
LDOS	Local Density of States	Page 12
LEED	Low Energy Electron Diffraction	Page 3
LHe	Liquid Helium	Page 29
LN ₂	Liquid Nitrogen	Page 30
LT-STM	Low-Temperature Scanning Tunneling Microscopy	Page 31
MBE	Molecular Beam Epitaxiary	Page 1
NC-AFM	Non-Contact Atomic Force Microscopy	Page 3
PED	Photo Electron Diffraction	Page 3
PES	Photoelectron Spectroscopy	Page 53

Abbreviation	Description	Definition
PFM	Piezo-response Force Microscopy	Page 41
PLD	Pulsed Laser Deposition	Page 1
STM	Scanning Tunneling Microscopy	Page 3
XPS	X-ray Photoelectron Spectroscopy	Page 3
STS	Scanning Tunneling Spectroscopy	Page 4
TER	Tunneling-Electro Resistance	Page 24
UHV	Ultra High Vacuum	Page 4
UPS	Ultra-violet Photoelectron Spectroscopy	Page 3
V	Bias voltage	Page 10
XAS	X-ray Adsorption Spectroscopy	Page 32
XMCD	X-ray Magnetic Circular Dichroism	Page 28
XPD	X-ray Photoelectron Diffraction	Page 3
ϕ	Work function	Page 9
ρ_t	Density of states of tip	Page 12
ρ_s	Density of states of sample	Page 12
P_t	Spin polarization of the tip	Page 17
P_s	Spin polarization of the sample	Page 17

Chapter 1

Introduction

Oxide films have attracted considerable interest for their fundamental and practical importance in catalysis, environmental science, ceramics, electronic devices, and material sciences [1, 2, 3]. The useful properties of ultrathin oxide films vary from ferroelectricity to antiferromagnetism, depending on the type of oxide. These properties can be controlled by external stimuli, such as electric-field control of polarization in ferroelectric BaTiO_3 films, which open new perspectives for the application in magnetoelectronics. Considerable progress has been made in the synthesis and characterization of the thin oxide films grown on substrates. The present interest in oxide ultrathin films is generated by several factors [4], including (a) advances in thin-film growth techniques for the fabrication of single terminated oxide interface on the atomic scale, such as pulsed laser deposition (PLD) and molecular beam epitaxial growth (MBE), (b) the availabilities of sophisticated characterization techniques, such as advanced spectroscopy and microscopy, and (c) electronic structure theory, which not only has great value in the interpretation of experiments but also in the prediction of new properties.

Thin oxide films have already found many applications. Oxide films of a few microns in thickness have been used as coating in aircraft engines to reduce fuel consumption, owing to their thermal insulating properties [5]. Oxide electronics is

another big field. SiO_2 films of a few nanometers thickness, an essential and probably unsurpassed material in the design of metal oxide field effect transistors, have been the basis of microelectronics [6]. A wealth of intriguing properties, including a two-dimensional electron gas, superconductivity and magnetism, emerge in systems composed of the band insulators LaAlO_3 and SrTiO_3 [7]. Significant attention has been paid to graphene oxide, including a solution-processable precursor for bulk production of graphene for products such as transparent conductors, chemical sensors, biosensor, polymer composites, batteries, and ultra-capacitors [8]. A growing interest is also devoted to a new generation of systems and devices based on ultrathin oxide films, such as tunneling magneto-resistance sensors [9], special coatings for energy-saving applications [10], ferroelectric ultrathin film capacitors [11], and solid-oxide fuel-cells [12]. Mechanical writing, in addition to electric writing, of ferroelectric polarization has been achieved in the ultrathin BaTiO_3 films [13]. Furthermore, metal-oxide heterostructures composed of ferromagnetic and ferroelectric materials show an interesting magnetoelectric effect, which allows the electric control of magnetic properties or magnetic control of polarization, utilizing the properties of flexoelectricity (the coupling between polarization and a strain gradient) [14]. One example is the electric field control of the exchange bias [15]. These many examples illustrate the importance of oxide thin films for advanced technologies. Thin oxide films are expected to become important for the development of future electronics and spintronics devices.

Important questions for fundamental research regarding ultrathin oxide films include, but are not limited to, the following [16,17,18,19]: How do the dielectric

properties scale with film thickness and structure size? How does the structure of oxide thin films compare to that of bulk? Is the stoichiometry reserved in the oxide thin films? As is often the case, the answers are not simple. Scientists have applied a broad diversity of surface science techniques to explore the structure and electronic properties of oxide thin films, such as low-energy electron diffraction (LEED) [20], photo-electron diffraction (PED and XPD) [21] and grazing-incidence X-ray diffraction (GIXD) [22] spatially averaging structural information and ultra-violet (UPS) [23] and X-ray photo-electron spectroscopy (XPS) [24], electron-energy-loss (EELS) [25] for their electronic properties. However, the above techniques integrate over large sample surface areas and have no spatial resolution, that is, non-local structure and electronic properties. Non-contact atomic force microscopy (NC-AFM) is commonly used for the investigation of local surface structure, but only with limited spatial resolution. The local electronic and magnetic properties of the sample cannot easily be obtained with NC-AFM. In addition, atomic force microscopy (AFM) measurements are mostly performed in air where surface can be contaminated.

The innovative component of this thesis is the application of scanning tunneling microscopy (STM) for the study of surface structure and electronic properties of the insulating oxide thin films. This is an experimental challenge since STM typically relies on electrically conducting samples. It will be shown here, for the first time, how to operate STM to obtain morphology, electronic information and dielectric properties of thin insulating oxide films, with unprecedented spatial resolution. Most films are grown and studied under ultrahigh vacuum conditions. However, it will be also shown how

defined and pristine surfaces of BaTiO_3 films can be re-established in ultrahigh vacuum (UHV) after a sample is transferred through air.

Three systems will be discussed as model examples: (1) ultrathin BaTiO_3 films without and with magnetic adsorbates, (2) ultrathin chromia films, and (3) metal clusters deposited on insulating templates. A combination of local and non-local surface scientific techniques, including STM/STS, LEED, XPS, and XMCD methods, are used to characterize the surface morphology, electronic properties of thin oxide films, as well as the magnetism of ferromagnetic clusters and films deposited on oxide thin films. Key results of this thesis are: (a) scanning tunneling microscopy and spectroscopy (STM/STS) measurements on the ultrathin BaTiO_3 films reveal that high quality surfaces can be recovered by post-preparation in UHV chamber after sample transfer through air; (b) the switching and detection of the polarization in BaTiO_3 films are achieved with STM; (c) growth strategies of metal overlayers that suppress the metal oxidation are identified; and (d) the surface of chromium oxide Cr_2O_3 is directly identified. Many of these results cannot be obtained with other scanning probe methods and surface science techniques. The pioneering aspect of this thesis therefore is that it expands current strategies to investigate thin oxide films by a very powerful method---thus far widely ignored---scanning tunneling microscopy.

This thesis is organized as follows: The experimental and theoretical foundation for the work in this thesis is presented in chapter 2. The growth and characterization of ultrathin BaTiO_3 films, such as surface morphology, dielectric properties, surface

termination, and the polarization switching and detection, are discussed in Chapter 3. The growth and surface structure of chromia, or Cr_2O_3 are presented in Chapter 4. Research presented in Chapter 5 builds on the result of chapter 3, by studying structure and magnetism of Fe nanostructures deposited on barium titanate films under various experimental conditions. Conjugated insulating layers as templates to achieve ordered magnetic nanostructures, in contrast to the random clusters distributions presented in Chapter 5, are discussed in Chapter 6.

Chapter 2

Experimental

The scanning tunneling microscope (STM) was invented by Binnig and Rohrer at IBM in 1981 in Zürich [26], for which they received the Nobel Prize in physics in 1986. It is a powerful tool for measurement of the structural, electronic, and magnetic properties on metallic surface, semi-conductors as well as insulating films [27]. It has ultimate atomic spatial resolution. It was used in the research reported this thesis to locally measure morphology and electronic properties at the same time on the same sample area, which allows us to investigate the correlation between surface structure features and electronic properties. This thesis also reports that the STM was applied to switch and detect the electric polarization in ultrathin ferroelectric films. The basic principles of STM and its application to oxide films will be reviewed, with focus on the topography measurements, point spectroscopy, and dI/dV map at the fixed bias voltage, where the dI/dV signal in the map is proportional to the conductance of the sample. Other applications of STM, not of primary interest to this thesis, include the measurements of electronic surface states [28], the Kondo effect on single adatoms [29], magnetic measurements [30], and work function measurements [31].

2.1 Scanning tunneling microscopy and spectroscopy

The basic principle of scanning tunneling microscopy is schematically shown in Fig. 2.1. The tunnel junction is formed by a sharp metallic tip and conductive surface in close proximity. The underlying principle of STM is the quantum-mechanical tunneling of electrons between the tip and sample surface across a vacuum barrier at small tip-sample distance. The metal tip is positioned precisely above the sample surface by a piezoelectric crystal. When the distance between metal tip and sample is sufficiently small ($<2\text{nm}$) and a bias voltage is applied between the sample and tip, electrons will cross the barrier between tip and sample with a finite probability because their wave functions overlap. A typical STM exhibits a lateral and vertical resolution of $\sim 0.2\text{ nm}$ and $\sim 1\text{pm}$, respectively. Hence, it can probe and control structures with atomic precision. STM can be used in various environments, such as under atmospheric and ultrahigh vacuum conditions, and the sample can even be immersed in liquid [32,33]. In addition, STM measurements are possible in a wide temperature range: from milli-Kelvin [34] up to several hundred Kelvin [35, 36].

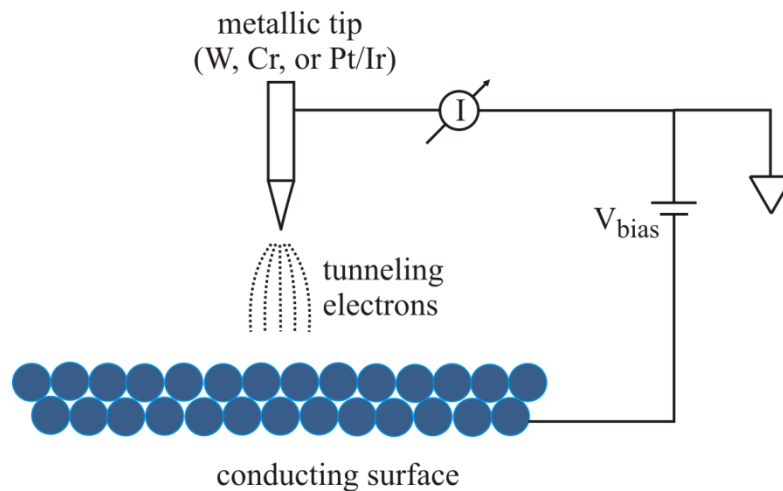


Fig. 2.1: Schematic operation principle of scanning tunneling microscopy

The basic physical principle of STM can be explained in the picture of electrons with energy E tunneling through a potential barrier of barrier height U in one dimension, as shown in Fig. 2.2. In classical mechanics, such a situation is described by

$$\frac{p^2}{2m} + U(z) = E \quad (2.1)$$

where m is the electron mass, E the electron energy and p the electron's momentum. When the electron has an energy larger than the barrier height, it has a non-zero momentum $p = \sqrt{2m(E - U)}$ and it can pass the barrier. However, when the electron energy is smaller than the barrier height, it will be reflected by the barrier, instead (Fig. 2.2(a)). This is a classically forbidden region.

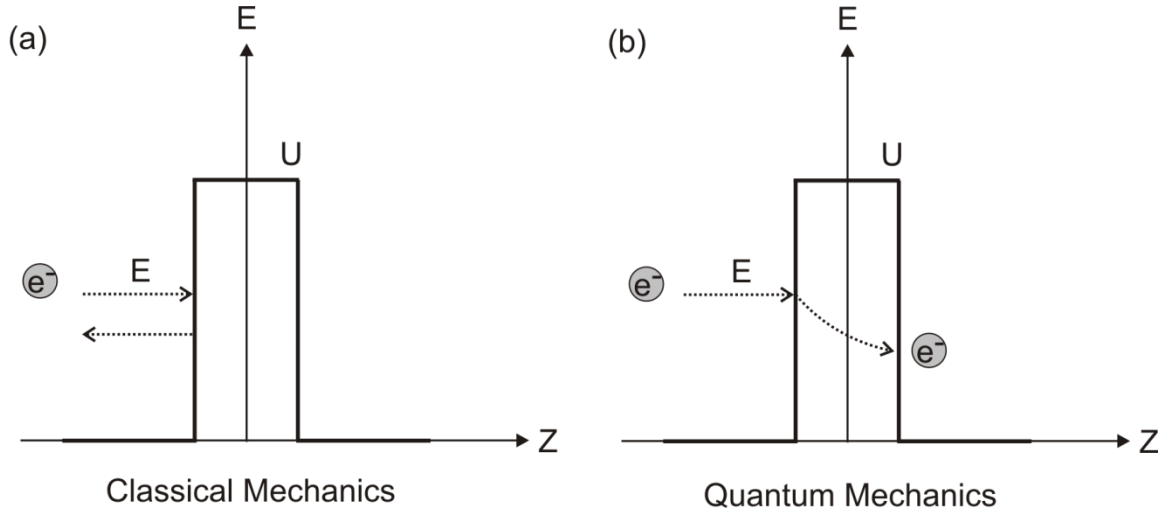


Fig. 2.2: Tunnel effect in one dimension. An electron of energy E is lower than the barrier height U . (a) in classical mechanics, the electron is reflected by the potential barrier and it cannot pass through the barrier; (b) in quantum mechanics, it has non-zero probability to penetrate the potential barrier.

In quantum mechanics, the electron is described by a wavefunction $\psi(z)$, which satisfies the Schrödinger equation,

$$-\frac{\hbar^2}{2m} \frac{d^2}{dz^2} \psi(z) + U(z) \cdot \psi(z) = E \cdot \psi(z) \quad (2.2)$$

Inside the barrier, which is the classically forbidden region, Eq. 2.2 has solutions

$$\psi(z) = \psi(0) \cdot e^{-kz} \quad (2.3)$$

where

$$k = \frac{\sqrt{2m(U - E)}}{\hbar} \quad (2.4)$$

is the decay constant. It describes a state of the electron penetrating through the barrier into the +z direction. The probability of observing an electron at a point z is proportional to $|\psi(0)|^2 \cdot e^{-2kz}$, which has a nonzero value in the barrier region, and thus has a nonzero probability to penetrate the barrier. Another solution is $\psi(z) = \psi(0) \cdot e^{kz}$, which describes an electron state decaying in the -z direction. It is usually too small to be significant.

Using electron-volt as the unit of the work function, and nm^{-1} as the unit of the decay constant, the numerical value for the decay constant is

$$k = 5.1\sqrt{\varphi} \text{ nm}^{-1}. \quad (2.5)$$

where φ is the work function of the target material in unit of electron volts with a typical value of 5 eV for metals. For example, a typical value of the decay constant k is 11.2 nm^{-1} for copper. According to Eq. 2.3 and 2.5, the tunneling current decays 9.4 times, almost an order of magnitude, per 0.1 nm of barrier width. This makes the STM very sensitive to

variation in tip-sample distance. For a typical atomic diameter of 0.3nm, the tunneling current changes by a factor of 1000! As a result, the tunnel current depends exponentially on the tip-sample separation, d , following:

$$I(d) = C \cdot e \cdot V \cdot \exp\left(-2 \frac{\sqrt{2m\phi}}{\hbar} d\right), \quad (2.6)$$

where C is constant, e charge of an electron, m mass of an electron, d the tip-sample distance and V the bias voltage.

Using this model, some basic features of the tunnel effect through a vacuum barrier can be explained, as shown in Fig. 2.3. At zero bias, the Fermi-levels of tip and sample are aligned and there is no tunneling current between tip and sample, as shown in Fig. 2.3(a). However, if the sample is biased by a negative voltage V with respect to the tip, this raises the Fermi level of the sample electrons with respect to the tip electrons by eV . Hence, electrons will flow from the occupied states of the sample into the empty states of the tip (Fig. 2.3(b)). If the sample is positively biased, the electrons flow in an opposite direction, that is, from the filled states of the tip into the empty states of the sample. Hence, both occupied and empty states of the sample can be probed. If the sample is a semiconductor, there exists a band gap between valence band and conduction band. At sufficiently large negative bias voltage, the electrons from both the valence band and conduction band can tunnel into the tip at large bias voltage (Fig. 2.3(c)).

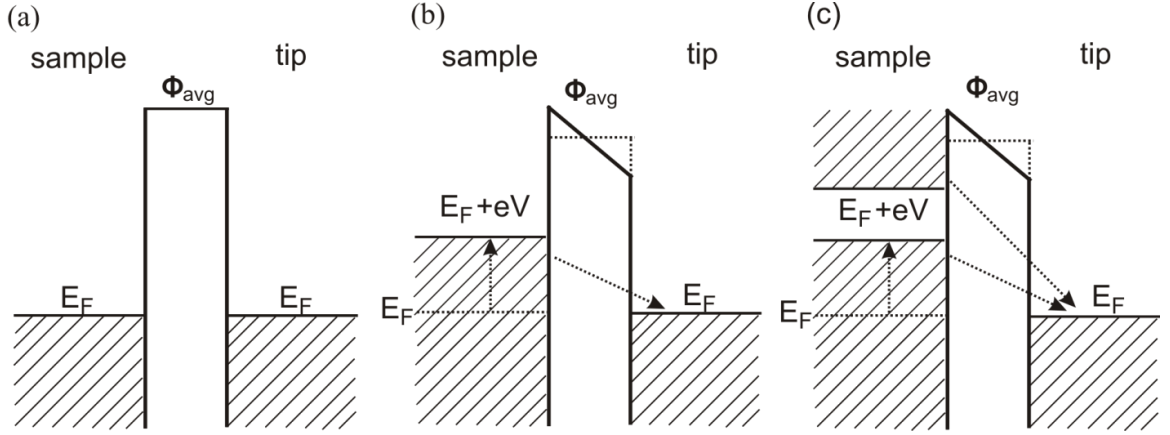


Fig.2.3: Schematic band structure of the tunnel contact formed by tip and sample in STM. (a) the Fermi levels of the metal surface and tip are aligned at zero bias, no tunneling current. (b) At the negative sample bias, the apparent Fermi level of the sample is shifted up to $E_F + eV$, tunneling current flows from sample to tip. (c) At the negative sample bias, ultrathin oxide film with a band gap structure, electrons could tunneling from both covalence band and conduction band of oxide film into tip.

In point scanning tunneling spectroscopy, the tunneling current is measured as a function of the bias voltage by deactivating the feedback loop to keep the tip-sample distance constant. These I-V curves provide the information that is the convolution of the tip density of states (DOS) and the sample DOS. At sufficiently low temperature, the elastic tunneling current (I_T), at low bias voltage can be approximated by the well-known Tersoff-Hamann model [37]:

$$I_T \propto \int_{E_F}^{eV} d\epsilon \rho_t(\epsilon) \rho_s(\epsilon + e \cdot V) \quad (2.7)$$

where ρ_t and ρ_s are the density of states of tip and sample, respectively. In this model, the tunneling current only depends on the DOS of the tip and the sample and the bias voltage. As a further simplification, the metallic tip DOS is assumed as constant, so that I_T reflects only the variations in the DOS of the sample.

The first derivative of the tunneling current I_T in Eqn. 2.7 with respect to bias voltage V yields the differential conductance, which is proportional to the sample local density of states (LDOS):

$$\frac{dI}{dV} \propto \rho_s(E_F + e \cdot V) \cdot \rho_t(E_F) \quad (2.8)$$

As previously discussed, the tip DOS is often assumed to be featureless, that is, approximately constant. In this case, the differential conductance, dI/dV , is proportional to the sample DOS [38,39]. Hence, in this spectroscopy method, where dI/dV is measured as a function of bias voltage, the local density of states of the sample is probed directly. It can, in principle, measure the LDOS of the sample at atomic resolution. It is a local spectroscopic tool for investigating the electronic structure, in contrast to ultraviolet photoelectron spectroscopy and inverse photoelectron spectroscopy (IPES) which can be used to evaluate the electronic properties over large surface areas.

The substrate can be a metal, a semi-metal, or a semiconductor with sufficient conductivity that is large compared to the conductivity of the tunnel junction. Oxide samples can only be studied if their conductivity is increased through experimental treatment or if a high bias voltage is applied to overcome the band gap of the oxide layer. In Fig. 2.4, the electronic structure of different materials and their possible I-V and dI/dV spectroscopy curves are illustrated. If the substrate is metallic, then the tunneling current depends linearly on the applied voltage when the tip-sample distance is constant. In a semi-metal, there is a very small overlap between the bottom of the conduction band and the top of the valence band; hence it has no band gap and a negligible density of states at

the Fermi level. In this case, the tunneling current will also depend linearly on the applied voltage similar to a normal metal, but the tunneling conductance is depressed around the Fermi level. The tunneling current at low bias voltage rather exhibits insulator behavior. In semiconductors and insulators, which both exhibit a band gap, the conductance for small bias voltage is practically zero. The width of the band gap is reflected by the width of the zone of zero conductivity in the dI/dV spectra. An onset of exponentially increasing tunneling current is observed when the bias voltage is larger than the band gap.

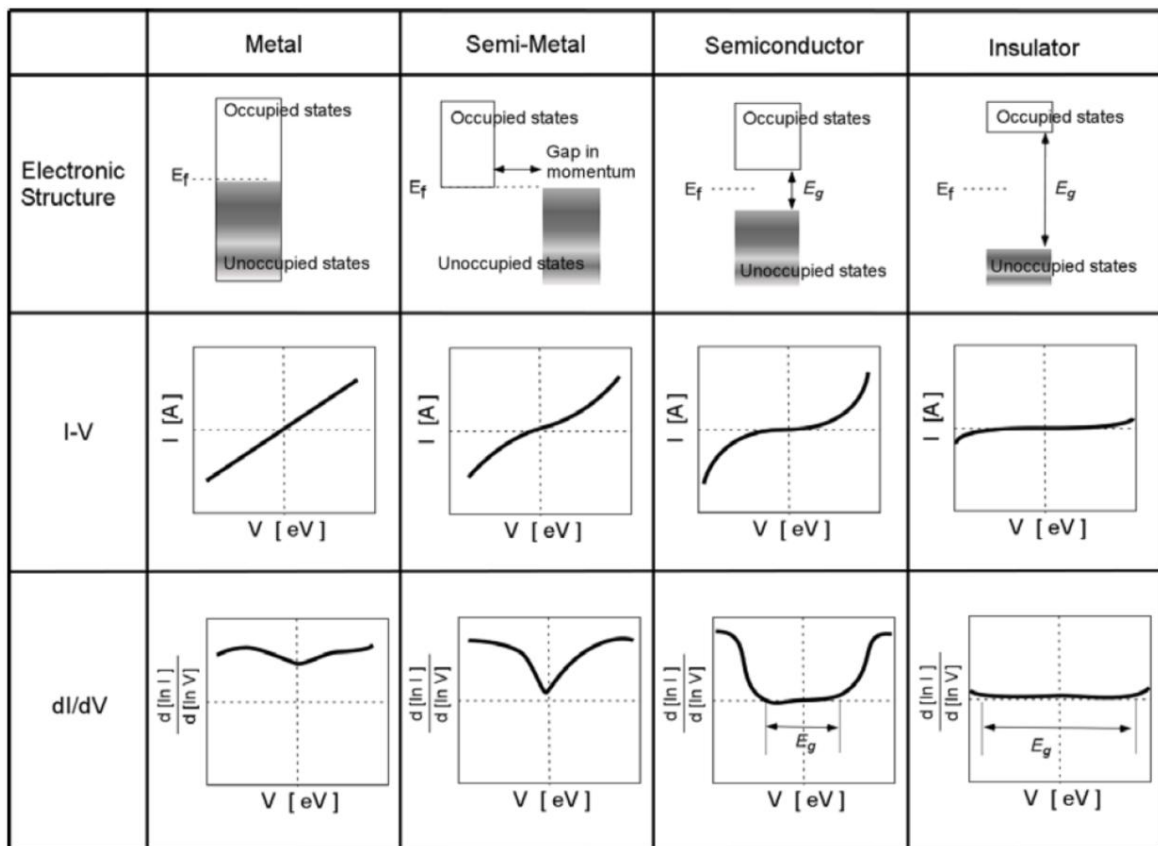


Fig. 2.4: Electronic structure of metal, semi-metal, semiconductor, and insulator and their possible I-V and dI/dV spectroscopy curves. Figure is reprinted from [40].

As shown in Fig. 2.4, the tunneling conductance, dI/dV , is material-dependent. For a metal, the dI/dV is nearly constant for the entire bias voltage ranges. For a semi-metal, the dI/dV has a characteristic minimum value around the Fermi energy (E_F) as described earlier. For semiconductors and insulators, the dI/dV has almost constant value close to zero inside the band gap due to the absence of the density of states and it has a step-like increase above the band gap.

A particular strength is the combination of STM and STS, which enable spatially resolved maps of the surface topography and the local differential conductivity at a fixed energy to be recorded simultaneously. Surfaces often exhibit interesting electronic properties, such as electronic surface states [28] and the Kondo effect of impurity ad-atoms [41], which can be conveniently studied with this local spectroscopy method. The surface morphology can be obtained from STM image and the electronic properties are determined from either I-V curves or direct dI/dV map measurements. The local tunneling spectra are recorded by measuring the differential conductance as a function of bias voltage at a constant sample-tip distance. The dI/dV is typically measured using a lock-in method, in which an *ac* voltage of magnitude of a few millivolt at a frequency above the feedback bandwidth is added to the applied bias voltage. The measured tunneling current will be modulated with the same frequency as the bias voltage modulation which will be measured with a lock-in amplifier. The output of the lock-in amplifier will be the sample conductance at that bias voltage. The I-V curves yield an integral measurement of the density of states in the probed energy window, and differential conductance dI/dV spectroscopy results in energy resolved information [37,38,39].

The spatial distribution of an electronic state can be obtained by measuring dI/dV maps at a fixed bias voltage. The dI/dV maps are obtained by recording the dI/dV signal via the lock-in technique simultaneously with constant-current images obtained with closed feedback loop scanning of the sample surface. The main advantage of this method is that the dI/dV map, in addition to the surface morphology, can also have an ultimately atomic resolution. As an example, the topography image and the dI/dV map of cobalt islands on a Cu(111) substrate obtained with a non-magnetic W tip are shown for comparison in Fig. 2.5. It is well known that Co islands are of double-layer height, exhibiting triangle shape with two different stacking sequences [42,43,44]. In Fig. 2.5 (a) the topography of the Cobalt islands is shown, while in Fig. 2.5 (b) the simultaneously recorded dI/dV map shows the well-known standing wave pattern due to the electron confinement. This quantum interference pattern is due to the finite lateral size [45,46,47] of the Co double layer and the scattering of *sp* majority electrons [43].

When both tip and sample are ferromagnetic, the tunneling current can also be sensitive to the spin of the tunneling electron---- a tunneling magnetoresistance effect. That can be used to map the local magnetization of the surface. The tunneling current depends on the relative alignment of the local magnetization of the tip and sample, as well as the spin polarization of the electronic states of tip and sample contributing to the tunneling current [48].

$$I_{SP}(V_0) \propto I_0 \left[1 + P_{tip} \cdot P_{sample} \cdot \cos(\vec{m}_{tip}, \vec{m}_{sample}) \right] \quad (2.9)$$

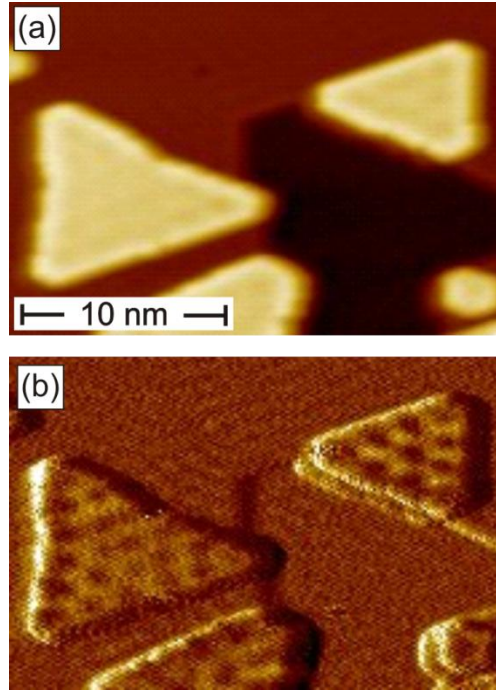


Fig. 2.5: Images of cobalt islands on Cu(111) taken by a non-magnetic W tip. (a) The topographic STM image of Co islands; (b) The simultaneously recorded dI/dV map. The STM image has been adjusted to enhance the brightness of Co islands and the dark region is the Cu terrace with an atomic step lower than the surface. The bias voltage is 0.3 V and the tunneling current is 1 nA. The image is taken after desorption of H_2 , following a procedure described in [49]. Sample temperature during imaging is 77 K.

where I_0 is the unpolarized (spin-averaged) tunneling current, P_{tip} and P_{sample} are the spin polarization of the tip and the sample, respectively. This equation considers that the tunneling current is spin-dependent only when both the tip and sample are magnetic and that the tunneling current is maximized when the spin direction in tip and sample are aligned in parallel. In principle, such spin-resolved magnetic structure measurement on magnetic sample can be imaged with atomic resolution [30,50].

Within the spin-polarized tunneling model, the differential tunneling conductance is given by:

$$\left(\frac{dI}{dV}\right)_{SP} \propto C \cdot \left[1 + P_{tip} \cdot P_{sample} \cdot \cos(\vec{m}_{tip}, \vec{m}_{sample})\right] \quad (2.10)$$

Therefore it is qualitatively clear that any change in the $\cos(\vec{m}_{tip}, \vec{m}_{sample})$ term leads to variation in the dI/dV spectroscopic data. In other words, now the tunneling conductance contains information on the local orientation of the sample magnetization direction relative to the tip magnetization, that is, it is spin-resolved. The contrast in so-recorded dI/dV map by a magnetic tip can thus reflect the spin orientation of the sample when the spin orientation of the tip is assumed to be constant.

Fig. 2.6 shows an example of SP-STM/STS measurements on a Cr(001) surface. The data are obtained with a bias voltage $V = -300\text{mV}$ and a tunneling current $I = 1\text{ nA}$ at a temperature of $T = 77\text{ K}$. The measurements were performed with an electrochemically etched bulk Cr tip. Similar measurements can be performed with magnetically coated W-tips [51]. The topographic image in Fig. 2.6(a) shows terraces, ascending from the lower left to the upper right edge of the image, separated by monatomic steps. The dI/dV signal reveals two distinctively different values of tunneling conductance for adjacent terraces due to the antiferromagnetic nature of the Cr(001) surface. Cr is a topological antiferromagnet, where each Cr layer shows ferromagnetic ordering while adjacent layers have opposite magnetization. The contrast in the dI/dV image is thus due to the opposite magnetic orientation of any two neighboring terraces [52].

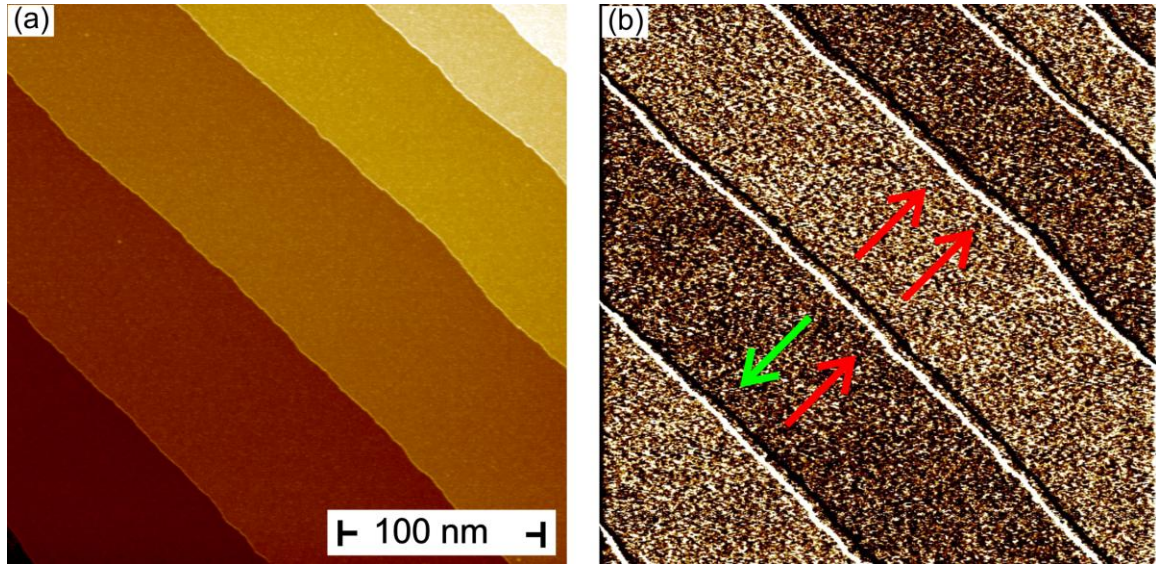


Fig. 2.6: The topography and spin-resolved dI/dV map on the Cr(001) surface taken with a bulk Cr tip. (a) The topographic image of Cr(001) surface shows atomical terraces that are separated by monatomic steps. (b) Spin-polarized dI/dV map records the dI/dV signal of the same surface region. Bias voltage is -0.3V and the tunneling current is 1 nA. The lock-in amplifier is set with 1ms time constant, 5 mV sensitivity, 10mV at 5.190 KHz Sine modulation.

2.2 STM on oxide film

Several standard techniques of surface science have already been explored for the investigation of thin oxide films, as discussed in Chapter 1. None of these techniques have spatial resolution; instead, they integrate over large sample surface areas. This can pose a problem when smallest structures are to be studied, where the above methods at best capture the ensemble properties. Local properties, such as local structure and morphology, electron quantization effect in ultra-small clusters [53] and size-dependent optical response [54] cannot be revealed in such ensemble measurements.

A goal of this thesis is to apply the strengths of STM/STS, as described in section 2.1, to study structure and electronic properties of thin oxide films. Oxides are usually not suitable for STM/STS experiments due to their low conductivity. However, oxide film can be studied with STM if one of the two following conditions is fulfilled:

- The resistance of the oxide film is still significantly lower than the tunnel resistance; that is, lower than $G \Omega$.
- The bias voltage is larger than the electronic band gap of the oxide.

Although challenging, the benefits of STM on oxide films are that structural, electronic and magnetic properties can be simultaneously achieved with an ultimately atomic resolution. The energy-resolved electronic properties can be obtained by point tunneling spectroscopy and the spatial distribution of electronic information can be mapped with tunneling conductance measurements, which are not available in Atomic Force Microscopy (AFM).

Typical experimental challenges during STM studies on oxide films are the following: The oxide films are characterized by a band gap around the Fermi level that inhibits tunnel processes at low bias. The small mobility of carriers in the oxide band might prevent efficient electron transport, even when the sample bias is higher (lower) than the conduction (valence) band onset in the insulator. Further, the metallic tip is often contaminated by the oxide surface. The standard *in-situ* tip modification approaches of STM do not work on the oxide surface. The oxidized tip needs to be flash-annealed up to 2000 K occasionally to remove the oxide layer. All of these factors make the STM measurement on oxide surface difficult and time-consuming.

STM measurements on oxide thin films are possible under the following experimental situations [55]: (1) There is a sufficient density of intrinsic carriers in the oxides even at low temperature enables electrons to follow between tip and oxide layers. Typical examples include transition metal oxides with narrow band gaps, such as V_2O_3 , Fe_3O_4 and ReO_3 [56]. (2) For ultrathin insulating films with 0.5-1 nm thickness, the electrons can tunnel through the oxide layer because the wave functions of the metal support sufficiently penetrate the oxide layer to overlap with the electronic states of the tip. The STM can operate at low bias voltage in this case [57]. (3) For oxide films with thicknesses up to 5 nm, electrons can be injected ballistically into the oxide conduction band and propagate towards the metal support in the tip-induced electric field. The STM needs to operate in the near field-emission regime (bias voltage = 5-10V) in this case [58]. (4) At elevated temperature, free carriers for electron transport are established by exciting a small number of valence electrons into the conduction band, hence providing sufficient oxide conductivity for STM measurement. This has successfully been achieved in several wide-gap insulators, including NiO at 500 K [59] and CeO_2 at 700 K [60]. The STM needs to operate at high temperature in this case. (5) A finite carrier concentration for electron transport is established by the doping of oxide films with defects (oxygen vacancies) or impurity atoms. This method is commonly used for semiconductors and narrow-gap oxides. For example, the creation of oxygen vacancies in TiO_2 or tin oxide [61] produces a large number of donor states in the band gap, enabling electrons to transport to the conduction band. (6) The adsorption of molecular species on certain oxides creates conductive surface states. For instance, the $ZnO(10\bar{1}0)$ surface is metalized after it is exposed to the hydrogen [62].

Specifics of STM studies of oxide thin films are now discussed, as follows, with reference to the potential energy diagram in figure 2.7 [63]. The diagrams for a metal (a) and an oxide surface (b) are compared in this figure. For STM on metallic substrates, the vacuum gap is represented by a trapezoidal potential energy profile. As discussed earlier, the electrons will tunnel through the vacuum from the filled states of the tip into the empty states of sample if the sample is biased by a positive voltage V with respect to the tip. The STM can operate at any bias voltage because of metallic nature of the conductive sample. This diagram has to be modified for STM measurements on insulating films on a metal substrate, as shown in Figure 2.7 (b), to include the band structure of the oxide layer. The oxide layer is also represented by a trapezoidal energy potential profile, but it has a large band gap and prohibits tunneling at low bias voltage. This effectively increases the width of the tunnel barrier by the thickness of the film, thus reducing the tunnel probability. At small bias voltage, the electrons will tunnel through both vacuum gap and oxide layer. Only if the bias voltage is sufficiently large will either the valence band or the conduction band of the oxide line up with the energy interval eV , thus contributing to the electron transport across the junction and eliminating the additional barrier provided by the film. The shape of the potential profile of the oxide layer will modify the tunnel current and so can then be studied experimentally. This includes the dependence of the barrier profile on the electronic polarization of a dielectric film [64]. Further, the electric field between tip and sample can be used to manipulate this polarization of the oxide film if the film is a dielectric, as shown in Section 3.3.3. Since the electric field from the tip is large at small tip-sample distance (about in order of 10^9 V/m), it is possible to switch the polarization direction in ferroelectric thin films with the

bias voltage applied on the STM tip. Thus, I-V curve measurements can both switch and detect the film polarization, as will be demonstrated in Section 3.3.3.

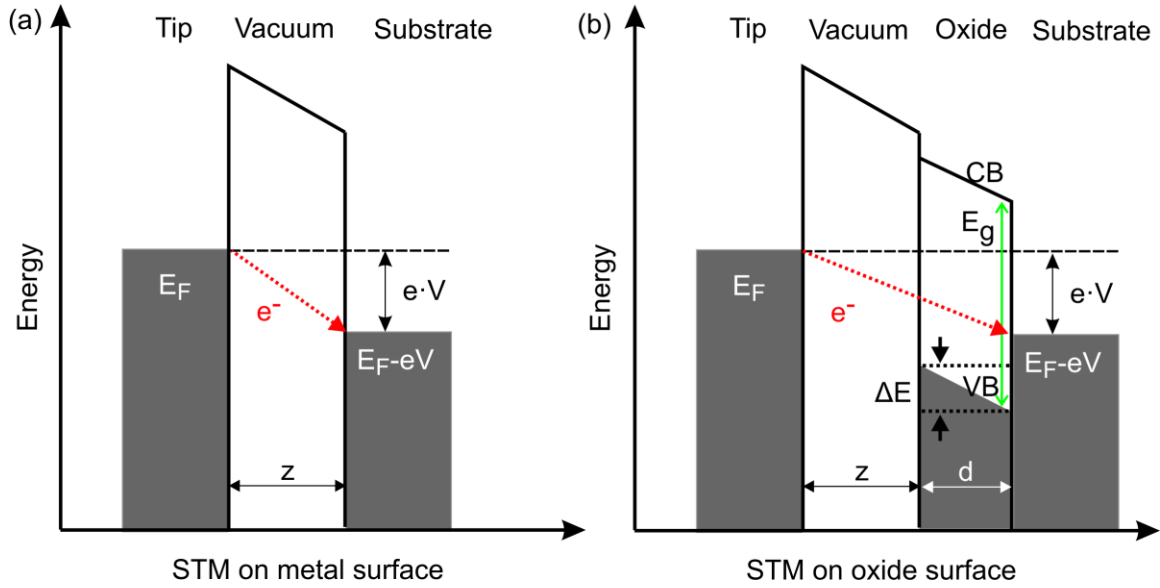


Fig. 2.7: Potential energy diagrams for STM on substrate with different electronic properties: (a) for metal sample, the electrons tunnel through the vacuum barrier represented by a trapezoidal potential energy profile; (b) for oxide surface, the electrons tunnel through both vacuum gap and oxide layer, where the oxide layer is also treated as a new trapezoidal potential energy profile, exhibiting a different effective vacuum barrier height. Due to the electric field from the tip, the oxide bands are shifted. E_g represents the band gap between valence band (VB) and conduction band (CB) in the oxide films, shown as a green line.

Using the Wentzel–Kramers–Brillouin (WKB) approximation, the typical current density in the Ohmic transport regime for a small bias voltage is given by [64]:

$$J = \frac{e^2}{\hbar} \frac{1}{2\pi d} \frac{\sqrt{2m\bar{\varphi}}}{\hbar} \cdot \exp\left[-2 \frac{\sqrt{2m\bar{\varphi}}}{\hbar} d\right] \cdot V, \quad (2.11)$$

where $\bar{\varphi}$ is the average potential barrier height, d the thickness of BaTiO₃ film, and V the applied voltage. Hence, the average potential barrier height determines the transport

properties and the tunneling electroresistance effect (TER) can be explained well in terms of the change of $\bar{\phi}$ with polarization reversal. When the barrier height changes by $\delta\phi$ from $\bar{\phi} - \delta\phi/2$ (high conductance state, current density $J_>$) to $\bar{\phi} + \delta\phi/2$ (low conductance state, current density $J_<$), the TER is given by:

$$TER = \frac{J_> - J_<}{J_<} = \exp\left[\frac{\sqrt{2m}}{\hbar} \frac{\delta\phi}{\sqrt{\bar{\phi}}} d\right], \quad (2.12)$$

assuming that $\delta\phi$ is small and $J_> \gg J_<$. The $J_>$ represents the tunneling current density when the polarization in BaTiO₃ film points out of the plane. The $J_<$ is the tunneling current density when the polarization in BaTiO₃ films points into the plane. The potential energy profiles of the BaTiO₃ film for opposite polarizations are schematically shown in Fig. 2.8. The basic idea is that polarization reversal leads to the change in effective barrier height in the tunneling junction; hence, the resistance between the tip and film is also changed.

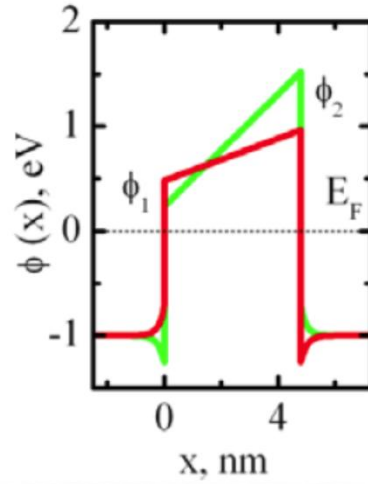


Fig. 2.8: schematically potential energy profiles in BaTiO₃ film for opposite polarizations. Red: polarization is into the plane; Green: polarization is out-of-plane. This Figure is reprinted from [64].

Another tunneling characteristic specific to oxide surfaces is the effect of voltage division in a tip-sample junction with an insulating oxide layer [65, 66]. The oxide materials are often unable to screen the electric field from the tip at their surface because the electron density in the oxide layer is very small. Hence, the applied bias voltage between tip and metal substrate will be dropped across both the vacuum gap and the oxide film. The fraction of the applied junction bias voltage will lead to a bending of the oxide bands [67]. The amount of band bending is determined by the thickness d and the dielectric constant ϵ_r of the oxide layer and can be estimated by modeling the tip-sample junction as a plate capacitor. When the oxide layer is treated as a dielectric medium inside the vacuum gap, the ratio of the voltage drop inside the oxide film to the total junction bias is given by: $\eta = \frac{d}{z\epsilon_r}$, where z is the tip-surface distance and d is the

film thickness. Hence, the band onsets in an thin oxide film will shift away from their

flat-band position E_0 by $\Delta E = E_0 \left(\frac{\eta}{1-\eta} \right)$, as shown in Figure 2.7 (b) [65].

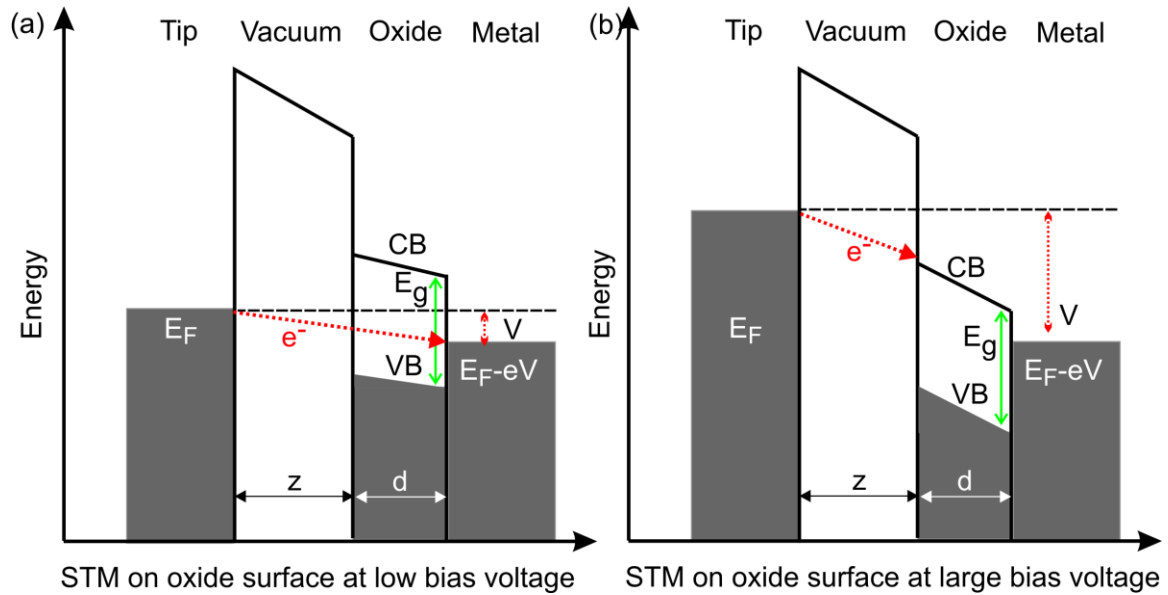


Fig. 2.9: Potential energy diagrams for STM on an oxide film on metal surface with small band gap. (a) At low bias voltage, the tunneling current is dominated by the electron transport between tip and metal substrate; hence, the STM images are determined by the DOS of the metal; (b) At large bias voltage, the tunneling current is dominated by the electron transport between tip and oxide bands; therefore, the STM images are determined by the unoccupied DOS of the oxide. E_g represents the band gap between valence band (VB) and conduction band (CB) in the oxide films, shown as a green line.

For the oxide material with mid-gap states or a small band gap, the tunneling behavior may be dominated by defects or metal-oxide interface since the electronic states in the valence band and conduction band of the oxide are not accessible at low bias voltage. In this case, the electrons can only tunnel between the tip and the metal support, as shown in Fig. 2.9(a). Now, the electron transport is governed by the DOS of tip and metal, while the oxide merely acts like a second tunnel barrier. Hence, the properties of

the metal-oxide interface determine the STM images taken with low bias voltage, that is, smaller than the band gap. Therefore, STM images show the topography at the metal-oxide interface. For example, G. Kresse et al have resolved the interface between a thin alumina film and the NiAl(110) support with STM, even though the interface layer is buried below three other oxide planes [68]. However, at higher bias voltages close to the onset of the conduction or valence gap, the electrons can tunnel directly into or out of oxide states. In Figure 2.9(b), the electrons tunnel from the tip into the conduction band of the oxide layer when the bias is above the band gap.

By the choice of the bias voltage, either the oxide layer itself or the surface underneath can therefore be imaged---something no other experimental methods can offer. This phenomenon can also be exploited to estimate the gap size of the oxide material [69,70,71]. The contrast of STM images of an oxide layer at different bias voltages due to the nature of availability of electrons is illustrated in the constant current topography images of an alumina film on NiAl(110) taken with low bias voltage and high bias voltage [72, 73] (see Figure 2.10). When the bias voltage is within the band gap of alumina, an Al_2O_3 island exhibits almost zero height with respect to the bare NiAl substrate, as shown in Fig. 2.10(a). In this case, the contrast represents the interface between alumina and NiAl. However, when the bias voltage is larger than the band gap, the same Al_2O_3 island shows an apparent height of 3.5 Å with respect to the bare NiAl substrate (Fig. 2.11(b)). The STM images in this case display the surface structure of the alumina island.

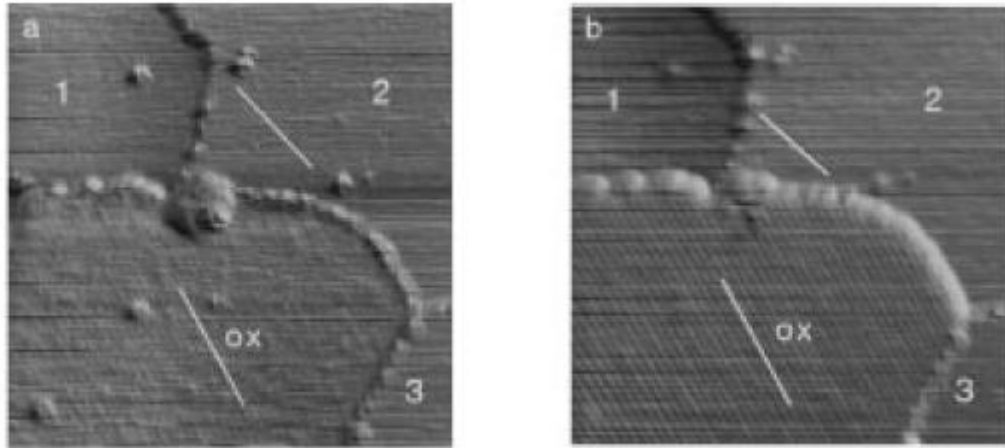


Fig. 2.10: STM images of an Al_2O_3 island on $\text{NiAl}(110)$. (a) when the bias voltage is well below the band gap ($U = 0.4 \text{ V}$), the STM image in oxide layer region reflects the interface of Al_2O_3 and the bare NiAl substrate; (b) when the bias voltage is beyond the band gap ($U = 4\text{V}$), the STM image in oxide layer region represent the morphology of an Al_2O_3 island [72]. Figure is reprinted from [72].

2.3 Experimental setup and sample preparation

In this thesis, scanning tunneling microscopy (STM) studies are performed to investigate the structural and electronic magnetic properties of ultrathin oxide films as well as surface supported nano-particles. Additional measurements on sample electronic structure and magnetic properties were performed in separate labs, including X-ray magnetic circular dichroism (XMCD) at the ID-08 beam line of the European Synchrotron Radiation Facility in Grenoble and at the 2A-beam line of Pohang Accelerator Laboratory in Korea, angle-resolved X-ray photoelectron spectroscopy (ARXPS) at University of Nebraska-Lincoln and LEED at the Center of Nanoscale Material in Argonne National Laboratory. All measurements presented in this work were performed under ultrahigh vacuum (UHV) environment, which typically refers to a base

pressure $<10^{-10}$ Torr. All STM experiments were performed on *in-situ* prepared samples in a multi-chamber UHV system, which is described in the following. The UHV system is composed of two chambers: a preparation chamber and a STM chamber. All samples preparation was done in the preparation chamber before the sample was transferred under UHV to the STM chamber for further investigation with STM.

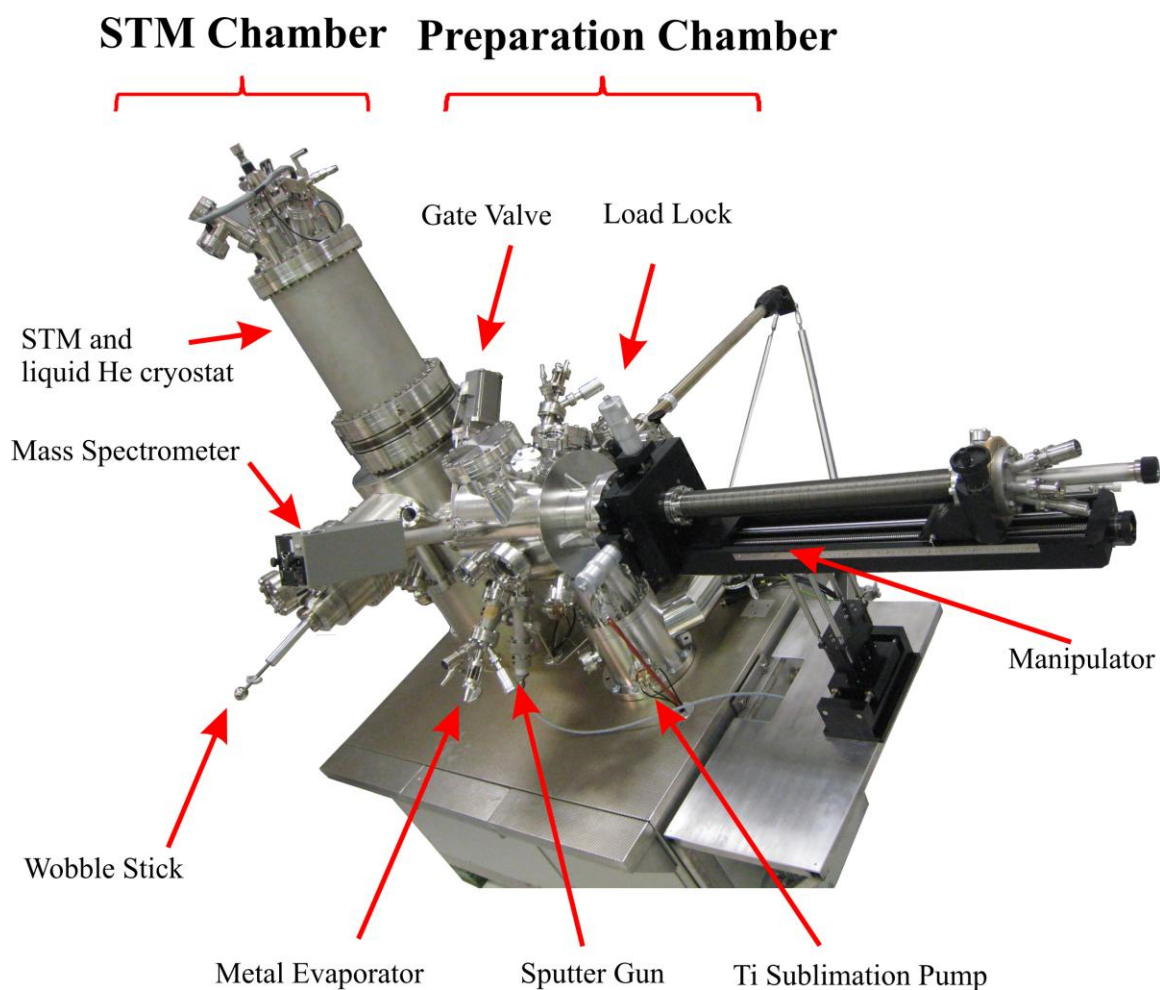


Fig. 2.11: The UHV system. The preparation chamber combines standard tools for sample preparation: sputter gun, e-beam heater in the manipulator, leak valve for different gas use, metal evaporators, mass spectrometer, and gate valve. The STM is mounted in the STM chamber together with a bath for cryostat. The STM can be operated at 4.2 K, 77 K and room temperature. The base pressure of the UHV system is about 10^{-11} Torr.

Fig. 2.11 illustrates the Omicron ultra-high vacuum system used for most of the STM research in this thesis. The UHV environment is achieved by pumping the system using a four-stage pumping system (mechanical pump, turbo pump, ion pump and Ti sublimation pump) and a 36-hour baking-out procedure at 410K. The base pressure after bakeout is typically 3×10^{-11} Torr.

The preparation chamber combines the following tools for sample preparation:

- Omicron EFM3 metal evaporators, for the MBE growth of metal films and nanostructures, such as Cr, Fe, Co, Cu, Ag;
- Omicron sputter gun ISE 10, operated with the following parameters: 1000V ion energy, 10 mA emission current, 10 μ A target current, 4×10^{-6} mBar Ar;
- Sample manipulator, allowing for annealing the sample up to 2000K with e-beam heater and cooling the sample down to 35 K with liquid helium (LHe). It also includes a separate reception for STM tip preparation by ion sputtering, annealing and thin film deposition. A thermocouple near the sample on the manipulator measures the temperature of the sample during annealing or cooling;
- A quartz microbalance, attached at the head of manipulator, for calibrating the evaporation rate of the metal evaporators;
- A fast entry load lock, for loading and unloading sample to and from the UHV chamber;
- A quadrupole mass spectrometer, used for residual gas analysis;

- A leak valve for gas inlet into the chamber, including argon gas for sputtering process, oxygen gas for oxidizing the metal clusters, and xenon gas for buffer layer assisted growth.

The STM chamber consists of the following components:

- Bath cryostats for cooling the STM stage at $T = 4.2$ K with liquid helium, at 77K with liquid nitrogen (LN_2) and at room temperature (300K) with no filling;
- The STM, suspended on springs during measurement with eddy current noise cancellation system;

Sample transfer from the preparation chamber to the STM chamber can be performed while the sample is being cooled, using the wobble stick and sample manipulator. If necessary, the sample will not warm up above 60 K during transfer.

Sample preparation

A typical cleaning process for a single crystal metal substrate, such as Cu(111) and Ag(111), is performed by repeated cycles of argon ion sputtering and annealing. Cu(111) substrates are cleaned by repeated cycles of Ar^+ sputtering and annealing at 700K. The sputtering parameters are 1,500V energy, 10 mA emission current, 10 μA target current at 6×10^{-6} mbar Ar partial pressure. Sample heating is performed at 66% of the melting point ($T = 700\text{K}$) to anneal sputter damages. The metal evaporator enables us to deposit metal on the sample. Thin metal films are deposited on the clean substrate at substrate temperature between 35 K and 300 K. After preparation, the sample is transported into the STM stage. At the base pressure inside the STM, the sample will stay

sufficiently clean for 1-3 days. The low temperature scanning tunneling microscopy (LT-STM) can be operated at three different temperatures, including room temperature (300K), liquid nitrogen temperature (77K) and liquid helium temperature (4.2K) [74]. The bath-cryostat design for the cooling system has a liquid helium holding time of up to 50 hours without refilling so it provides extremely low drift and high stability for long-term sample measurement. STM tips can be prepared by flash heating to 2000 K *in-situ* using a home-built tip annealing station.

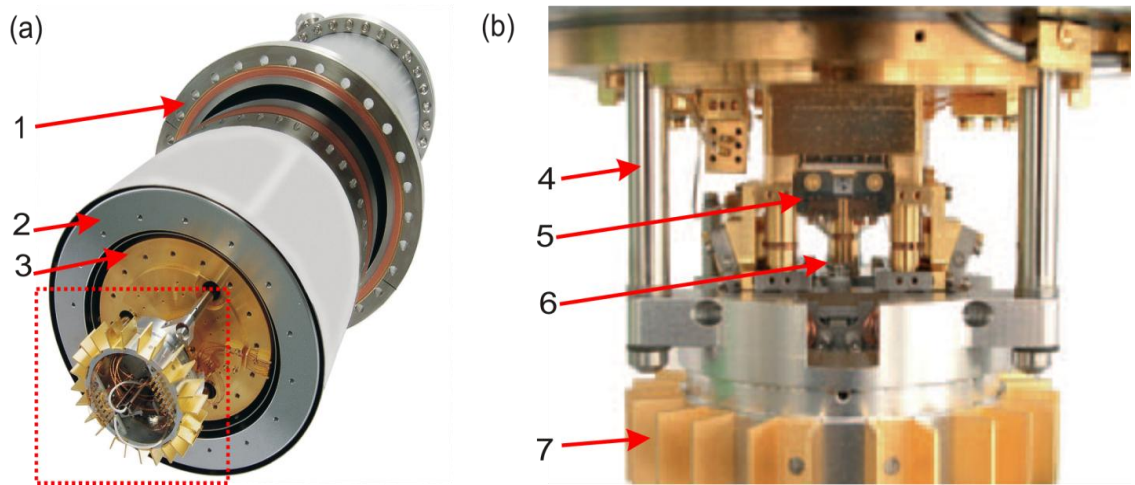


Fig. 2.12: Omicron LT-STM. (a) Overview of STM stage. (b) Side view of STM stage. (1) LT-STM UHV chamber, (2) LN₂ bath cryostat (silver), (3) bottom cold plate of the LHe bath cryostat (gold), (4) suspension springs holding the STM, (5) side-view of sample reception, (6) top of scan piezo with STM tip, (7) eddy current damping. This figure is reprinted from [74].

STM design

The design of LT-STM is shown in Fig. 2.12 [74]. The LT-STM is mounted to a large bath cryostat consisting of a LHe tank and an outer LN₂ tank for thermal isolation. The STM is mounted to a cold plate at the bottom of the LHe tank with suspension

springs. The suspension springs further reduce mechanical vibrations from coolant boil-off. There are two positions for the STM stage: cool-down position and measurement position. In the cool-down position, the STM stage is pulled against the cold plate for fast cool-down; in the measurement position, the STM stage is suspended in the eddy current damping system suspension springs. After the sample temperature becomes stable, the stage is released from the cool-down position to the measurement position for high-performance STM/STS measurements. The sample plate stays inside the sample holder with sample surface pointing downward. The tip of the STM, underneath the sample, is mounted on top of a piezo crystal and can be positioned laterally by x and y coarse drive motion within a range of ~ 5 mm.

In the work reported in this thesis, most STM images and dI/dV spectroscopic maps were obtained with non-magnetic W tips and so contain surface morphology and electronic information about the sample surface. The STM images have been processed by means of SPIP 5.1.1 software [75]. All the STM measurements were performed at LN_2 temperature.

2.4 Analysis of XMCD measurements

X-ray absorption spectroscopy (XAS) has been applied to study the magnetic properties on magnetic materials thanks to the development of intense sources of circularly polarized light with tunable energy, soft X-ray monochromators, and dedicated experimental endstations [76]. The XAS features, including lineshape and relative strength, provide fingerprint information of the chemical states of a given atom since the

X-ray transitions are localized on core holes at a certain atom and polarization dependent. The XMCD spectra are the difference of absorption spectra recorded for two opposite X-ray helicities---left and right circularly polarized light--and are sensitive to the magnetic properties of the sample. The intensity of XAS spectra for circularly polarized light depends on the orientation of the spin and orbital moment of the unoccupied electron states relative to the X-ray helicity. By applying the XMCD sum-rules [77,78,79], the spin and orbital magnetic moments for a given element could be quantitatively estimated. The sum rules can be applied to study the magnetism of 3d elements.

The first sum rule [77] is used to determine the orbital moment of the sample:

$$m_{orb} = -\frac{4\int_{L_3+L_2} (\mu_+ - \mu_-)d\omega}{3\int_{L_3+L_2} (\mu_+ + \mu_-)d\omega} \times (10 - n_{3d}), \quad (2.10)$$

where μ_+ and μ_- are the absorption coefficient for left and right circularly polarized light, ω is the photon energy, and n_{3d} is the number of 3d electrons. L_3 and L_2 denote the absorption edges $p_{3/2} \rightarrow 3d$ and $p_{1/2} \rightarrow 3d$, respectively.

The second sum rule [78] helps determine the spin moment:

$$m_{spin} = -\frac{6\int_{L_3} (\mu_+ - \mu_-)d\omega - 4\int_{L_2} (\mu_+ - \mu_-)d\omega}{3\int_{L_3+L_2} (\mu_+ + \mu_-)d\omega} \cdot (10 - n_{3d}) \cdot \left(1 + \frac{7\langle T_z \rangle}{2\langle S_z \rangle}\right) \quad (2.11)$$

where $\langle T_z \rangle$ is the spin-quadrupole coupling term, which describes the asymmetries of the spin density distribution and can be determined by theory [80]. If this sum rule is used to determine the spin moment, one has to assume that $\langle T_z \rangle$ is zero or $\langle T_z \rangle$ must be known from other experiments or theoretically approximated.

Because of the limited escape depth of low-energy photoelectrons, typically several 10 to 100's of Angstroms, XAS measured in the total electron yield mode is inherently surface sensitive. Its sensitivity is sufficient for probing surface impurities at coverage as low as 0.01 ML. Its biggest strength is in determining element-specific magnetic properties. While the standard XMCD sum rules provide good estimation of the spin and orbital magnetic moments, the analysis of spectra at low coverage is a challenge since background effects in the signal become significant and must be carefully removed. Here, the XMCD data analysis procedure for very low coverage (down to 0.03 ML) is discussed. The procedure will be explained with the example of Fe impurities on a BaTiO₃ film.

Step 1:

The as-measured XAS spectra and Fe background spectra are taken from the recorded data, as shown in Fig. 2.13. In the XAS spectra, the total electron yield, proportional to the coefficient of absorption, are recorded as a function of photon energy for both left circularly polarized and right circularly polarized incident light. The Fe background spectrum is for the clean BaTiO₃ film.

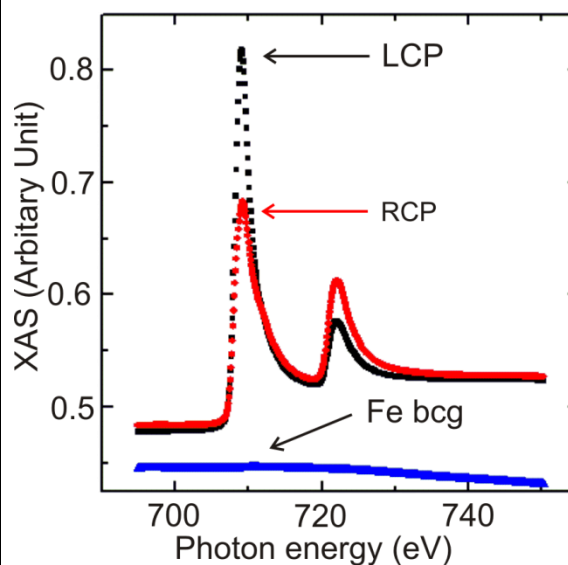


Fig. 2.13: As-measured XAS spectra of Fe impurities deposited on 13 u.c. BaTiO₃ film and the background signal taken on 13 u.c. BaTiO₃ film (Fe bcb). Red: right circular polarized light (RCP). Black: left circularly polarized (RCP) light. Blue: Fe background signal (Fe bcb).

Step 2:

XAS spectra and the Fe background are normalized to the signal at the pre-edge, which is at energies just before the L_3 adsorption peak. The derived spectra are shown in Fig. 2.14. The XAS spectra divided by the XAS signal at 705 eV yield the normalized XAS spectra. The normalized Fe background spectrum is derived in a same way.

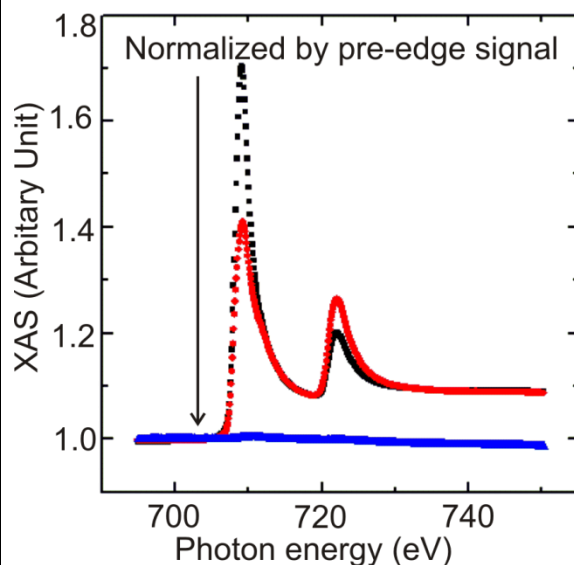


Fig. 2.14: Normalized XAS spectra of Fe impurities and the background signal with respect to the pre-edge signal at 705 eV.

Step 3:

The Fe background is subtracted from the normalized XAS spectra. The XAS spectra after Fe background subtraction is illustrated in Fig. 2.15. Sometimes, this will result in a split at high photon energy region in the spectra between opposite helicities, as shown in Fig. 2.15 inset.

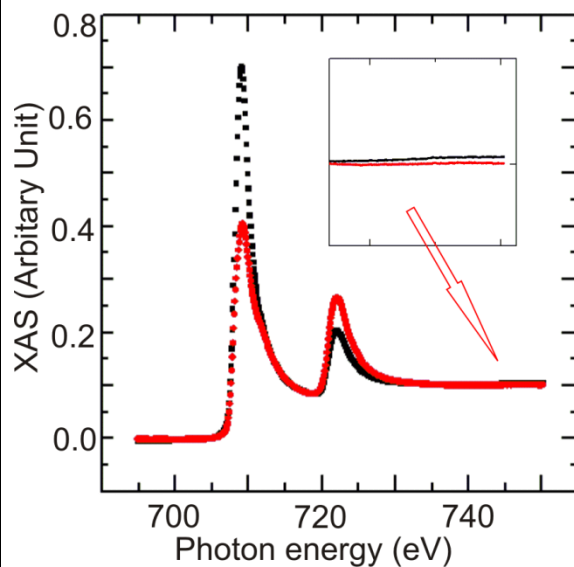


Fig. 2.15: The XAS spectra after Fe background subtraction. This process usually creates a split at high energy region, as shown in the inset.

Step 4:

The derived XAS spectra is subtracted by a line passing through point (705eV,0) in order to remove the split in the spectra at high photon energy part. The XAS spectra after removing the split in high energy region are shown in Fig. 2.16. The inset shows that there is no split at high energy region any more.

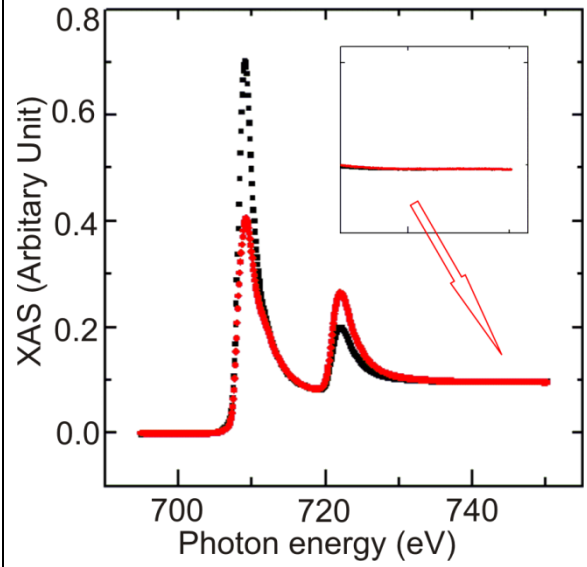


Fig. 2.16: XAS spectra after removing the split at height energy region. The inset shows that there is no split at high energy region any more.

Step 5:

A two-step function is given by:

$$\text{total step height} \times \frac{1}{6} \times \left[\left(2 + 2 \frac{\tanh(x - x_3)}{\text{width}} \right) + \left(1 + \frac{\tanh(x - x_2)}{\text{width}} \right) \right]$$

where total step height is the spectra intensity difference between high energy and low energy; x_3 and x_2 the photon energy at $L_{3,2}$ edges, and width the resolution of the beamline. The step function (blue line) is shown in Fig. 2.17.

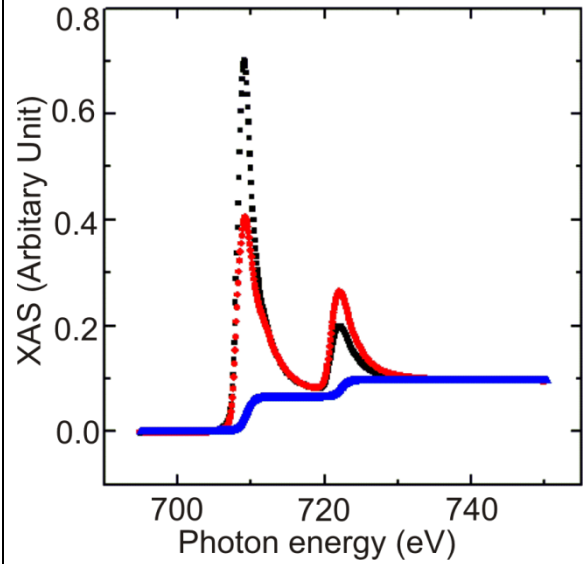


Fig. 2.17: XAS spectra and a two-step function

Step 6:

The XMCD spectra from the fourth step are subtracted by a two-step function derived from the fifth step. The XAS spectra after subtracting a two-step function are shown in Fig. 2.18. Later on, the XAS below 705eV will be ignored because this does not affect the final calculations of spin and orbital moments.

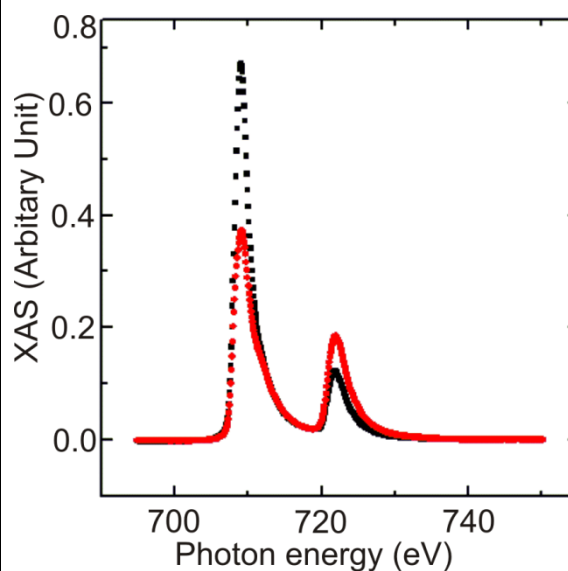


Fig. 2.18: XAS spectra after subtracting the two-step function

Step 7:

The sum of XAS spectra is calculated by adding XAS in parallel and antiparallel geometries together. The saturation value for the integral of the sum of XAS spectra is set as r , as shown in Fig. 2.19.

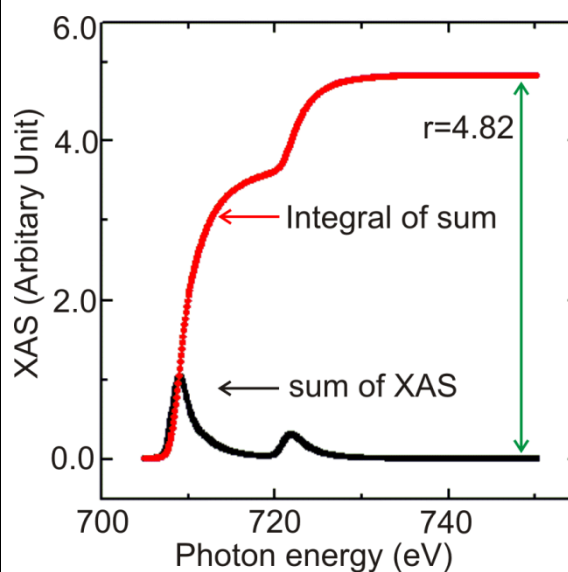


Fig. 2.19: Sum of XAS spectra and its integral, giving the value of r .

Step 8:

The XMCD signal is determined by taking the difference of plus and minus spectra, enabling p and q values to be determined from the integral of XMCD as shown in Fig. 2.20.

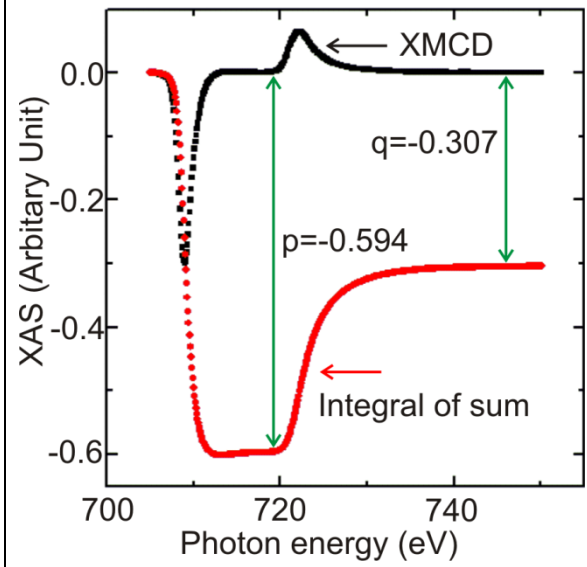


Fig. 2.20: XMCD signal and its integral, yielding the value of p and q .

Step 9:

XMCD sum rules are applied to obtain the orbital and spin magnetic moment, as well as the orbital/spin ratio, using the value of p , q and r .

$$m_{orb}(\text{per hole}) = -\frac{4q}{3r} = 0.08\mu_B$$

$$m_{spin}(\text{per hole}) = -\frac{6p - 4q}{r} = 0.48\mu_B$$

$$\frac{m_{orb}}{m_{spin}} = 0.17$$

In the bulk Fe, the number of $3d$ holes is 6.61. However, it is not known for the nanostructures. An estimate number of $3d$ holes is usually needed.

Chapter 3

Ultrathin BaTiO₃ templates for multiferroic nanostructures

3.1 Introduction

Barium titanate is a prototypical ferroelectric material. It has a perovskite structure. When the temperature is above 393K, it has a cubic structure with Ba at the corners, O in the face centers and Ti at the center of the unit cell. The effective charge positions for both positive and negative ions in the cubic structure are located at a single position, that is, the center of the unit cell and there is no electric polarization. However, when the temperature is lower than 393K, the center Ti ion shifts away from the original position and the oxygen stays at the same position, thus creating a spontaneous electric polarization. The spontaneous polarization can be manipulated by the application of an external electric field. The polarization has a hysteretic dependence on the electric field, meaning that there is a remanent polarization at zero applied fields. In the ferromagnetic material, the magnetism can be controlled by external magnetic field in a similar way. When the ferroelectric and ferromagnetic properties are combined in a two-phase multiferroic system comprising ferromagnetic metals and ferroelectric oxides, interesting and useful phenomena, such as magneto-electric effects [81,82], will arise. A model two-phase system exhibiting magneto-electric behavior, that is, the electric field dependence of the magnetization, is epitaxial Fe thin film on a BaTiO₃ substrate. The magnetic anisotropy of Fe depends strongly on the electric polarization of BaTiO₃, which has been

shown by Sahoo et al. [14]. The underlying mechanism here is a lateral strain exerted by the ferroelectric on the ferromagnet and the associated change of the magneto-elastic contribution to the total magnetic anisotropy. A second mechanism, different in nature but also leading to magneto-electric behavior, has been predicted recently for Fe/BaTiO₃ heterostructures [83, 84]. Characteristic for this new effect are modulations of the Fe - Ti bonds at the interface by the piezoelectric distortion of the BaTiO₃, resulting in changes of the effective magnetic moments of Fe and Ti atoms and the anisotropy. Another related example is magnetic tunnel junctions which are also based on metal-oxide interfaces [85]. Experimental investigation of any metal-oxide heterostructures depends critically on the quality of the oxide layer, since their performance is extremely sensitive to the chemical and structural properties of the interfaces. The realization of model structures or even devices exhibiting and exploiting the above effects is complicated by the experimental difficulty to grow metal-oxide interfaces of high interface quality.

Atomically smooth BaTiO₃ substrates are a requirement for the study of magneto-electric effects in all BaTiO₃-based heterostructures. The surface preparation of bulk samples is typically done by annealing them under ultrahigh vacuum or in hydrogen atmosphere to temperatures at around 1000 K [86,87,88]. It is found that both the atomic structure and the surface termination depend critically on the preparation conditions [88,89,90], as shown in Fig. 3.1. For example, following the black arrow in Fig. 3.1(b) by increasing the temperature from 1000 K to 1573 K, the surface undergoes a series of reconstructions with increasing Ti concentrations:

$$(2 \times 2) \rightarrow c(2 \times 2) \rightarrow (3 \times 1) \rightarrow (2 \times 2) \rightarrow (1 \times 1).$$

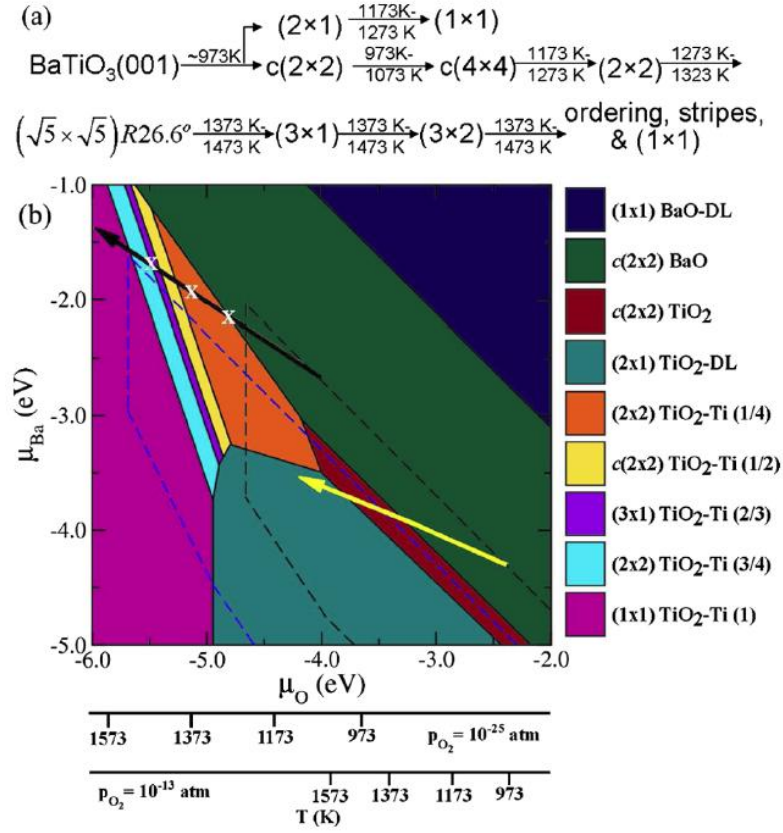


Fig. 3.1: the atomic structure and the surface termination of BaTiO_3 bulk is critically depended on the annealing temperature and oxygen partial pressure. (a) Observed phases at annealing sequence. (b) Computed surface phase diagram of single crystal BaTiO_3 at different annealing temperature and oxygen partial pressure [85]. Figure is reprinted from [85].

As alternatives to bulk BaTiO_3 substrates, ultrathin films of BaTiO_3 have been investigated recently [91,92]. The structural characterization has thus far been limited to reflection high-energy electron diffraction (RHEED) during growth [93, 94, 95, 96, 97], and low-energy electron diffraction (LEED) [92]. It is known from these studies that the films grow layer-by-layer only below a critical film thickness, which is of the order of 12 unit cells [98]. Characterization by piezoresponse force microscopy (PFM) [99] has demonstrated robust ferroelectricity in films as thin as 1 nanometer while even layers as

thin as one unit cell can be ferroelectric in BaTiO₃/SrTiO₃ superlattices (1 unit cell = 0.399 nm) [100]. However, comprehensive *in-situ* characterization with surface-sensitive methods to address the atomistic structure, surface termination, and dielectric properties are currently missing, but urgently needed, for the optimization of synthesis strategies and to achieve a significant performance increase in magneto-electric structures.

The present work aims at filling this gap. A comprehensive study of the structural, dielectric and electronic properties of BaTiO₃ films is presented, where BaTiO₃ films are only a few unit cells thin and grown on Nb-doped SrTiO₃ substrates. The properties are studied with a combination of local probe methods and electron diffraction and spectroscopy. It will be demonstrated that such films are superior to bulk BaTiO₃ substrates regarding the structural quality at the surface, while still showing the dielectric properties of bulk BaTiO₃ [101]. It is proposed that BaTiO₃ thin films are suitable for fundamental research and applications, such as for the study of magneto-electric effects and magneto-tunnel junctions.

3.2 Experimental aspects specific to these studies

The BaTiO₃ films were grown by molecular beam epitaxy (MBE) by co-evaporation of Ba and Ti from Knudsen cells and using pure ozone as the oxidizing agent. A steady flow of ozone gas was delivered to the growth chamber with the pressure maintained at 2×10^{-6} Torr. Prior to film growth, the Nb:SrTiO₃ substrates (0.2% Nb doping) were prepared with a buffered HF dip to obtain a TiO₂-terminated surface. The

substrate was heated in ozone to a growth temperature of 923 K and then cooled in ozone after film deposition. Each BaTiO₃ unit cell was deposited within ~50 seconds, followed by 30 seconds annealing (with Ba and Ti shutters closed). The deposition was monitored using reflection high energy electron diffraction (RHEED).

After growth, the samples were transferred through air into a separate ultrahigh vacuum systems for further studies with scanning tunneling microscopy (STM), low electron energy diffraction (LEED), photoemission spectroscopy (UPS), etc. STM images were obtained at 45 K using an Omicron variable temperature scanning tunneling microscope. Photoelectron spectroscopy was carried out at a soft x-ray beam line (3A1) at the Pohang Light Source, Korea. The UPS spectra presented here were taken with the sample kept at room temperature using a hemispherical electron energy analyzer with multichannel detector (Scienta). The energy resolution was 0.3 eV, as determined from the measured shape of Fermi edge of a Cu reference sample. The binding energy was measured with respect to the Fermi edge of Cu. Piezoresponse force microscopy (PFM) measurements were performed in air. During the PFM measurements, an external AC bias voltage was applied to the PFM tip, and the local piezoelectric response from the ferroelectric layer was measured. By scanning the sample surface while measuring the PFM response, a two-dimensional map of the piezoresponse amplitude and phase signals was generated, providing information on polarization magnitude and direction. For local hysteresis loop measurement, a DC offset voltage of controlled magnitude in the range of ± 6 Volts was applied to the tip. Dielectric properties, such as the coercive field and remanent polarization, were deduced from local hysteresis loops.

3.3 Results and Discussion

3.3.1 Surface structure studies with LEED and STM

This study focuses on BaTiO_3 films of 8 and 13 unit cell (u.c.) thicknesses. RHEED images taken along the $[100]$ axis of the pristine Nb:SrTiO_3 substrate surface prior to film growth, and of the 8 u.c. and 13 u.c. BaTiO_3 films are shown in Figure 3.2(a)-(c), respectively. Especially for the 8 u.c. film, spots rather than streaks were observed [Figure 3.2(b)], which is consistent with large, crystalline terraces at the surface of the films. Those spots broaden into streaks as the film thickness is increased to 13 u.c., indicating a gradual increase in surface roughness [Figure 3.2(c)].

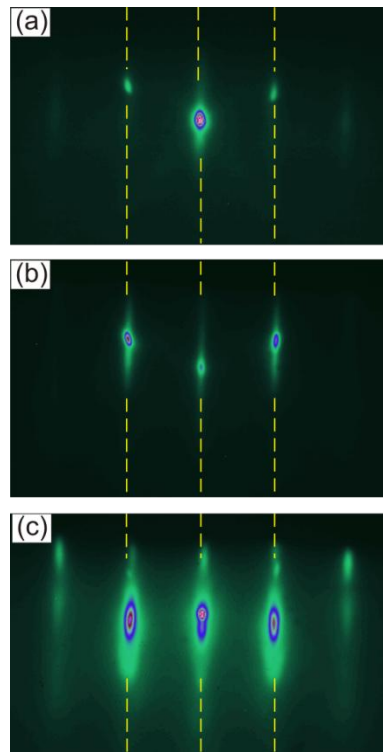


FIG. 3.2: RHEED images at different stages during the growth of BaTiO_3 by MBE. (a) pristine $\text{Nb-SrTiO}_3(100)$ substrate, (b) after growth of 8 unit cells of BaTiO_3 , (c) after growth of 13 unit cells of BaTiO_3 growth.

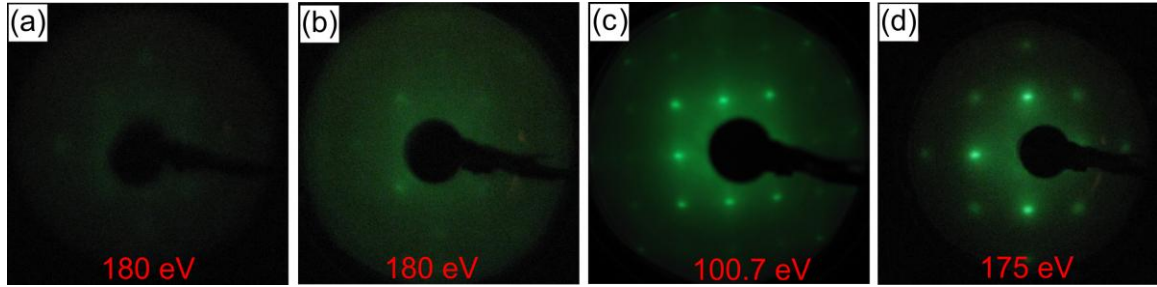


Fig. 3.3: LEED patterns of BaTiO₃ film at different annealing temperature at the 1×10^{-4} Torr oxygen for 20 minutes. (a) 423 K, (b) 573 K, (c) 723 K, and (d) 923 K, respectively.

The films were transferred through air into a separate STM UHV chamber after growth, where they were annealed in oxygen to recover ordered LEED diffraction patterns. While immediately after transfer no LEED pattern was observable, sharp (1×1) diffraction patterns could be established by thermal annealing at approximately 650 K under O₂ pressure of 3.75×10^{-7} Torr, using an oxygen dozer that faces the sample surface at a distance of ~ 5 cm. A weak LEED pattern becomes observable at an annealing temperature $T_a = 423$ K. With increasing temperature, the peak intensity and sharpness improves and the background intensity is decreased, as shown in Fig. 3.3. High-quality (1×1) diffraction patterns are observed at $T_a \sim 923$ K – 9730 K (Fig. 3.3(d) and Figure 3.4 inset). Further annealing is found to be detrimental to the diffraction image quality. STM images are taken at a sample temperature of 45 K on the films immediately after the annealing in oxygen. Flat terraces of approximate 100 nm width are found on the 8 u.c. film and the terrace step height corresponds to a single unit cell of BaTiO₃ (Figure 3.4). The 13 u.c. films also exhibit atomically flat terraces, albeit of much smaller size, typically ~ 10 nm. A height histogram analysis reveals that there are on average 4 open layers, as illustrated in Fig. 3.4 (d). This is consistent with the observation of streaks in the RHEED images and is attributed to the relaxation of epitaxial film strain.

It is concluded that crystalline films showing no detectable surface reconstruction in LEED and exhibiting terraces as wide as 100 nm in the case of the 8 u.c. film can be recovered after sample transfer through air.

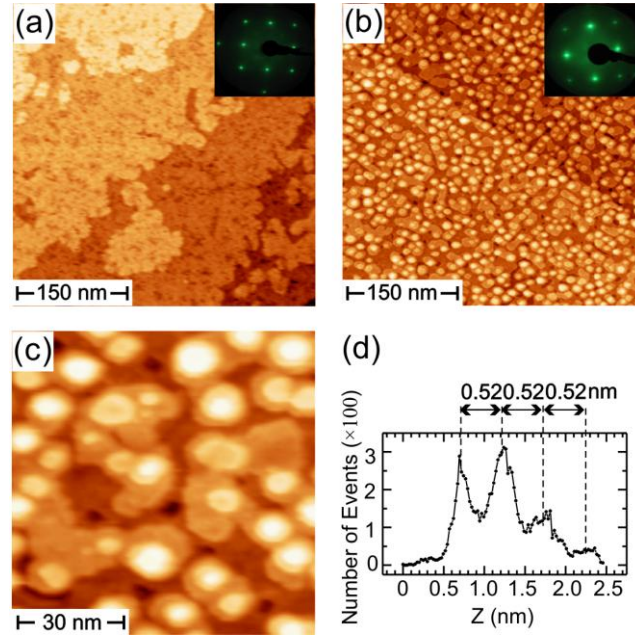


FIG. 3.4: STM images and LEED patterns of BaTiO₃ films on Nb-SrTiO₃. The thickness of the BaTiO₃ films is 8 unit cells (a) and 13 unit cells (b). (c) zoom-in STM image from part (b), (d) Histogram of height of the sample in (c). The LEED images are taken at 85 eV. Bias voltage is 2.7 V and tunneling current is 1 nA.

3.3.2 Piezoresponse Force Microscopy and Dielectric Properties

Resonance-enhanced piezoresponse force microscopy (PFM) measurements [64, 102] have been performed at room temperature on the BaTiO₃ films in air after extraction of the samples from the growth chamber, without further sample treatment. Prior to PFM characterization, bi-domain square-in-square polarization patterns have been generated in

the BaTiO₃ films by scanning the surface with an applied dc bias voltage of ± 4 V. The PFM phase and amplitude maps of the resulting patterns, together with local polarization hysteresis loops, are shown in Figure 3.5 for the 8 u.c. thin films. The amplitude signal in Figure 3.5(a) is a measure of the polarization magnitude, while the phase signals in (b) show the polarization direction. The hysteresis loops of the phase and the amplitude signals in (c, d) confirm the existence of remanent polarization, which can be reversed by applying electric fields larger than those corresponding to the measured coercive bias voltage of approx. 3.5 V. The visible asymmetry in the amplitude signal hysteresis loop for opposite polarization is due to differences in the interfaces on both sides of the BaTiO₃. Film boundaries and surface terminations, are known to result in the accumulation of surface charges, which influence the symmetry of the observed PFM loops. Identical results were obtained from the 13 u.c. thin film and are shown in Fig. 3.6.

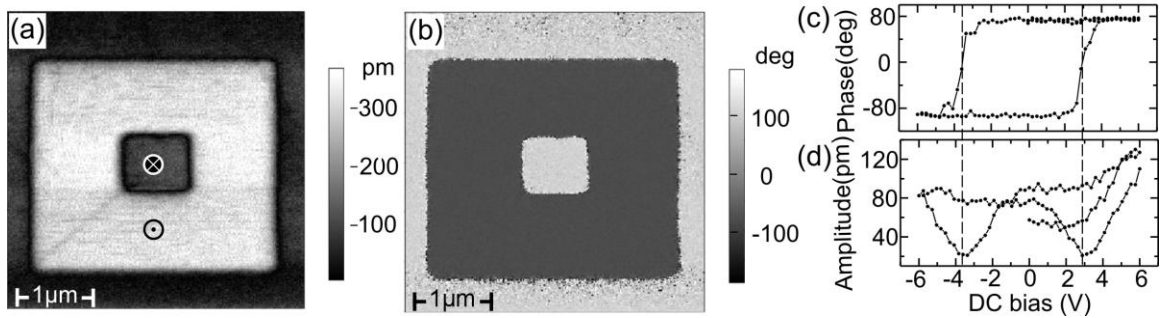


FIG. 3.5: Maps of the remanent piezo-response force microscopy amplitude signal (a) and phase signal (b) of a BaTiO₃(8u.c.)/Nb-SrTiO₃ film showing areas of opposite ferroelectric polarization, produced by scanning with the tip at ± 4 V DC bias voltage. Hysteresis loops of the PFM in-field phase (c) and amplitude (d) acquired from the same film.

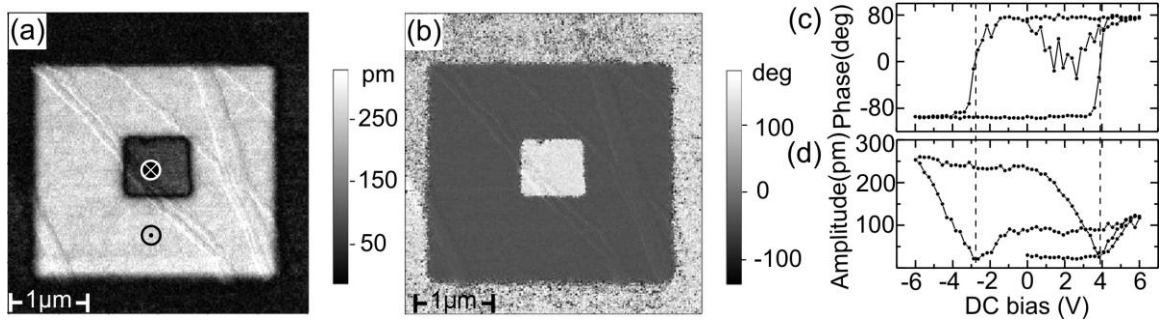


FIG. 3.6: Maps of the remanent piezo-response force microscopy amplitude signal (a) and phase signal (b) of a $\text{BaTiO}_3(13\text{u.c.})/\text{Nb-SrTiO}_3$ film showing areas of opposite ferroelectric polarization, produced by scanning with the tip at ± 4 V DC bias voltage. Hysteresis loops of the PFM in-field phase (c) and amplitude (d) acquired from the same film.

3.3.3 Electric polarization switching and detection with STM

The tip of the STM can be used as an electrode to switch and detect the polarization of barium titanate film. A possible application could be the study of electronic and magnetic properties of Fe impurities and clusters deposited on BaTiO_3 film upon the polarization re-orientation with the STM tip. With the aim to switch and detect of the polarization in BaTiO_3 film with an STM tip, the I-V characteristics have been recorded. The STM tip was brought in tunnel contact with the barium titanate film and the I-V curves were recorded by sweeping the bias voltage from -5V to +5V, and back to -5V. As previously described [section 2.2], the electrons could tunnel through both the vacuum gap and the BaTiO_3 film. Therefore, the tunneling current contains information about the potential profile of the BaTiO_3 film.

The measured I-V curves of a 13 u.c. BaTiO₃ film are shown in Fig. 3.7. The I-V curves exhibit non-linear behavior typical for a tunnel junction with an insulator, as outlined in figure 2.5. What is interesting here is that the width of the gap is dependent on the history of the measurement. The gap appears 3.5 volts wide when the I-V curve starts from positive voltage, compared to 1.5 volts when starting from negative bias voltage.

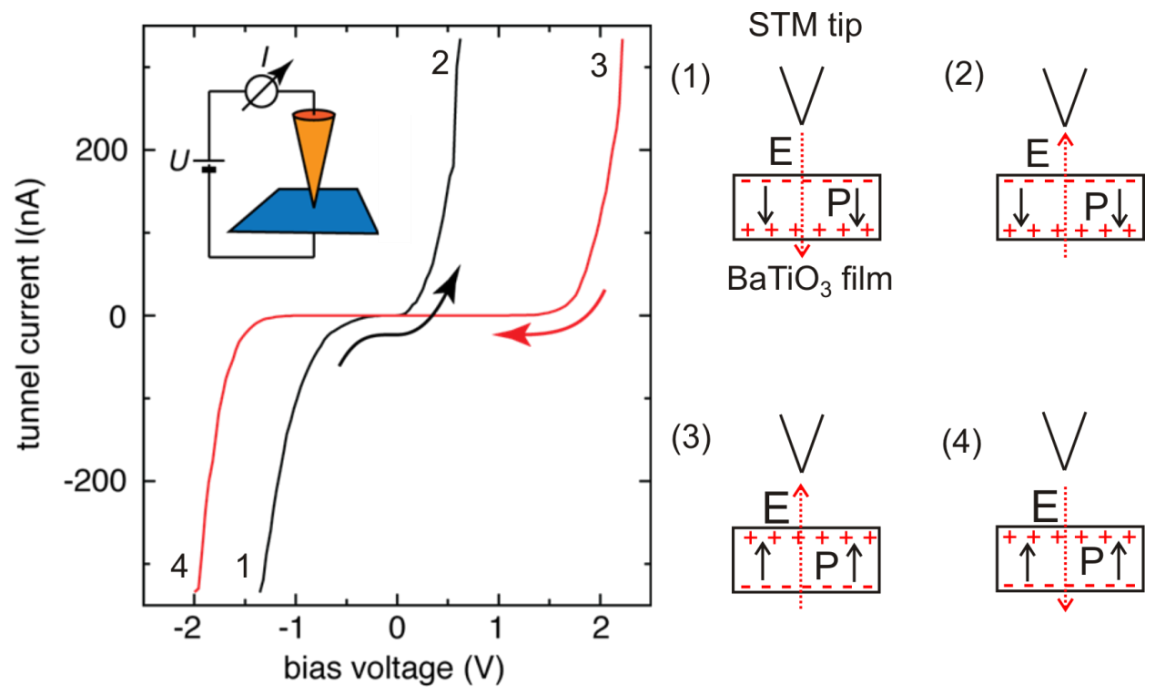


Fig. 3.7: I-V curves measured on BaTiO₃ film by STM exhibit the giant tunneling electro-resistance effect. The arrows represent the bias voltage sweeping direction. The figures (1), (2), (3) and (4) represent the electric field and polarization direction in BaTiO₃ film at position 1, 2, 3, and 4, respectively.

The physics of these I-V curves can be explained as follows, with reference to figure 3.7. At the beginning of the loop, a -5 V bias voltage is applied sample so that the large electric field is pointing into the plane of the BaTiO₃ film. It is large enough to

align the polarization of the BaTiO₃ film in the same direction. The electric field switches its direction, pointing out of plane direction for positive a bias voltage. However, as long as the electric field is lower than the coercive field of the BaTiO₃ film, the polarization in BaTiO₃ film does not change its direction. The respective I-V curve taken in region 1 → 2 shows a high conductance behavior, which reflects the high tunneling probability of electrons for the film polarization pointing into the plane. While the preamplifier is saturated at 333 nA signal (not shown), the loop is continued to +5 V. At a bias voltage of +5V (beyond position 3), the electric field is larger than the coercive field so that the polarization orientation of the BaTiO₃ film switches from into-the-plane direction to out-of-the-plane direction.

Next, the applied voltage is swept from +5V to -5V. The polarization in BaTiO₃ film is kept along out in the recorded bias region (from position 3 to position 4) because the electric field in between position 3 and position 4 is lower than the coercive field. As was shown in Fig. 2.8, the effective barrier height provided by the BaTiO₃ film depends on the direction of its polarization; hence the observed tunnel probability is dependent on the direction of the film polarization. In this experiment in Fig. 3.7, this is observable as a change in the apparent width of the band gap. Now, the effective barrier height is high. Therefore, the I-V curves show low tunneling probability behavior. When the bias voltage reaches -5 V (after position 4), the electric field is larger than the coercive field and it switches the polarization in BaTiO₃ film from out-of-plane direction to into-the-plane direction.

The I-V curves can be repeatedly performed with the same results. Two results are derived from the I-V curves: First, it is evident from the loops that the polarization of BaTiO₃ film can be reversibly switched by the electric field from the STM tip. The estimate switching voltage is 4.5 V and this voltage drop is for the vacuum gap and BaTiO₃ film combined. Since the resistance of the vacuum gap is on the order of giga-ohms and the resistance of BaTiO₃ film is about several kilo-ohms, the actual applied voltage on the BaTiO₃ is much smaller than 4.5 V. Second, the polarization direction can be detected from the tunneling resistance in the I-V curve measurement. The out-of-plane electric polarization in the BaTiO₃ film will result in high tunneling resistance and the in-plane electric polarization will lead to low tunneling resistance.

It is instructive to compare the results with similar AFM measurements published by Alexei Gruverman's group [64]. The typical I-V characteristics recorded on PFM-generated two antiparallel domains with contact-AFM are shown in Fig. 3.8. The I-V curves show a nonlinear behavior typical for conductance in tunnel junctions and a drastic change in resistance. The resistance with polarization pointing out-of-plane direction is about 2 orders of magnitude of that with polarization pointing into the plane. It shows a reversible giant tunneling electro-resistance effect due to the polarization switching in the BaTiO₃ film.

As described in chapter 2, section 2.2, the tunneling electroresistance ratio (TER) depends on the change of $\bar{\varphi}$ with polarization reversal [64]:

$$TER = \exp \left[\frac{\sqrt{2m}}{\hbar} \frac{\delta\phi}{\sqrt{\phi}} d \right], \quad (3.1)$$

where $\bar{\phi}$ is the average potential barrier height, d thickness of BaTiO₃ film, V applied voltage, and $\delta\phi$ the change of electrostatic potential upon the polarization reversal.

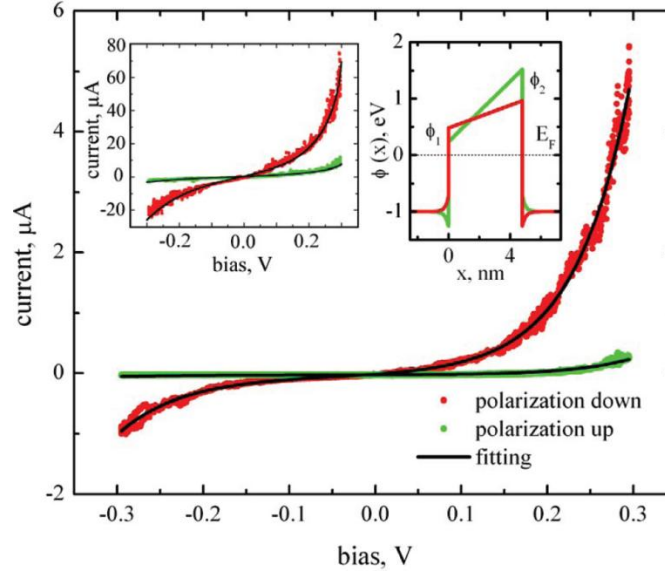


Fig. 3.8: I-V curves for two opposite polarization directions in the BaTiO₃ film measured by C-AFM. Solid lines, fitting of the experimental data by the WKB model by treating the BaTiO₃ film as a trapezoidal potential energy profile, which depends on the orientation of the polarization in BaTiO₃ film [64]. The figure is reprinted from [64].

In Figure 3.8, solid lines are the fitting of the experimental data by the WKB model (section 2.2), where the electrons are assumed to tunnel through a trapezoidal potential barrier [103] whose profile depends on the polarization orientation. According to the simulation, the reversal of the polarization changes the potential energy difference across the BaTiO₃ barrier from 1.28 to 0.48 eV and this change of 0.8 eV is due to the change in the electrostatic potential associated with ferroelectric polarization reversal and associated reorientation of the depolarizing field. Using the above WKB approximation,

the experimental I-V characteristics for the 4.8 nm thick BaTiO₃ films is well fitted [64]. The same physics can be applied with small modifications to explain the hysteresis loop taken with STM tip. The difference is that there exists a vacuum barrier in the STM junction, which takes away most of applied voltage from the STM tip since the tunneling resistance in vacuum gap is much larger than that in BaTiO₃ film.

3.3.4 Photoelectron Spectroscopy and Surface Termination

Photoelectron spectroscopy (PES) data have been collected on the 13 u.c. BaTiO₃ film, to determine the surface termination and to learn about the electronic structure of the films. Even though the growth of the films was stopped after deposition of the TiO₂ layer, the actual surface termination after transfer through air and annealing in oxygen needs verification. The Ba 4d and the Ti 2p spectra are summarized in Figure 3.9. The Ti 2p spectrum shows two characteristic peaks identified as the Ti 2p_{3/2} and Ti 2p_{1/2} peaks. In these spectra, no surface core level shift (SCLS) is observable. Such a shift is often observed at surfaces due to the reduced coordination of the atoms and the resulting change in charge state there. However, no SCLS has ever been reported for

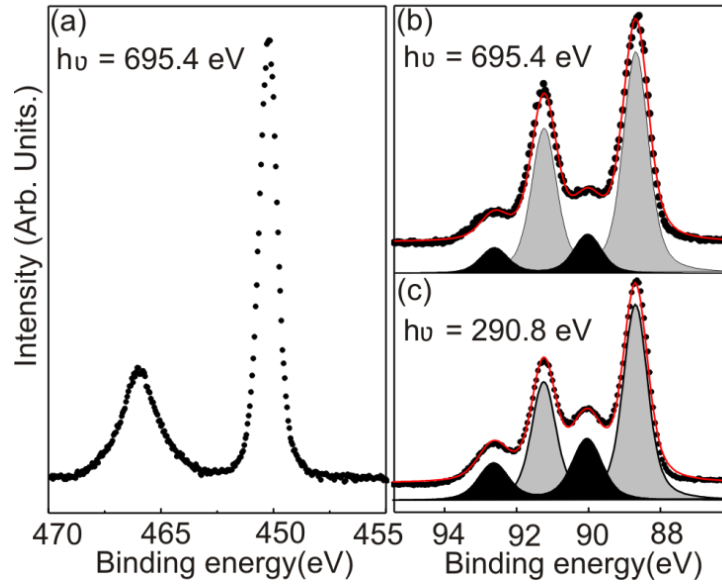


Fig. 3.9: Photoelectron spectra of BaTiO₃(001). Ti 2p spectrum (a), Ba 4d spectrum taken at 695.4 eV (b) and 290.8 eV (c), respectively. The binding energy is in reference to Fermi energy. Black- and gray-shaded areas in (b, c) represent fits to the bulk and surface peaks of Ba 4d_{5/2} and 4d_{3/2}, respectively.

TiO₂- terminated surfaces in the literature. The absence of SCLS for the Ti 2p peaks can even be expected since the effective charge of the Ti ions in the TiO₂-terminated BaTiO₃ surface is similar to that of Ti ions in the bulk BaTiO₃, as has been predicted in first principles calculations [90]. Thus, the absence of SCLS of Ti does not strictly exclude TiO₂ surface termination.

By contrast, the effective charge of Ba ions in a BaO-terminated surface is less than half of that of Ba ions in the bulk, thereby producing substantial SCLS, as has previously been reported for bulk BaTiO₃(001) [104]. For the present films, the 4d peaks of Ba split into the well-known 4d_{5/2} and 4d_{3/2} peaks and two additional peaks shifted by ~1.5 eV towards higher binding energies with respect to those 4d peaks (Fig. 3.9(b) and

(c)). Similarly shifted peaks have been reported for BaO surface layers and ascribed to SCLS [104]. Ba 4*d* spectra have further been taken with two different photon energies, 695.4 eV and 290.8 eV, shown in Figures 3.9(b) and (c). An increase of the ratio of surface- to bulk-peaks at lower photon energy is observed where the photoelectrons have smaller kinetic energy and are thus more surface-sensitive. Both observations, the SCLS and the energy dependence of the surface to bulk peak ratio of the Ba 4*d* states, suggest the existence of BaO in the surface of the films. However, a quantitative analysis of the fractions of BaO- and TiO₂-terminated surface areas requires a detailed analysis of the photoemission peak intensities.

The standard approach for the peak intensity analysis in photoelectron spectroscopy [105] has been adapted here for surfaces containing two atomic species. A detailed discussion of the spectral areas of the Ba 4*d* bulk and SCLS peak pairs is described below. The BaO and TiO₂ fractions of the surface termination have been obtained from the relative peak intensities of the bulk Ba 4*d* peak, I_B , and the surface Ba 4*d* peak, I_s , following a standard peak intensity ratio analysis found, for instance, in reference[105]. Considered here is a photon flux F incident on the sample surface. The intensity of the 4*d* peak in the photoelectron spectrum per BaO layer is proportional to the photon flux F , the areal density of Ba atoms in the layer N , and the photoelectron cross section for Ba 4*d* at the given photon energy. The surface monolayer of the BaTiO₃ film may consist of a fraction A of BaO and a fraction $(1 - A)$ of TiO₂. The intensity of the surface Ba 4*d* peak can be written as:

$$I_s = C \cdot F \cdot \sigma \cdot A, \quad (3.2)$$

where C is the total area illuminated by the incident photons. For the intensity of the bulk Ba $4d$ peak, I_B , two contributions are considered: one from the BaO-terminated fraction of the film, I_{B1} , and one from the TiO₂-terminated fraction of the film, I_{B2} . Both can be expressed in a form which, for I_{B1} , is

$$\begin{aligned} I_{B1} &= C \cdot A \cdot F \cdot \sigma \cdot \left(e^{-d/\lambda \cdot \cos \theta} + e^{-2d/\lambda \cdot \cos \theta} + \dots \right) \\ &= C \cdot A \cdot F \cdot \sigma \cdot e^{-d/\lambda \cdot \cos \theta} \cdot \frac{1}{1 - e^{-d/\lambda \cdot \cos \theta}} \end{aligned} \quad (3.3)$$

Here, θ is the angle between the surface normal of the sample and the spectrometer inlet. Assume constant values for the energy- and material-dependent electron escape depth or inelastic mean free path, λ , and the interlayer spacing of BaTiO₃, d . The summation is performed as if the film was of infinite thickness, since published values of the escape depth are 4 ~ 7 Å and 2 ~ 4 Å for spectra in Fig. 3.7(b) and (c), respectively [106]. They are thus much smaller than the film thickness of ~52 Å.

Likewise, I_{B2} is given by:

$$\begin{aligned} I_{B2} &= C \cdot (1 - A) \cdot F \cdot \sigma \cdot \left(e^{-h/\lambda \cdot \cos \theta} + e^{-(d+h)/\lambda \cdot \cos \theta} + \dots \right) \\ &= C \cdot (1 - A) \cdot F \cdot \sigma \cdot e^{-h/\lambda \cdot \cos \theta} \cdot \frac{1}{1 - e^{-d/\lambda \cdot \cos \theta}} \end{aligned} \quad (3.4)$$

It is taken into account here that the fraction of TiO₂-termination is (1-A) and h is the interlayer spacing between TiO₂ surface layer and the adjacent BaO layer. The fraction of BaO surface termination, A , can be determined from the intensity ratio I_B/I_S , which is also dependent on the escape depth and interlayer spacing of the BaTiO₃:

$$\begin{aligned} \frac{I_B}{I_S} &= \frac{C \cdot F \cdot \sigma \cdot \frac{1}{1 - e^{-d/\lambda \cdot \cos \theta}} \left[A \cdot e^{-d/\lambda \cdot \cos \theta} + (1 - A) e^{-h/\lambda \cdot \cos \theta} \right]}{C \cdot F \cdot \sigma \cdot A} \\ &= \frac{1}{1 - e^{-d/\lambda \cdot \cos \theta}} \left[e^{-d/\lambda \cdot \cos \theta} + \left(1 - \frac{1}{A} \right) \cdot e^{-h/\lambda \cdot \cos \theta} \right] \end{aligned} \quad (3.5)$$

It follows for A:

$$A = \left[\frac{I_B}{I_S} (1 - e^{-d/\lambda \cos \theta}) + (e^{-h/\lambda \cos \theta} - e^{-d/\lambda \cos \theta}) \right]^{-1} \quad (3.6)$$

Here, it is safe to assume $h = d/2$. The ratio I_B/I_S has been measured for 2 different photon energies, and the fitted peak values from the data in Figure 3.9 are summarized in Table 1. This results in 2 equations to solve for the unknown A, assuming for the escape depth $4 \sim 7 \text{ \AA}$ and $2 \sim 4 \text{ \AA}$, respectively in Fig. 3.9 (b) and (c). Therefore, the derived estimate for the fraction of BaO surface termination is $A = 17 - 32\%$. For the BaTiO₃ film, a mechanism for the inelastic scattering, the plasmon loss is missing and the escape depth should be larger than the corresponding one for the metal. Thus, the BaO surface fraction A is expected to be closer to $\sim 32\%$, which is obtained by inserting the upper limit of the aforementioned escape depths, or 7 \AA and 4 \AA , respectively in Fig. 3.9(b) and (c).

Table 3.1: Fitting parameters and best-fit results of the photoelectron spectra in Fig. 3.9(b, c). The parameters GW and LW are Gaussian and Lorentzian widths of the fitting function, respectively.

Photon energy	695.4 eV		290.8 eV	
	Gray	Black	Gray	Black
Peak position (eV)	88.7	90.0	88.7	90.0
Peak Area	94341.4	18935.5	63713.2	25482.0
GW	0.63	0.70	0.60	0.75
LW	0.35	0.40	0.35	0.45
Spin orbit splitting	2.55 eV	2.6 eV	2.55 eV	2.6 eV

The conclusion from this analysis is that the BaTiO_3 layer is dominantly TiO_2 -terminated, specifically that the fractions of the TiO_2 - and BaO -terminated surface areas are found to be $\sim 70\%$ and $\sim 30\%$, respectively. Uncertainties in our analysis result from estimates of the electron mean free path.

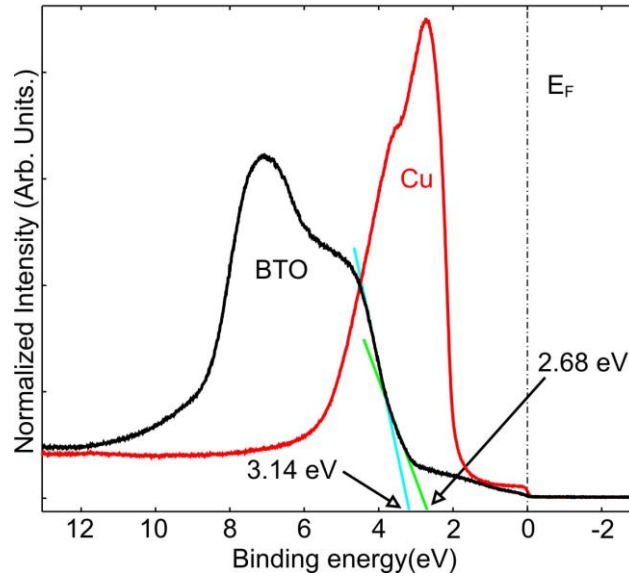


Fig. 3.10: Photoelectron spectra near Fermi edge of clean $\text{BaTiO}_3(001)$ and Cu. The photon energy was 111.04 eV. Extrapolations of the band edges give the band gap (blue, green lines). The non-zero signal in the band gap is due to the existence of mid-gap states (see text).

Further complementary experiments were performed on several BaTiO_3 thin films on SrTiO_3 and LaSrMO_3 substrates with angular-dependent photoemission spectroscopy, where the BaTiO_3 films were fabricated by different groups. Those samples have been prepared at varied annealing temperatures (473 K – 923 K) and oxygen partial pressures under UHV. All measurements consistently find surfaces dominantly terminated by TiO_2 .

It is concluded that the TiO_2 termination of $\text{BaTiO}_3(001)$ films is energetically favored and robust during in-situ sample preparation.

The valence band spectra of the BaTiO_3 samples are shown in Figure 3.10, together with the spectra of a Cu reference sample for comparison. Most prominently, the valence band, which is mostly of O $2p$ character, spans from ~ 3 eV to 10 eV binding energy. The width of the band gap is determined by extrapolating the band edge. This is shown in Figure 3.8 for two extreme choices of linear extrapolations, resulting in upper and lower limits for the band gap of 2.7 eV – 3.2 eV, respectively. In-gap states are observable between the valence band edge and the Fermi edge. Such states are most commonly found to originate from oxygen defects [104, 107, 108] and Ti^{3+} ions located in the vicinity of oxygen defects [108]. While first principles calculations predict that the valence band reaches the Fermi edge [107], we observe instead a band shift to higher binding energy. This shift is similar to the optical band gap of BaTiO_3 of 3.22 eV. It is reasonable to attribute this shift to the pinning of the Fermi level at the bottom of the conduction band to the effective n -type doping, which is a result of the reduction of the sample during the annealing. This indicates that the film has a band gap analog to bulk BaTiO_3 , with in-gap states due to local defects. The latter finding is not surprising for the 13 u.c. film given the observed transition to a 3D island structure.

3.4 Conclusions

The advantage of the nanometer thin films of BaTiO_3 studied here over bulk samples is the formation of large, atomically smooth surface terraces of unit cell height and the absence of surface reconstruction, while the films are still insulating and exhibit remanent electric polarization. Thus, ultrathin BaTiO_3 films are expected to become substrates for the fabrication of various model systems in the experimental studies of magneto-electric effects and also facilitate theoretical analysis. An important result of this work is the demonstration that high-quality surfaces of BaTiO_3 can be recovered after sample transfer through air. This simplifies the sample exchange in most lab settings where oxide growth, surface analytics, and device fabrication are performed in separate UHV systems. It is evident that BaO and TiO_2 surface terminations can coexist and are thus similar in energy, thereby providing experimental evidence towards a mostly theory-based discussion in the literature. Due to the prevalent TiO_2 termination of the surface, these films potentially enable the synthesis of high-quality Fe/BaTiO_3 interfaces that might exhibit the recently proposed magneto-electric effect due to Fe-Ti-bond modulation. The use of these thin BaTiO_3 films for the fabrication of ferromagnetic/ferroelectric interfaces is discussed in Chapter 4,

Chapter 4

Growth and characterization of ultrathin chromia films

4. 1 Introduction

Chromia (Cr_2O_3) is a magneto-electric anti-ferromagnet and it has attracted increasing interest in both experiments and theory. Cr_2O_3 has a corundum structure, consisting of a hexagonal close packed array of oxide anions with $2/3$ of the octahedral holes occupied by chromium. The side view of a unit cell of Cr_2O_3 structure is shown in Fig. 4.1(a). The distance between two equivalent surface terminations along c axis is

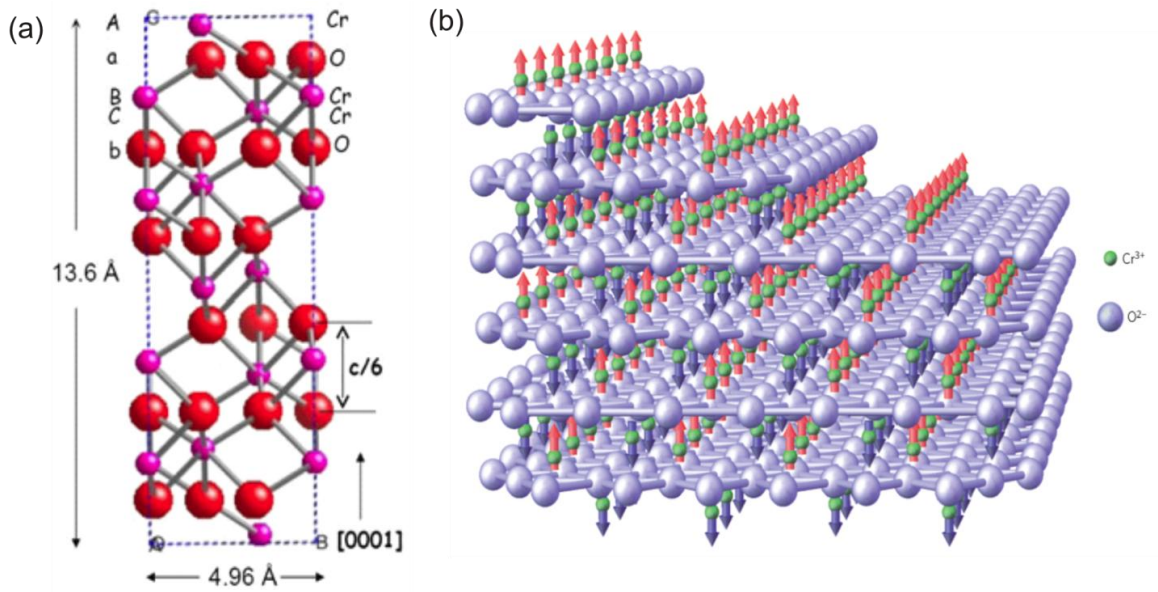


Fig. 4.1: (a) The side view of a unit cell of Cr_2O_3 structure. The distance between two equivalent charge type surfaces along c axis is about 2.27 Å. (b) The spin structure of a Cr_2O_3 single crystal with a stepped (0001) surface. Up (red) and down (dark blue) spins of the Cr^{3+} ions (green spheres) point along the c axis [15]. This figure is reprinted from [15]

about 2.27 Å. Fig. 4.1(b) [15] reveals that each terrace has uncompensated surface magnetization arising from surface Cr^{3+} ions. A single-domain antiferromagnetic state is formed with all surface Cr spins pointing in the same direction. What is special here is that the surface magnetization can be flipped by an external electric field. This property is useful for the electric field control of the exchange bias of ferromagnetic ad-layers. For example, the electric control of exchange bias at room temperature has been achieved on the system of a ferromagnetic Pd/Co multilayer deposition on Cr_2O_3 single crystal [15].

Extensive studies on the structure and chemical reactivity of Cr_2O_3 surfaces have been performed on ordered films grown on single crystals surfaces, including Cr(110) [109, 110, 111], Pt(111) [112, 113], Cu(110) [114], Cu(100) [115], Cu(111) [24], and Ag(111)[116]. Most experiments utilized integral tools, such as LEED, XPS, XRD, and AES. There are few local measurements with STM focusing on morphology [111], where stripes with limited width are observed after exposing to oxygen at 625 K and subsequent annealing at 925 K. However, more studies are needed to characterize the structure and electronic properties of thin chromia films. In order to understand the surface structure of $\alpha\text{-Cr}_2\text{O}_3$, theoretical calculations based on *ab initio* density functional theory [117] have been performed. Wang and Smith [117] predicted that surface terminations of $\alpha\text{-Cr}_2\text{O}_3$ critically depended on the oxygen partial pressure and annealing temperature. At an oxygen partial pressure of 10^{-6} mbar, the possible surface structures include oxygen-terminated surface, 1/3 ML chromyl ($\text{O}=\text{Cr}$)-terminated surface, 2/9 ML chromyl-terminated surface, 1/9 ML chromyl-terminated surface, and 1/3 ML Cr-terminated surface in the order of increasing temperature, where 1 ML is defined as the number of

oxygen atoms in a bulk Cr_2O_3 (0001) oxygen plane. Rohrbach et al. [118] show that all oxygen-terminated surfaces are strongly disfavored in GGA+U and the Cr-O₃-Cr-termination is thermodynamically favorable at room temperature and above. However, this is in contrast to the complex surface structured determined by SXRD on $\alpha\text{-Cr}_2\text{O}_3$ in UHV and oxygen partial pressure [119], where a surface termination with a partially occupied double layer of chromium is found in UHV and a chromyl-topped structure is found at an oxygen partial pressure of 1×10^{-2} mbar. In the following, low temperature STM/STS is used to demonstrate that different surface terminations may coexist within the surface of an ultrathin chromium oxide film grown on Cu(111) substrate. These studies presented in this section contribute to the standing discussion of the surface terminations of chromia and can potentially aid in the development of *ab-initio* models.

4.2 Experimental aspects specific to these studies

The Cu(111) substrate preparation has been described in chapter 2. Chromium pieces were purchased from Alfa Aesar with a purity of >99.995%. Two monolayer (ML) of metal chromium were deposited on clean Cu(111) surface from an e-beam heated crucible. The as-grown Cr film was studied with STM. Afterwards, the as-grown Cr/Cu(111) sample, it was annealed in oxygen at partial oxygen pressure of 5×10^{-7} mbar at 923 K for 1 minute. The sample is transferred through the air after preparation. After the sample is annealed in UHV at 593 K for about 20 minutes to remove possible contaminants from air exposure, mainly water molecules, the XPS and LEED investigations are carried out in a separate UHV system. The XPS studies are performed

with a hemispherical electron energy analyzer spectrometer, using a Mg K α X-ray source at 1253.6 eV. The Cr $2p_{3/2}$ and O $1s$ core level XPS spectra were obtained for different emission angles.

4.3 Results and discussion

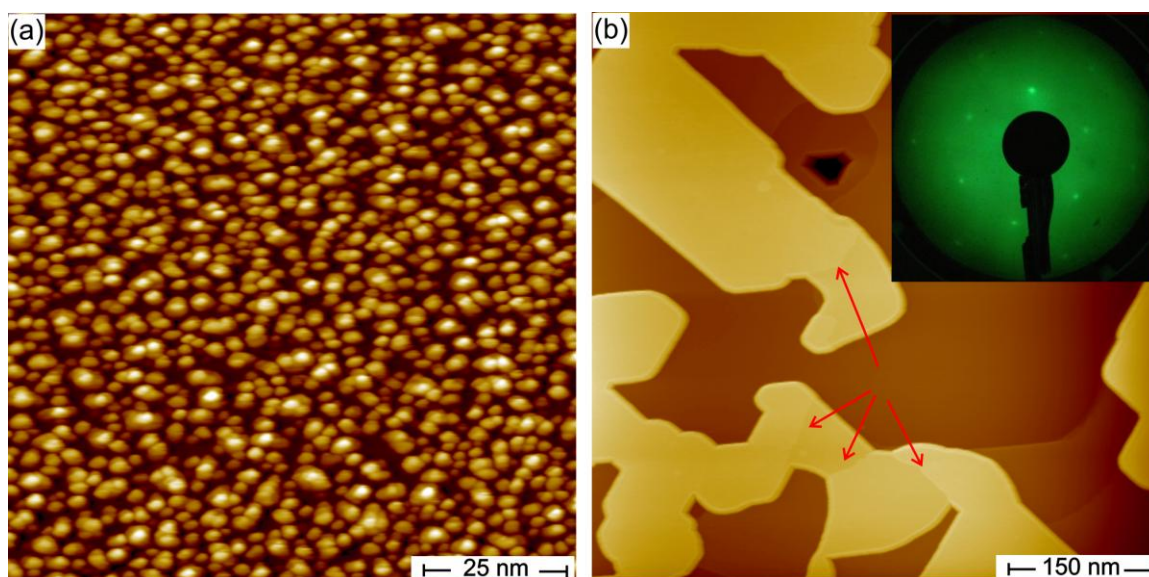


Fig. 4.2: STM topographic image of 2ML Cr deposited on Cu(111) before and after annealing in oxygen. Cr clusters are deposited on Cu(111) at room temperature. (a) STM image of the as-grown sample. (b) STM image of chromium oxide film after annealing the as-grown sample in oxygen atmosphere at 923 K for 1 minute. Inset: LEED pattern measured on the annealed sample at 260 eV. Arrows indicate the small steps on the films.

A Cr film of 2 ML nominal coverage is studied with STM first. A typical STM image is shown in Fig. 4.2 (a). It is observed that chromium grows in the Volmer-Weber mode, which is a 3D growth mode. In Fig. 4.2 (a), small separated Cr islands of 2--5 nm in diameter and 2--5 Å in height are observable. This sample was then annealed in oxygen partial pressure at 923 K for 1 minute. The STM image of the oxidized film reveals large, flat, highly ordered films, spanning across several Cu(111) terraces over

several hundreds of nanometers (Fig. 3.16(b)) . The oxide film has an apparent height of about 2 nm and the distinctive steps are visible on the islands with apparent heights of 1 or 2 Å, as indicated by the arrows. The comparison of both images clearly shows that the small Cr islands coalesce to form wide islands that are oxidized thoroughly during annealing in oxygen.

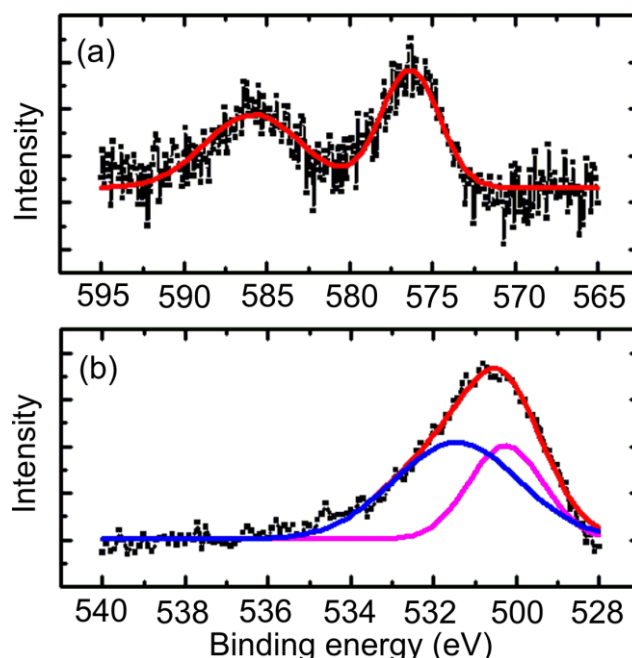


Fig. 4.3: XPS spectra (a) Cr 2p and (b) O 1s taken at 20 degree emission angle. The intensity is in the arbitrary unit. Black dotted lines are experimental data and other color lines are peak fitting results. The red line is the fitting XPS spectrum. The blue line represents the fitted spectrum with a peak at 531.5 eV for chromia and the pink line shows the fitting spectrum with a peak at 530.2 eV for copper oxide.

In addition to STM, also XPS and LEED measurement are performed on the sample. The sharp hexagonal LEED pattern (Fig. 4.2(b) inset) taken at 260 eV is consistent with hexagonal surface structure of Cr_2O_3 [24]. The strong diffuse background of the LEED image may be due to the insulating nature of the chromium oxide film. The Cu(111) surface is also oxidized during annealing in oxygen partial pressure which is

confirmed by a clear chemical peak shift from the metallic peak in Cu 2*p* XPS spectra [Data is not shown here]. Fig. 4.3 shows XPS spectra of both the Cr 2*p* and O 1*s* core levels taken at the room temperature along 20 degree emission angle. The small signal-to-noise ratio for Cr 2*p* spectra is expected from the low coverage of chromium oxide film. The binding energy of Cr 2*p*_{3/2} core level is about 576.2 eV, a clear shift from chromium peak for bulk metal at 574.4 eV, and this chemical shift is in reasonable agreement with literature values for Cr₂O₃ (576.6 eV±0.3 eV). The Cr 2*p*_{3/2}–Cr 2*p*_{1/2} binding energy separation is 9.5 eV, which is also very close to the binding energy (BE) separation for Cr₂O₃ (9.8eV). The binding energy of O 1*s* core level for annealed sample is 530.7eV±0.1eV. The observed peak of O 1*s* at 530.7 eV is located between the peak of chromia at 531.5 eV and the peak of copper oxides at 530.2 eV. In addition, the peaks of all other chromium oxides, such as CrO₂ and CrO₃, are located around 530 eV. Hence, the peak position of oxygen is interpreted as the superposition of chromia spectra and copper oxide spectra. A multiple peak fit of the XPS spectra with peaks fixed at position O 1*s* from chromium oxide and copper oxide shows that the experimentally observed peak can be reproduced by assuming Cr₂O₃ islands, separated by an oxidized Cu substrate. From this fit and the LEED result, it is concluded that the films are of composition Cr₂O₃.

In Fig. 4.4, an STM image shows that a chromium oxide island can cross over several Cu(111) substrate terraces. The apparent height of the islands is approximate 1nm. The apparent height of the right side of terrace is 1.03nm, while it increases to 1.29 nm relative to the substrate on the left. This thickness is slightly smaller than a unit cell

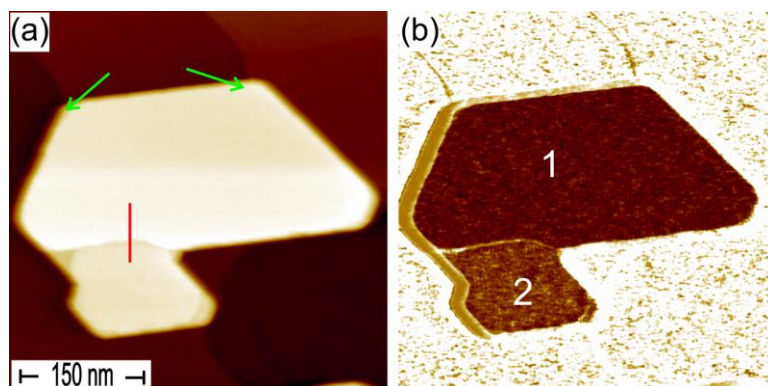


Fig. 4.4: (a) Topography image of ultrathin chromium oxide film on Cu(111), (b) Simultaneously recorded dI/dV map, revealing different conductivities of terraces #1 and #2. The green arrows indicate the substrate step edges and region #1 and region #2 is separated by a small step, as indicated by a red line. The image is taken by -5.5 V bias voltage and 0.2 nA current.

height of a Cr_2O_3 film (1.36 nm). The interpretation of height measurements of oxide films with STM has to be undertaken with care. On metal surfaces in constant current mode of the STM, the tip's z-position traces out the surface morphology. For oxides in the tunnel regime, instead, the feedback loop forces the tip closer to the surface of an island, due to the reduced conductivity there, in order to restore the constant tunneling current. The images in Fig. 4.4 have been measured at a voltage of 5 Volts, above the band gap. As outlined in chapter 2.2, the electron tunnel into the conduction band of the film, so that height measurements reveal approximately the true height. In other words, the conductivity of oxide film is less than that of substrate and the tip-sample distance is reduced in order to maintain the same tunneling current above the insulating islands. Hence, a smaller apparent height is expected for chromium oxide. Even though the island extends across 2 substrate step edges (as highlighted by green arrows), there are no corresponding kinks on the surface of the chromium oxide island at each step edge. The

apparent height for the observed small step on the island is 1 Å, which is indicated by the red solid line in the Fig. 4.4 (a). This step height is much smaller than from the distance between two equivalent (0001) surface terminations of α -Cr₂O₃, which is about 2.27 Å.

It is tentatively concluded that the observed steps do not correspond to the height of a unit cell but rather to fraction of a unit cell. This implies that neighboring terraces are of different terminations, such as Cr-terminated and chromyl-terminated surfaces. Another possible explanation is that two regions have different surface polarization. As discussed in Section 3.3.3, the surface polarization can be changed by appropriate bias voltages, which may result in considerable change in the tunneling resistance. The two possible explanations cannot be distinguished with the current data. Here, a tentative explanation is given based on the different surface terminations. The dI/dV map recorded on the same chromium oxide island is shown in Fig. 4.4(b), where the brightness is a measurement of the local conductivity. It can be seen that the region #1 and region #2, which are separated by a step with 1 Å height, have uniform conductivity within each terrace. However, the dI/dV signal in the region #2 is much higher than that in the region #1. The contrast in dI/dV map reveals that two regions have different DOS, which may be due to different surface terminations. Another argument for this phenomenon is that the conductivity of the oxide film is correlated with its thickness, since terrace #1 is about 1 Å thicker than terrace #2. However, later in this section, results will be presented that contradict such a conclusion.

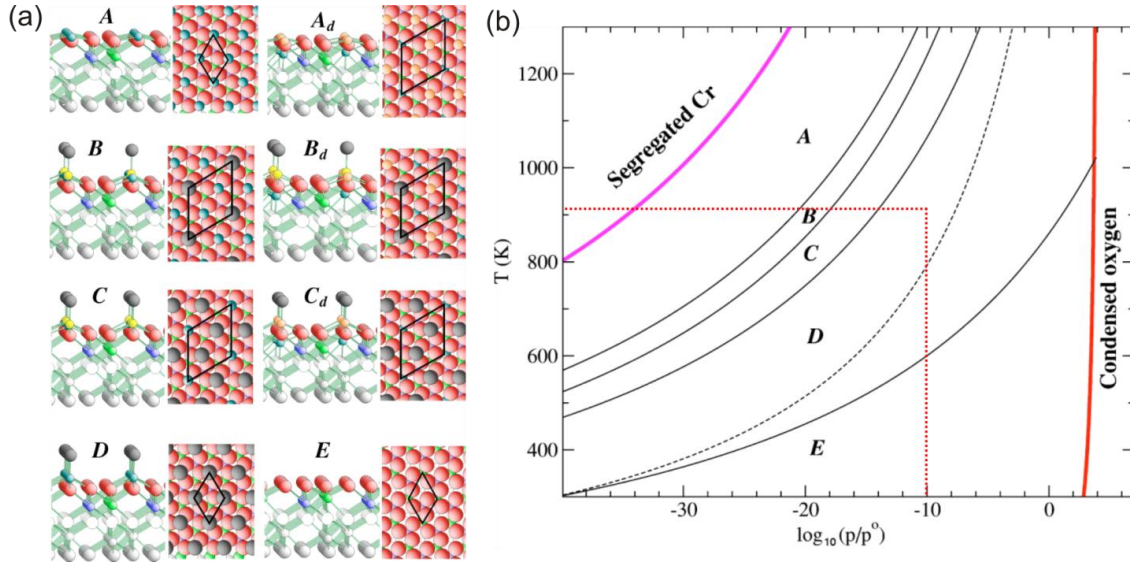


Fig. 4.5: Principal surface structure configurations (a) and the corresponding surface phase diagram for the Cr₂O₃(0001) (b) [117]. This figure is adapted from [117].

Surface terminations of Cr₂O₃ have been studied in theory by Wang [117]. These results aid in discussing the contrast in the dI/dV map. Possible surface terminations of Cr₂O₃ film have been calculated and it is predicted that principal Cr₂O₃(0001) surface structure configurations include Cr-terminated, O-terminated, and chromyl (Cr=O) terminated configurations. In Fig. 4.5(a), the large balls represent O atoms, the small balls Cr atoms, and the shade color of the balls indicate that they are at different layers. A_d , B_d and C_d indicate the nearly degenerate (surface energies within 2 meV/Å²) states of A, B, and C, respectively. The surface unit cells are plotted in the figure. As shown in Fig. 4.5 (b), the surface phases critically depending on the annealing temperature and the oxygen partial pressure. Considering the experimental parameters in this study, as indicated by the red dashed lines in the Fig. 4.5 (b), the surface termination to be expected, based on this theory, is D (1×1) 1/3 ML (O=Cr). A specific feature of the experiments here is that

the experimental conditions are not well defined at the end of the annealing of the film in oxygen, but it cannot be excluded that the decreasing temperature and oxygen pressure alter the surface of film.

Further studies of morphology and electronic DOS have been performed on other chromia islands, such as the one in Fig. 4.6. This island exhibits multiple intrinsic steps at the surface. The film is also about 1 nm in thickness. The apparent heights of all steps are labeled individually, as shown in the morphology image in Fig. 4.6 (a). There are two distinct step heights---1 and 2 Å. The comparison between morphology and dI/dV map reveals that the contrast in the dI/dV map does not depend on the film thickness. For example, several terraces of different height show the same brightness in the dI/dV map. However, the contrast seems to be strongly correlated with the value of step heights between two adjacent terraces. Terraces of the same contrast are always separated by a 2 Å step, while terraces of different contrast are always separated by a 1 Å step. These values are close to the distance between two equivalent (0001) surface terminations of α -Cr₂O₃ (2.27 Å) and the one between adjacent Cr- and O-layers (1.15 Å), as illustrated in Fig. 4.1(a). The strong correlation between the step height and contrast in dI/dV map indicates that the chromium oxide island may have indeed at least two surface terminations. In addition to the contrast between different terraces separated by apparent step edges, there is also contrast inside one terrace where no step edge is detectable in topography image, as indicated by a red rectangle in the dI/dV map. The darkest region in the dI/dV map indicates that this region has the lowest DOS. It is therefore concluded that three different surface terminations co-exist in this sample. This result is consistent with

the theoretical prediction of surface phase diagram for Cr_2O_3 film under current experimental parameters [117], but it could also be noted that they contradict other theories from Belashchenko [120]. Hence, this research is potentially helpful to contribute to a standing discussion about termination of Cr_2O_3 surfaces.

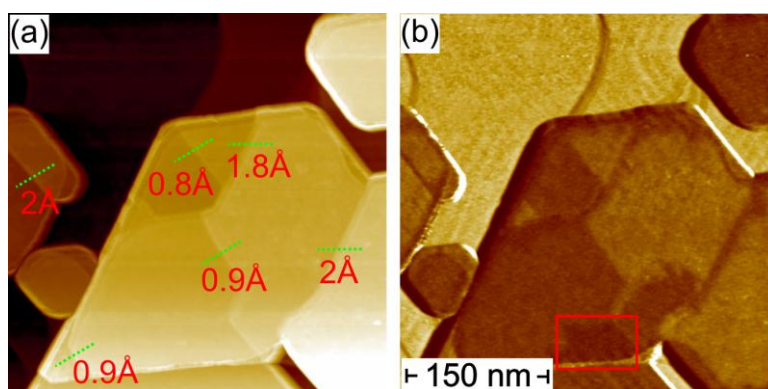


Fig. 4.6: Surface structure and electronic properties of a chromium oxide island with multiple steps: (a) morphology image; (b) simultaneously recorded dI/dV map. There exists strong correlation between small step height and the contrast in dI/dV map. The bias voltage is -5.5V and tunneling current is 0.2 nA .

4.4 Conclusion

In summary, ultrathin chromium oxide film has been grown on a $\text{Cu}(111)$ substrate and the surface structure was characterized by STM and LEED. The STM image for the as-grown sample reveals that the chromium follows the 3D-island growth mode (Volmer-Weber) and the cluster diameter varies from 2 nm to 5 nm . The STM images of the annealed sample show that the small chromium islands coalesce to form flat and ordered film with more than 200 nm in width, spanning several $\text{Cu}(111)$ substrate terraces. The combination of XPS spectra at $\text{O } 1s$ and sharp LEED pattern indicates that

the chromium oxide film is Cr_2O_3 . The strong correlation between step heights and the contrast in the conductance map is explained as the result of different surface terminations in the ultrathin chromia films.

Chapter 5

Magnetism of Fe nanostructures on ultrathin BaTiO₃ films

5.1 Introduction

Previous work in Chapter 3 has shown that barium titanate films with a few unit cells in thickness are atomically smooth, crystalline, dominantly TiO₂ terminated, and ferroelectric. As a next step towards multiferroic heterostructures, the magnetism of Fe nanostructures deposited on BaTiO₃ films, as well as the Fe oxidation is studied here. Very few studies have been reported on the interface oxidization of submonolayer Fe deposited on ultrathin BaTiO₃ film. When Fe is deposited on BaTiO₃/La_{2/3}Sr_{1/3}MnO₃ bi-layers, which were grown on NdGaO₃(001) substrates, an additional FeO monolayer between BaTiO₃ and Fe is assumed for an accurate description of the interface structure [121]. It means that Fe films are partially oxidized as FeO. The atomic structure of the interface for ultrathin BaTiO₃ film grown on Fe(001) has been investigated by surface x-ray diffraction. It was found that a defined TiO₂-Fe interface was formed [122]. In other studies, the system of ultrathin BaTiO₃/Fe bi-layers grown on MgO(001) and SrTiO₃(001) substrates was investigated. The absence of any magnetically dead layer was assumed to be proof of a sharp Fe/BaTiO₃ interface structure at the atomic scale[120]. For both studies, the Fe films were several to tens of nanometer thick. Hence, the methods applied may lack the sensitivity to address the magnetism and chemical structure

at the interface. To overcome this problem, this study focuses on Fe impurities and clusters to determine the magnetism and oxidation at the interface.

Fe adsorbates at oxide surfaces have a natural tendency to react with surface oxygen, to form various forms of iron oxide. Fe overlayer oxidation has, for instance, been found at the interface of Fe/NiO where Fe is grown at room temperature. The amount of Fe oxidation increases during post-annealing above the NiO Neel temperature [123]. A paramagnetic FeO formation at the interface during the growth process is used to explain the reduced magnetic moment of Fe films on NiO(001) crystals [124, 125]. Another example of interface oxidation are Fe/CoO bi-layers on Ag(001) [126]. The oxidation of the interfaces is determined to 0.3 ML from the observed decrease in the magnetic moment. It is a challenge for experimentalists to develop growth strategies that suppress interface oxidation.

In this study, methods of Fe growth on BaTiO₃ are comparatively studied. Three different growth methods have been analyzed, which are (i) MBE growth with the substrate held at room temperature, (ii) MBE growth with the substrate held at 10 K, and (iii) growth of Fe via buffer-layer assisted growth. A study of the magnetism of Fe impurities and clusters is presented. Not entirely unexpected, it will be demonstrated that Fe oxidation is suppressed by MBE growth at low temperature and buffer-layer assisted growth, in comparison to room-temperature grown Fe. The Fe clusters show sizable magnetic moments in both growth methods (ii) and (iii). The oxidation level is

estimated from XAS lineshapes and XPS spectra. The ultimate goal is to identify the best way forward to suppress interface oxidation completely.

5.2 Experimental aspects specific to these studies

The preparation of BaTiO₃ film has already been described Chapter 3. The STM measurements are performed in constant current topography mode at 77K, with a typical tunneling setting of 2.7 V bias and 1 nA tunneling current.

(i) MBE growth at room temperature

The MBE growth of Fe on BaTiO₃ films at room temperature was carried out in a UHV chamber with a base pressure of 2×10^{-9} Torr. The Fe oxidation was studied by the angle angle-resolved X-ray photoelectron spectroscopy (AR-XPS). The XPS analyses were performed, *in-situ*, with a hemispherical electron energy analyzer spectrometer, using the Al K α X-ray source at 1486.6eV. The Fe L-edge XPS spectra were obtained at different emission angles by rotating the sample plate. This procedure was repeated for various Fe coverage.

(ii) MBE growth at 10 K

The MBE growth of Fe on BaTiO₃ films at 10 K was performed in a separate UHV system at beam line ID-08 at the European synchrotron radiation Facility (ESRF) in Grenoble, France. The end-station of the beamline consists of two chambers with a base pressure of 2×10^{-10} Torr. The preparation chamber is equipped with LEED optics and an STM, and the analysis chamber has an e-beam evaporator for Fe deposition and the low temperature superconducting magnet. All experiments, including sample cleaning, Fe

deposition and XMCD measurement, were performed *in-situ*. Fe deposition was done inside the XMCD chamber, so that magnetic measurements could directly be performed on the as-grown film at 10 K, without sample transfer. Fe impurities were deposited at the growth speed of 0.002ML/min with the substrate at 10 K. The Fe thickness was determined from ratio of peak intensity at L3 edge to the pre-edge intensity. The XAS spectra were obtained on the total electron yield mode by monitoring the sample drain current. The maximum magnetic field available is 5.5 Tesla.

(iii) Buffer-layer assisted growth at about 100 K

Fe clusters were deposited on BaTiO₃ films by the buffer-layer assisted growth [127,128]. The buffer-layer assisted growth (BLAG), as shown in Fig. 5.1, includes three separate preparation steps: (i) adsorption of Xenon on BaTiO₃ at substrate temperatures of $T < 50$ K, (ii) MBE deposition of Fe on the xenon buffer layer at this temperature. Fe cluster form directly on the Xe layer due to dewetting effects. (iii) Thermal desorption of the Xenon layer by rising the temperature to $T > 120$ K, to bring the clusters in contact with the BaTiO₃. During the Xenon desorption, the Fe clusters coalesce and thus grow in size. The final cluster size can be controlled by the Xe thickness and Fe coverage [129]. Higher Fe coverage results in larger Fe cluster size. Also, thicker Xe layer will give more time for Fe clusters to coalesce during desorption of Xe process, hence increasing the cluster size as well. This study compares two samples: (1) 2 ML Fe/ 500 L Xe/ BaTiO₃ film and 4 ML Fe /500 L Xe/ BaTiO₃.

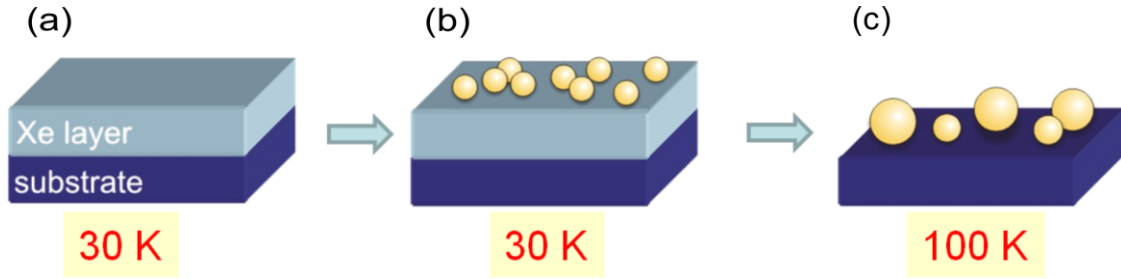


Fig. 5.1: Buffer-layer assisted growth process for Fe on BaTiO₃ film. (a) Adsorption of Xenon buffer layer on the pre-cooled substrate; (b) MBE deposition of Fe on Xenon buffer layer; (c) Soft landing of Fe clusters on BaTiO₃ film through thermal desorption of Xenon layer. [127, 128]

The main advantage of the buffer-layer assisted growth is that adatoms diffuse on the buffer layer to form 3D clusters and the 3D clusters are then brought into contact with the substrate. It is expected that this will reduce the Fe's chemical reactivity and reduce the amount of Fe oxidation considerably. The magnetic characterization of Fe clusters is done by XMCD measurement at the Pohang light source. The XAS spectra are also obtained on the total electron yield mode. Here, an electromagnet with its maximum field (H_m) ~ 0.5 T is utilized for XMCD measurement.

5.3 Results and discussions

First, studies at room temperature grown Fe are presented. The XPS spectra of the as-grown Fe films are recorded at different emission angles as a function of the Fe coverage. The XPS spectra of the L_{2,3} edge of Fe at 0° emission angle (a) and 40° emission angle (b) are shown in Fig. 5.2. The Fe L₃ peak is located around 710 eV for all Fe coverage, a chemical shift away from metallic Fe peak at 708 eV. By fitting each spectrum with peaks the peak positions of Fe and various Fe oxides, similar to the

procedure shown in chapter 4, it is determined that most Fe impurities are oxidized. This finding of high oxidization level of Fe at the Fe/BaTiO₃ interface at room temperature is consistent with earlier reports in reference [130].

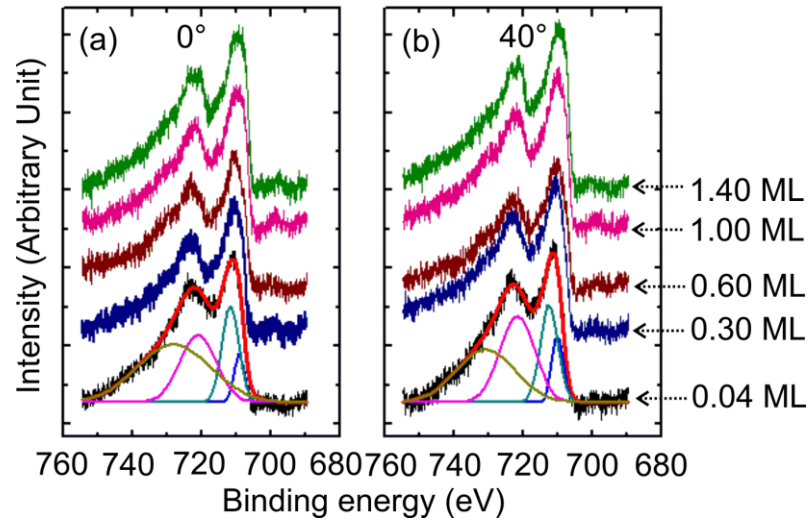


Fig. 5.2: XPS spectra of Fe deposited on BaTiO₃ film at room temperature via MBE growth at 0° emission angle (a) and 40° emission angle (b). The solid lines are the curve fittings corresponding to Fe and Fe oxide peaks at 0.04ML Fe coverage.

Next, Fe deposited by MBE at $T = 10$ K is discussed. The magnetic properties are measured by XMCD. Spectra have been recorded on the as-grown Fe clusters as a function of the film thickness. Fig. 5.3 shows the normalized (by the incident light intensity) XAS and XMCD spectra of various sub-ML Fe coverage, which are grown on 13 u.c. BaTiO₃ film with MBE growth at 10K. The XAS spectra are measured around the Fe L-edge under maximum magnetic field of $5 \pm T$ at both positive and negative helicities. The XMCD spectra are derived by taking the difference of XAS spectra of opposite magnetic polarization.

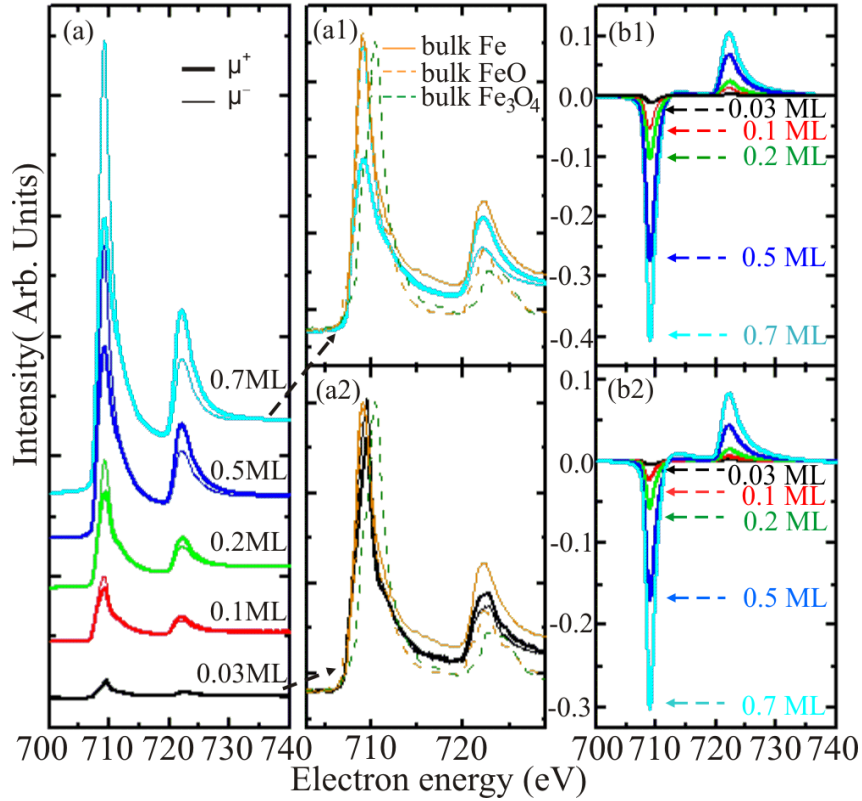


Fig. 5.3: XAS and XMCD spectra of Fe films at L-edge with different Fe coverage. (a) Polar XAS of Fe film near L-edge; (a1) and (a2) are comparisons polar XAS spectra of 0.7 ML and 0.03 ML Fe films to those of bulk Fe, FeO, and Fe₃O₄. (b1) and (b2) are in-plane and polar XMCD, respectively.

Fig.5.3 (a) shows XAS spectra of the Fe impurities with the maximum available magnetic field of ~ 5 T applied along two opposite directions along the surface normal. Each XAS spectrum displays the well-known L_3 and L_2 adsorption edge, which correspond to optical transition from the $2p_{3/2}$ to $3d$ and from $2p_{1/2}$ to $3d$. The XAS signal increases as the Fe coverage increases. The spectra are compared to published spectra of bulk Fe, FeO, and Fe₃O₄ from references [131,132], as shown in Fig. 5.3(a1) and (a2). Fe₂O₃ shows distinct additional peak at pre-absorption edge which is not observed in the XAS spectra in Fig. 5.3(a). Thus, formation of Fe₂O₃ is excluded. However, the L_3 and L_2 lineshapes of 0.03ML film deviates from those of bulk Fe in Fig. 5.3(a2). The peak

position of L_3 edge is shifted to higher energy by ~ 0.4 eV compared to bulk Fe and it is lower energy by ~ 1 eV compared to bulk Fe_3O_4 . Several models can be used to explain this effect. First, the Fe film at 0.03 ML coverage is composed of a mixture of Fe and Fe oxides, such as Fe_3O_4 . Another possible reason is a size effect. The Fe is presented as low-coordinated impurities as well as high co-ordinated Fe in impurity form, instead of bulk. The impurity form may have different band structure compared to the bulk, leading to different XAS lineshape. For the 0.7 ML Fe film, the spectral shape is almost identical to that of bulk Fe.

Fig. 5.3 (b1) and (b2) show the XMCD spectra at the Fe L_2 and L_3 edges for the in-plane and polar geometries, respectively. For all of the Fe coverage, well-defined XMCD spectra are observed, which provide proof that the Fe films have a magnetic moment, even at the lowest coverage studied, 0.03 ML. In order to obtain the mean magnetic moment per Fe atom, the sum rules are applied on the XAS and XMCD spectra in Fig. 5.3(b1) and (b2). The detailed analysis procedure has been described in section 2.4. Here, the number of electrons in the Fe $3d$ orbital is taken to be 6.61 as the bulk value. Since $\langle T_z \rangle / \langle S_z \rangle$ is only $\sim 0.38\%$ for Fe according to first principles calculations, it is neglected in the analysis [133]. The results of the sum rule analysis are summarized in Fig. 5.5.

Fig. 5.4 shows hysteresis curves of (a) 0.03 ML, (b) 0.2 ML and (c) 0.5 ML Fe impurities grown on $\text{BaTiO}_3(001)$ with MBE growth at 10 K. The hysteresis loops are taken by setting the photon energy to the L_3 -edge energy and recording the peak intensity

as a function of the applied magnetic field. All hysteresis curves exhibit a nearly saturated S-shape, typical for superparamagnetism of the Fe coverage. Accordingly, fits based on a Langevin function well reproduce the experimental hysteresis curves. From the curve fitting, the saturation magnetic moment μ_{sat} per Fe atom is determined and summarized in Fig. 5.5. For all of the films, the higher magnetization achieved in an applied field along the film plane compared to in-plane loops suggests that the easy magnetization axis is in-plane.

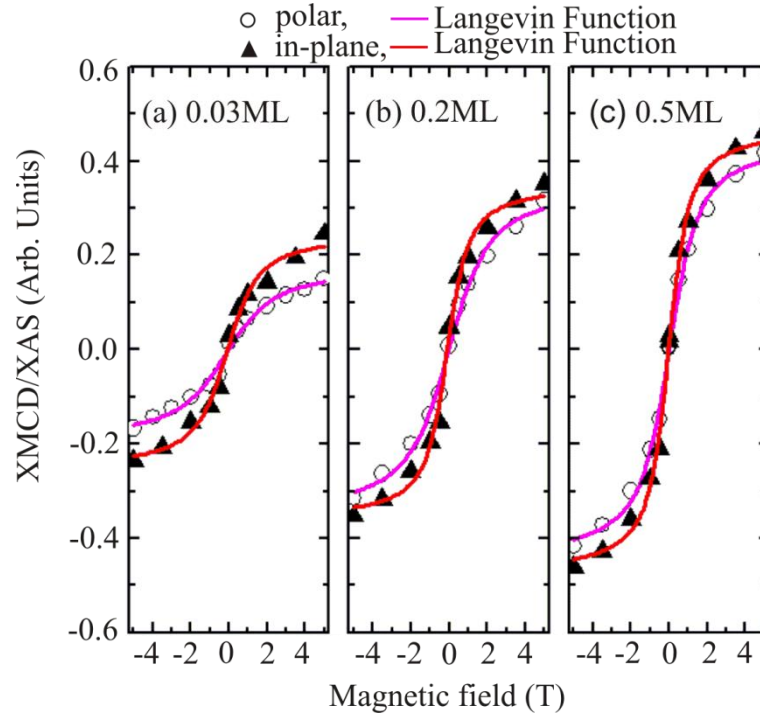


Fig. 5.4: Hysteresis curves of (a) 0.03 ML, (b) 0.2 ML and (c) 0.5 ML Fe grown on BaTiO₃ film. The red (in-plane) and pink (polar) lines are fitting results by Langevin function to estimate the saturation magnetic moments.

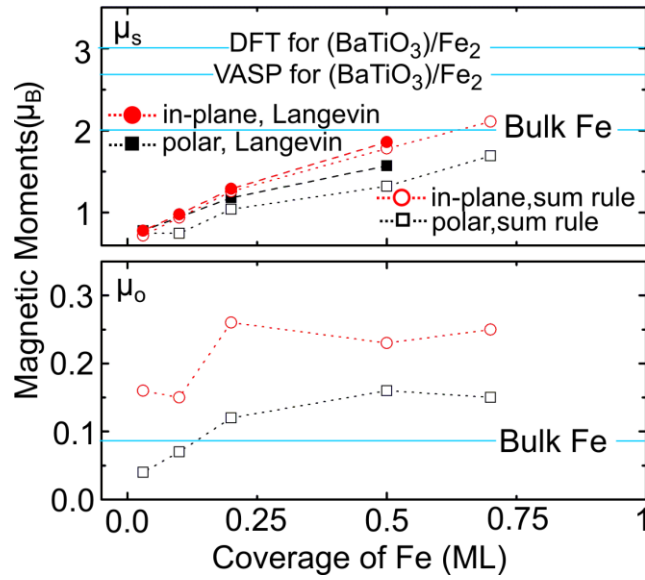


Fig. 5.5: The magnetic moments of Fe films calculated by sum rule (red open circle and black open square) and the saturation moments by using Langevin function (red filled circle and black filled square).

The experimentally determined spin and orbital moments are shown in Fig. 5.5. Through the entire comparison range studied below 0.75 ML Fe, the spin moments μ_s for the in-plane geometry (red open rectangle) are larger than those of the polar geometry (black open rectangle). It indicates that the Fe impurities have an in-plane easy axis. This is also confirmed by comparing hysteresis loops of the two geometries in Fig. 5.4. Moreover, orbital moments μ_o in Fig. 5.5 are larger in the in-plane direction than in the polar direction, which is consistent with the observation of the magnetization [134]. The orbital moments μ_o in Fig. 5.5(b) are larger than bulk value [133]; the ratios of μ_o / μ_s in both polar and in-plane directions for all of the films are in the wide range of 5~25%, which are larger than that of bulk Fe, ~4% [133]. The increased orbital moments found at this low coverage reflects the cluster formation and the high population of low

coordinated sites such as edge sites in the clusters, which is known to result in an enhancement of the orbital moment due to reduced symmetry around the sites. By comparison, however, the absolute values of the orbital moments are lower than the moment found in Fe clusters deposited on other substrates, such as on Cu(100) [135].

Next, the properties of Fe clusters deposited with BLAG approach on BaTiO₃ film will be discussed. The key idea is to suppress interface mixing and oxidization by deposition of less reactive large clusters. The morphology of the Fe clusters with different Fe coverage and different Xe layer thickness is investigated by STM and the results are shown in Fig. 5.6.

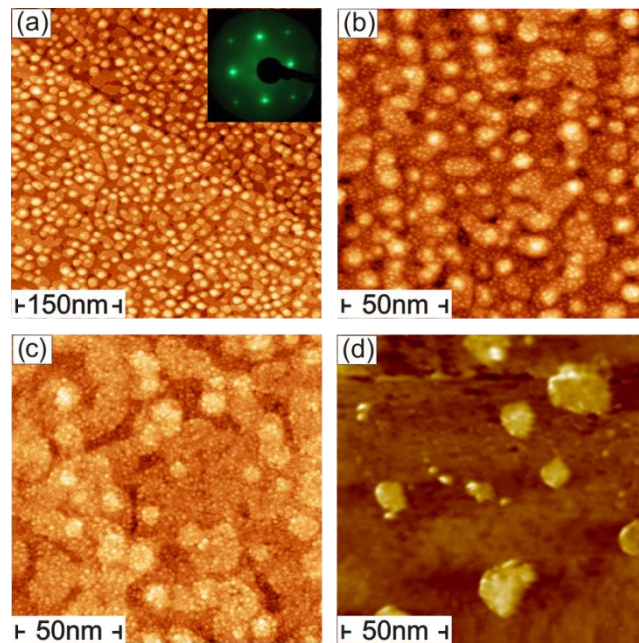


Fig. 5.6: STM images of BaTiO₃ substrate before and after Fe deposition. (a) 13 u.c. BaTiO₃ substrate, (inset: LEED image at 75 eV), (b) 0.2 ML Fe on BaTiO₃ with 100L Xe layer, (c) 2 ML Fe on BaTiO₃ with 100 L Xe layer, and (d) 2 ML Fe grown with 1000 L Xe layer.

A 13 u.c. thin BaTiO₃ film is available as a substrate for the growth studies. As previously discussed [section 3.3.1] and shown in Fig. 5.6(a), the 13-unit-cell BaTiO₃ film exhibits three-dimensional (3D) island formation due to strain-driven transition. The sharp 1×1 LEED pattern taken at 75 eV confirms that the BaTiO₃ film is crystalline and unreconstructed. In Fig. 5.6, the images shows the Fe cluster morphology for different Fe coverage and Xenon layer thickness, including 0.2 ML with 100 L Xe (b), 2 ML with 100 L Xe (c) and 2 ML with 1000 L Xe (d), respectively. One Langmuir Xe is defined by 1 second exposure of Xe at pressure of 1×10^{-6} Torr. Studies for other methods combinations have shown that 5.5 L of exposure are required to form 1 ML of Xe [136]. When the Fe sample is prepared using 100 L Xe buffer layer, the clusters are found to be of hemispherical shape. The Fe clusters are 2--3 nm in diameter and 2--5 Å at height. While Fe clusters prepared with 1000 L Xe buffer layer, the clusters are found 15 ~ 30 nm in diameter and 0.9 nm ~1.6 nm at height.

The magnetic properties of Fe clusters grown by buffer-layer assisted approach have again been studied by XMCD measurements. XAS spectra have been recorded for Fe films with two thicknesses. Fig. 5.7 shows the normalized XAS, and XMCD spectra of 2 ML and 4 ML Fe clusters grown on 13 u.c. BaTiO₃ with 500 L Xe buffer layer. For both Fe thicknesses the spectra show two distinctive peaks corresponding to transitions of $2p_{3/2}$ and $2p_{1/2}$ electrons into the 3d valence band. L₃ edge peak is located at 708 eV for both 2 ML and 4 ML Fe samples, which is a typical peak position of metallic character for Fe. There is a noticeable shoulder peak at the 2 ML Fe coverage, see Fig. 5.8. It is the result of an additional, small peak of energy at energy 709 eV. This peak corresponds to

the Fe in the oxide form, such as FeO. Fitting the XAS spectra with a 2-peak fit gives an estimate of the level of oxidization. Such a multiple peak fit of the 2 ML spectra results in the peak ratio between Fe oxide and Fe is about 1:3, as shown in Fig. 5.8. Comparison the fit with known Fe oxide spectra [131,132], it is concluded that about 25% of Fe is oxidized.

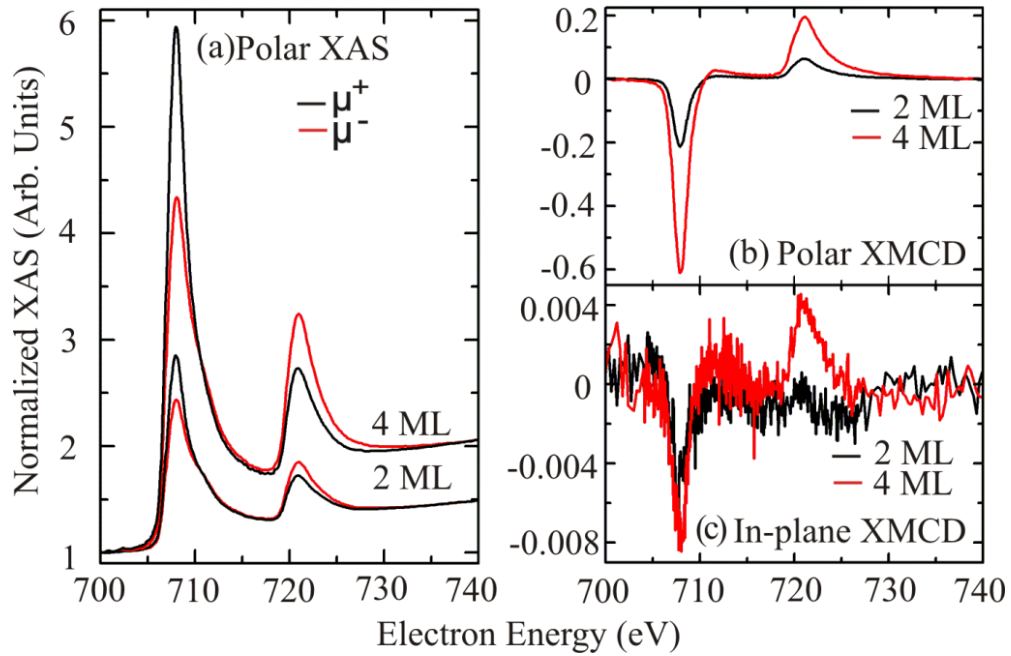


Fig. 5.7: XAS and XMCD spectra of Fe L-edge of 2.0, 4.0 ML Fe deposited on BaTiO₃ film with 500 L Xe layer. (a) polar XAS, (b) polar XMCD, and (c) in-plane XMCD.

Fig. 5.7 (b) and (c) show the XMCD spectra for 2 ML and 4 ML Fe coverage along polar and in-plane direction, respectively. The XMCD spectra in Fig. 5(b, c) illustrate that Fe clusters in both samples exhibit pronounced out-of-plane easy magnetization axis. Assuming magnetic saturation along the out-of-plane direction, the sum rules are again applied to determine spin and orbital moments, as illustrated in section 2.4. For 2 ML Fe coverage, the spin and orbital moments along polar direction are

$1.04 \mu_B$ and $0.05 \mu_B$, respectively; the XMCD signal along in-plane direction is too weak to determine accurate values for the spin and orbital moments. For 4 ML Fe coverage, the spin and orbital moment along polar direction are $1.75 \mu_B$ and $0.06 \mu_B$, respectively. The increase of the moment for 4 ML Fe sample is ascribed to larger Fe 3D clusters by buffer-layer assisted growth for higher Fe coverage; hence their magnetic properties are closer to bulk Fe.

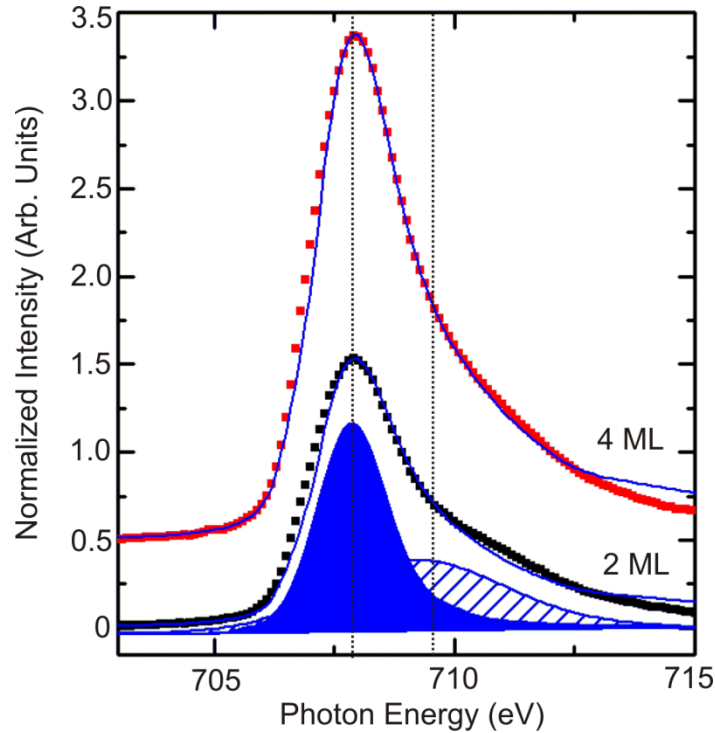


Fig. 5.8: XAS near L_3 -edge of Fe clusters deposited by buffer layer assisted growth. The dotted curves are experimental data and the solid lines are the curve fitting. The dash lines are the peak energies of Fe and Fe oxide for the curve fitting.

Table 5.1: Spin and orbital moments for 2ML and 4ML Fe clusters. They are deposited on BaTiO₃ films by buffer-layer assisted growth with 500 L Xeon.

Fe (ML)	Polar		In-plane	
	$\mu_s(\mu_B)$	$\mu_o(\mu_B)$	$\mu_s(\mu_B)$	$\mu_o(\mu_B)$
2.0	1.04	0.05	-	-
4.0	1.75	0.06	0.22	0.03

Extended Fe films in the thin film limit often show perpendicular magnetic easy axis due to the dominance of surface magnetic anisotropy, for example, Fe/W(110) [137] and Fe/Cu(001) [138]. First Principles calculations for 1 ML Fe film on BaTiO₃(001) also predict the perpendicular easy axis [83,84], which is contradictory to our experimental observation. This discrepancy between theory and experiment may be explained by the lattice strain which is created by low temperature deposition. When the Fe is deposited on BaTiO₃ film at 10 K, its low ad-atom mobility generates large epitaxial strain, which contributes to the total magnetic energy via the magneto-elastic coupling. The final magneto anisotropy energy is the balance between shape magneto-static energy and magneto-elastic energy. The key difference between Fe films grown with low temperature MBE method and Fe films grown with BLAG approach seems to be the amount of strain in the Fe, due to the difference in the synthesis. Thus, the highly strained and disordered Fe films obtain by MBE at 10 K could have a magneto-elastic anisotropy contribution that favors in plane easy axis. By contrast, BLAG grown clusters are structurally more relaxed, so that the magneto-elastic anisotropy is reduced and the total anisotropy is out of plane from interface contribution. MBE-grown Fe submonolayer islands have the easy magnetization axis in plane, while the BLAG-grown clusters have out-of-plane easy axis. It has been shown in several other studies that strain can alter the

easy magnetization axis [139] and it is proposed here that strain again is of the origin of the different in the MAE.

5.4 Conclusion

The growth and magnetic properties of Fe ad-layers have been investigated. Fe impurities and clusters are prepared via three deposition methods on 13 u.c. BaTiO₃ substrate, which are MBE growth at room temperature, MBE growth at 10 K and buffer-layer assisted growth. In the MBE growth at 10 K, the Fe impurities favor the in-plane easy axis and the magnetic moment per Fe atom monotonically increases with Fe coverage, and it reaches that of bulk Fe only for the coverage between 0.5 and 0.7 ML. In the buffer-layer assisted growth, the Fe forms large 3D cluster with out-of-plane easy axis. The different easy axes in two systems are ascribed to the epitaxial strain in Fe during different growth method. High epitaxial strain is expected in MBE growth a low temperature and it results in in-plane easy axis; while relaxed Fe clusters are formed in BLAG method and it leads to out-of-plane easy axis. Two strategies have been established to suppress the oxidation of Fe impurities and clusters deposited on BaTiO₃ thin films: MBE growth at 10 K and BLAG approach. This study paves the way for future investigation of interfacial magneto-electric effect.

Chapter 6

Ordered Layers of Co Clusters on BN Template Layers

6.1 Introduction

This is another example for magnetic nanostructure growth on thin film surfaces, using a completely different approach. The surface will be only 1 nm thin and it will act as a template for nanostructures. This section focuses on the positioning of nanoclusters at surfaces as a key challenge in nanotechnology and as a specific requirement in bit-patterned magnetic recording [140]. Experimental approaches for the fabrication of ordered nanoparticle layers center around the deposition of nanoclusters from the liquid phase [141], the soft landing from the gas phase [142], and the directed self-assembly on template surfaces [143,144]. While the first two approaches give only little control over the position of the clusters per se, as seen also in chapter 5, the latter has the advantage that the lateral arrangement of the particles can be controlled precisely by using template surfaces. Such surfaces provide well-defined energetic sinks with subnanometer accuracy to guide the nucleation processes and diffusion of atoms, and to form nanostructures or clusters at specific sites. A number of templates, including reconstructed surfaces [145], strain-relief patterns [146], or supramolecular architectures [147], have been used recently to fabricate nanoparticle arrays [148]. It is generally found that the directed growth works well for very specific film/substrate systems but does not represent a generic approach for the synthesis of ordered nanoparticle layers. An alternative approach is to deposit metal clusters by noble-gas buffer combines the advantages of template-

assisted growth with the versatility of cluster deposition. Metal clusters have been fabricated in this work by noble-gas buffer-layer assisted growth (BLAG) directly on flat surfaces [129]. Since BLAG permits, in principle, the deposition of any material on any substrate [149,150], this approach has the potential to be applicable to many other metallic or nonmetallic materials.

Analytical model calculations and Monte-Carlo simulation are performed to analyze the cluster coverage as a function the number of deposition cycles and the real-space distribution of the Co particles on template BN surface. It shows that the approach to full coverage critically depends on the interactions between particles and exhibits a critical slowing down for some interaction strength. Good agreement with experiment is achieved by including the assimilation of a small portion of newly deposited clusters by clusters deposited during preceding BLAG cycles.

6.2 Experimental aspects specific to these studies

Mechanically stable boron-nitride (BN) monolayers are used as templates for the fabrication of ordered layers of metal clusters. The *h*-BN layers are atomically thin, electrically insulating, chemically inert, mechanically extremely stable, and show a strain-driven hexagonally ordered corrugation with a periodicity of 3.2 nm [151,152]. Such BN layers are commonly referred to as *nanomesh* but they rather resemble the shape of a muffin tin. The difference in height between the attached areas (depressions) and the detached ridges is approximately 0.55 Å [153]. The cobalt nanoclusters were

fabricated directly at the BN layer by BLAG. The preparation steps can be found in section 5.2. Clusters of 1–3 nm in diameter are achieved by using approximately 2 monolayers (ML) of Xe and 3%–5% of a full monolayer of Co.

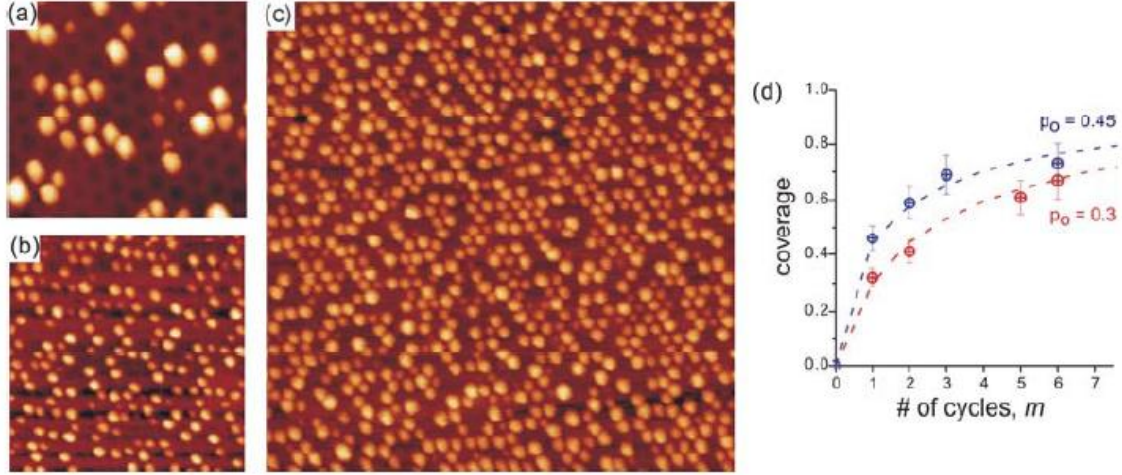


Fig. 6.1: Increase of the occupation of the BN layer with Co clusters by repeated BLAG cycles. (a) STM images after one BLAG cycles (5% Co/5L Xe) (30 nm x 30 nm) (b) after 2 BLAG cycles (50 nm x 50 nm), (c) after 3 BLAG cycles (100 nm x 100 nm), (d) analysis of the BN occupation, for 3% of a ML Co/5L Xe per cycle (red) and 5% of a ML Co/5L Xe per cycle (blue). The dashed lines are from an analytical model in equation (6.2), with $\lambda = 1.05$ and values of p_0 corresponding to the coverages at $m = 1$. [154]

With the deposition parameters $\theta_{Co} = 0.05 \text{ ML}$ and $\theta_{Xe} = 5 \text{ L}$, about 30% of the depressions in the BN layer are filled by one BLAG cycle, as shown in the STM image in Fig. 6.1(a). The number of the clusters deposited per area can be controlled, to some extent, by varying experimental parameters but depression occupancies beyond 40% are difficult to achieve in a single BLAG cycle. In order to fabricate ordered cluster layers with BN layer occupations approaching the ideal value of 100% (full coverage), the BLAG cycles are repeated several times. The fraction of occupied depressions gradually increases, and after three subsequent BLAGS cycles approximately 70% of the depressions are occupied [Fig. 6.1(c)]. Figure 6.1(d) shows the occupation of the

nanomesh as function of the number m of deposition cycles for two samples: 3% of a ML Co on 5 L Xe (red) and 5% of a ML Co on 5 L Xe (blue) per BLAG cycle. It appears that larger amounts of Co per cycle help in filling the BN layer more quickly. However, more Co per cycle results also in larger clusters, and the presence of larger clusters impedes their ordered arrangement is shown later. This might be due to decreased mobility of the clusters with increased volume, or simply a geometrical on-site repulsion problem if the clusters' diameters exceed the distance between the centers of neighboring depressions on the BN layer.

6.3 Modeling and Simulation

To analyze the cluster coverage as a function of the number of deposition cycles and the real-space distribution of the particles, analytical model calculations and Monte Carlo (MC) simulations are performed. In the simplest model, the particles arriving on the surface occupy a fraction p of the empty depressions so that the coverage c_m after the m_{th} cycle is given by the discrete rate equation,

$$c_{m+1} = c_m + p(1 - c_m) \quad (6.1)$$

Subject to the initial condition $c_0 = 0$, the solution of this equation is $c_m = 1 - (1 - p)^m$. By considering $m = \infty$, this equation predicts an approach to complete coverage ($c_\infty = 1$), which seems in contradiction to the experiment [Fig. 6.1(c)]. Physically, a fraction of the arriving particles tend to be attracted by occupied pits (clusters). Little is known about the details of this attraction but it probably reflects the mobility of the particles in the noble-gas matrix and at the surface during Xe desorption.

The effect exhibits a subtle dependence on an attraction parameter λ so that magnetic interactions between particles may be important, as well.

To describe the attraction effect, the probability p is assumed to depend on the coverage of the nanomesh. A certain fraction of the particles that arrive at empty depressions are diverted toward filled ones. This means that some of the deposited clusters coalesce with newly deposited clusters during a BLAG cycle and thus grow in size. In the present model, this effect is assumed to be linear in the coverage, $p = p_0(1 - \lambda c_m)(1 - c_m)$. Equation (6.1) now becomes

$$c_{m+1} = c_m + p_0(1 - \lambda c_m)(1 - c_m) \quad (6.2)$$

In real space, λ describes an excluded volume around occupied sites (clusters) and a large λ means that deposited clusters are very efficient in capturing particles arriving in their vicinity and preventing the occupancy of neighboring empty sites. In experiment, the number of deposited clusters always increases monotonically, which means that λ is always smaller than $1/p_0$.

Equation (6.2) is solved very easily by numerical iteration. Figure 6.2(a) shows the calculated coverage as a function of the number m of deposition cycles. For small concentrations c_m , that is, for small p_0 or m , the solution of Eq. (6.2) is exponential. However, the extrapolated maximum coverage is reduced, $c_\infty = 1/(1 + \lambda)$, and the approach to saturation is slower. Qualitative deviations from Eq. (6.1) occur as c_m approaches c_∞ and the extrapolated value $c_\infty = 1/(1 + \lambda)$ is actually a very poor estimate.

Figure 6.2(b) shows the coverage as a function of the attraction parameter. According to Eq. (6.2) the c_m cannot increase further if it becomes $c_m=1/\lambda$. The λ defines thus also a critical coverage above which *all* of the clusters arriving at the surface during a BLAG cycle are assimilated by previously deposited clusters. Therefore, critical behavior at $\lambda=1$ is determined. For values $\lambda<1$, the occupied pores reduce the deposition rate but leave the maximum coverage unchanged ($c_\infty = 1$). For $\lambda > 1$, the maximum coverage becomes <1 . This is of great practical importance because it means that seemingly small changes in deposition conditions can make the difference between complete and incomplete coverages. Matching the experimental data of the BN coverage in Fig. 6.2(d) with the function in Eq. (6.2) requires $\lambda = 1.05$; thus the maximum possible coverage for this system under the present preparation conditions is $c_\infty = 0.95$.

The case $\lambda = 1$ exhibits an interesting slowing down as the coverage approaches $c_\infty = 1$. The slow approach to saturation is clearly visible in Fig.6.2(a), where both the black and the red lines approach $c_\infty = 1$ but the red line exhibits a non-exponential convergence. By putting $\lambda = 1$ in Eq. (6.2), it is easy to show that the approach to saturation obeys the power law $p_0(1 - c_m) = 1/m$. This equation is obtained by putting $\lambda = 1$ in Eq. (6.2), replacing $c_{m+1} - c_m$ by dc/dm , and integration of the resulting differential equation. For λ values slightly smaller than one, the system exhibits a pre-asymptotic power-law approach, followed by an exponential approach to saturation with an effective deposition rate $p_{eff} = (1 - \lambda)p_0$. In other words, the coverage increases slowly but approaches full coverage in an exponential manner. Note that the present regimes are

different from well-known mechanisms such as Langmuir and Brunauer-Emmett-Teller (BET) adsorptions [155]. The latter are based on equilibrium thermodynamics, whereas the present absorption mechanism is partially of the first-passage type—where particles are allowed to stick to each other so that only a part of the full phase space is explored.

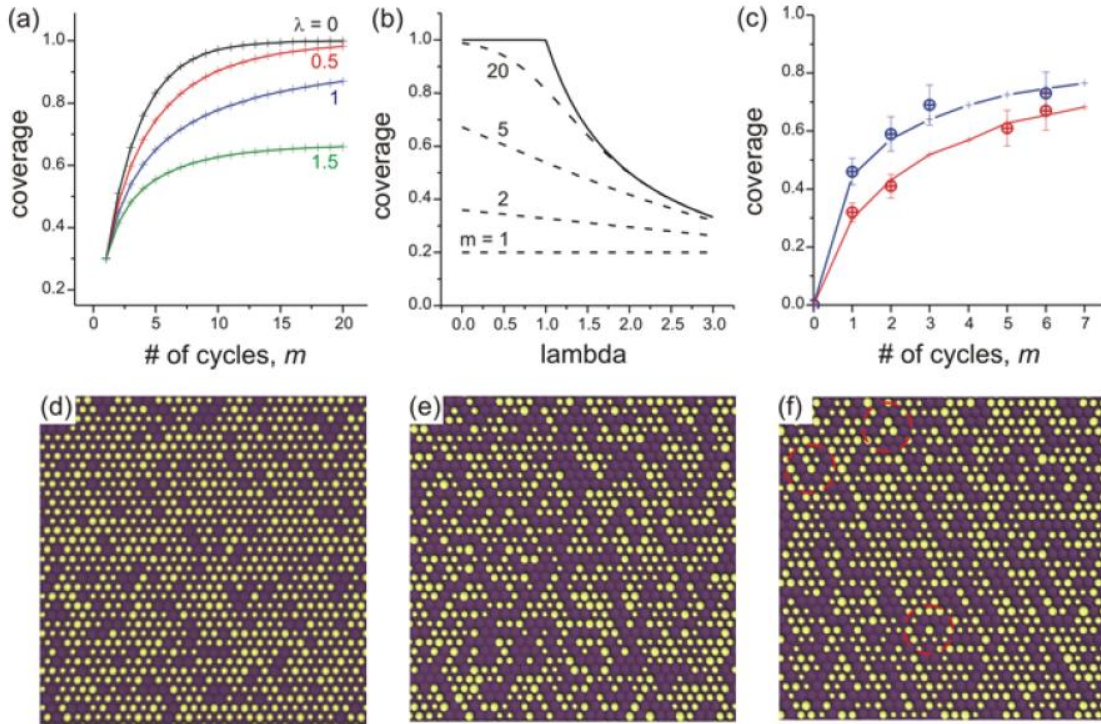


Fig. 6.2: Models of the BN occupation. (a, b) Analytical model, assuming attractive interaction between clusters, which leads to a slowing down of the BN layer filling for $\lambda > 0$, and a decrease of the maximum possible cluster coverage for $\lambda > 1$. (c-f) Monte-Carlo simulations of the BN occupation. The experimental data from Fig. 6.1(c) can be reproduced by assuming exponential volume-dependence of the attraction parameter λ , $V_c = 5.0$, $c_0 = 0.3$ (red) and $c_0 = 0.3$ (blue) (c). Visualization of the BN layer occupation with clusters (yellow), without cluster hopping to a neighboring site (d), with constant hopping probability (e) and a hopping probability that depends exponentially on the volume of the neighboring cluster (see text) (f). Encircled in red are some clusters that grew large by merging with their neighbors.

The model of Eq. (6.2) describes the coverage as a function of the number m of deposition cycles but does not explain the nanomesh occupation qualitatively. To reproduce the effect of the attractive cluster-cluster interaction on the lateral distribution, a Monte Carlo simulation is used. It is assumed that an integer number p_0 of clusters of unit volume are randomly distributed onto the discrete positions of a hexagonal lattice with each deposition cycle. After assigning those clusters to preliminary lattice sites, they are treated according to the following two rules. First, if a site is already occupied due to a preceding deposition cycle, then the new cluster is simply attached to the existing cluster, whose size is consequently enlarged by one unit volume. Second, if the site is empty, then the cluster is allowed to hop to a nearest-neighbor site i with a certain probability η_i and to merge with the cluster occupying the neighboring site unless it is empty. This process implies some mobility of the clusters at some point during the deposition and attractive cluster-cluster interaction, as also assumed in Eq. (6.2). A direct consequence is that the average cluster size increases linearly with every deposition step, something that can clearly be deduced from the STM images.

Figures 6.2(d)–(f) show the results of MC simulations, all after three deposition steps with $p_0=0.45$. In Fig. 6.2(d), no hopping of clusters after deposition was permitted, and the BN layer occupation is 90%. Hopping was permitted in the simulation in Fig. 6.2(e), based on the simple constant probability rule that a cluster merges with a randomly chosen cluster in its nearest neighborhood. Figure 6.2(e) shows the result of a simulation using $p_0 = 0.45$ and the probability $\eta = 0.65$, as these parameters give best agreement with the experimental data for $c(m)$ in Fig. 6.2(d). Figure 6.2(f) shows the

result of a simulation where η was assumed to be dependent on the volume V_i of the clusters in its six nearest-neighbor sites ($i=1-6$). The linear and exponential volume dependencies of η ,

$$\eta_i^{linear} = (V_i + n) / \sum_{k=1}^6 (V_k + n), \quad (6.3a)$$

$$\eta_i^{exp} = \exp\left(\frac{V_i}{V}\right) / \sum_{k=1}^6 \exp\left(\frac{V_k}{V}\right), \quad (6.3b)$$

give similar results. In Eq. (6.3), V_i is the volume of the i th cluster in direct neighborhood of a newly deposited cluster, V_c is a critical volume, and n is a constant. Both V_c or n can be used as fit parameters to describe the experimental data [Fig. 6.2(c)]. The BN coverages in Figs. 6.2(e) and (f) are 0.63 and 0.64, respectively. The radii r of the circles representing the clusters in Fig. 6.2 reflect their volume according to $r \sim V^{1/3}$. While the integral cluster volume is the same in all three simulations [Figs. 6.2(d)–(f)], the BN layer occupation is visibly reduced by the introduction of attractive cluster interaction.

The simulation based on the volume-dependent assimilation model reproduces the experimentally found coverage c_m [Fig. 6.2(c)], the formation of empty channels of one depression diameter in width on the BN, the existence of very large, isolated clusters, and the measured cluster size as function of m . As far as the c_m is concerned, the MC predictions are very similar to those derived from Eq. (6.2) [compare Figs. 6.2(d) and 6.2(c)].

6.4 Conclusion

Repeated buffer-layer assisted growth of Co clusters on BN template surface by is demonstrated as another example of creating nanostructures on thin film surface that combines the versatility of the cluster deposition from the gas phase with the positional accuracy of directed, self-assembled growth. The experimental Co cluster coverage as a function of the number of deposition cycles and the real space distribution of the Co clusters on template BN surface are analyzed by analytical model calculations and Monte-Carlo simulations. The assimilation of a small portion of newly deposited clusters by clusters deposited during repeating BLAG cycles in the simulation yields a good agreement with experiment. However, the chosen experiment and studies are a step in the direction of directed cluster arrangement on surfaces as compared to the random cluster layers in Chapter 5. This is therefore a sharing point for related studies aiming at the fabrication of ordered cluster layers by self-assembly.

Chapter 7

Conclusions

A comprehensive study of ultrathin oxide films as templates for magnetic nanostructures is presented in this thesis. Several important fundamental questions with regards to oxide thin films have been addressed experimentally using a surface science method. The local surface structure and electronic properties of ultrathin oxide films, as well as magnetic ad-layers, have been investigated by scanning tunneling microscopy/spectroscopy. Furthermore, the local characterization of ferroelectric properties of oxide thin films has been demonstrated by local point spectroscopy measurements using STM for the first time.

The studies have been focused on two examples of ultrathin oxide films: barium titanate film (BaTiO_3) and chromium oxide film (Cr_2O_3). The first example, ultrathin BaTiO_3 films, has been discussed in Chapter 3. It is shown that nanometer thin films of BaTiO_3 exhibit atomically smooth surface terraces of unit cell height, the absence of surface reconstruction, stoichiometric surface, well-behaved ferroelectric properties, and dominantly TiO_2 surface terminations. These high-quality surfaces of BaTiO_3 can be recovered after sample transfer through the air and it simplifies the sample preparation. These high quality films are used as templates for the study of magnetic properties of the ferromagnetic metal ad-layers in Chapter 5. Two strategies have been established to

suppress the oxidation of Fe impurities and clusters deposited on BaTiO₃ thin films: MBE growth at 10 K and BLAG approach. While Fe impurities and clusters are randomly distributed on flat surfaces, the Co clusters deposited on BN template surfaces by repeated BLAG growth demonstrates one example for achieving ordered nanostructure growth, as discussed in Chapter 6. As a second example of ultrathin oxide film, the growth and characterization of chromia films was presented in Chapter 4. Again, its local surface morphology and electronic properties were characterized by STM/STS, which are unavailable in other integral surface science techniques and NC-AFM.

Key outcomes of this thesis can be summarized as follows:

- High quality BaTiO₃ films can be achieved after sample transfer through air, by post-annealing sample in oxygen partial pressure.
- Switching and detecting of the polarization in BaTiO₃ films with STM have been demonstrated for the first time.
- Growth strategies have been identified that suppress the Fe oxidation during the growth of Fe adsorbates on BaTiO₃ films.
- Co-existence of multiple surface terminations on Cr₂O₃ films has been identified.
- The ordering of magnetic nanostructures by insulating template has been analyzed.

This thesis has shown how to apply scanning tunneling microscopy methods for the comprehensive study of the structure, morphology, and electronic properties and dielectric properties of thin oxide films. This is a remarkable result, since STM usually

requires conducting sample under standard operation. It has been shown that STM can be useful to obtain information, for instance the local electronic structure, that other scanning probe methods, such as AFM, cannot achieve,. Especially, the demonstration of polarization switching is new.

The high quality of the oxide films and metal-oxide interface obtained are expected to have a stimulating effect on related studies in the field and will help the development of functional metal/oxide hybrid materials for applications in oxide electronics. While this study has been successful in preparing suitable structures that potentially can show various magneto-electric effects, such effects have not been studied up to now. For future research, additional experiments to investigate the magnetism of the Fe ad-layers as a function of substrate polarization are suggested. Such studies would mostly rely on the XMCD effect, that is best performed at a synchrotron facility. Access to such facilities requires participation in a user proposal competition, typically at European facilities where the required UHV facilities and magnetic fields are available. Because of the limited access there for American research groups, such measurements could not be performed within the work for this thesis.

Bibliography

- [1] J. Nowotny, Science of Ceramic Interface in Materials Science Monographs (Elsevier, New York, 1993), Vol. 81
- [2] M. Rühle, A. G. Evans, M. F. Ashby, and J. P. Hirth, Metal-Ceramic Interfaces (Pregamon, New York, 1990)
- [3] H. H. Kung, Transition Metal Oxides: Surface Chemistry and Catalysis (Elsevier, New York, 1989)
- [4] G. Pacchioni, Chem. Eur. J. 18, 10144 (2012)
- [5] R. A. Miller, J. Thermal Spray Technol. 6, 35 (1997)
- [6] E. P. Gusev, in: Defects in SiO₂ and related dielectrics: science and technology, (Eds.: G. Pacchioni, L. Skuja, D. L. Griscom), Kluwer, Dordrecht, p. 577 (2000)
- [7] R. Pentcheva, R. Arras, K. Otte, V. G. Ruiz, W.E. Pickett, *Phil. Trans. R. Soc. A* **370**, 4904 (2012)
- [8] J. Kim, L. J. Cote, and J. Huang, *Acc. Chem. Res.* **45**, 1356 (2012)
- [9] S. S. P. Parkin, C. Kaiser, A. Panchula, P.M. Rice, B. Hughes, M. Samant, S. H. Yang, *Nat. Mater.* **3**, 862 (2004)
- [10] C.G. Granqvist, *Solar En. Mater. & Solar Cell* **91**, 1592 (2007)
- [11] C. H. Ahn, K. M. Rabe, J. M. Triscone, *Science* **303**, 488 (2004)
- [12] P.C. Su, C.C. Chao, J. H. Shim, R. Fasching, F. B. Prinz, *Nano Lett.* **8**, 2289 (2008)

- [13] H. Lu, C. W. Bark, D. Esque de los Ojos, J. Alcal, C. B. Eom, G. Catalan, A. Gruverman, *Science* **336**, 59 (2012)
- [14] S. Sahoo, S. Polisetty, C.G. Duan, S. S. Jaswal, E. Y. Tsymbal, and C. Binek, *Phys. Rev. B* **76**, 092108 (2007)
- [15] X. He, Y. Wang, N. Wu, A. N. Caruso, E. Vescovo, K. Belashchenko, P. Dowben, and C. Binek, *Nat. Mater.* **9**, 579 (2010)
- [16] S. Altieri, L. H. Tjemg, G. A. Sawatzky, *Thin Solid Films* **400**, 9 (2001)
- [17] R. Schintke, W. D. Schneider, *J. Phys. Condens. Matter.* **16**, R49 (2004)
- [18] C. Feryesoldt, P. Rinke, M. Scheffler, *Phys. Rev. Lett.* **99**, 086101 (2007)
- [19] C. L. Pang, G. Thornton, *Surf. Sci.* **603**, 3255 (2009)
- [20] S. Förster, M. Huth, K. M. Schindler, and W. Widdra, *J. Chem. Phys.* **135**, 104701 (2011)
- [21] S. Dreiner, M. Schürmann, C. Westphal, and H. Zacharias, *Phys. Rev. Lett.* **86**, 4068 (2001)
- [22] D. G. Neerinck, T. J. Vink, *Thin Solid Films* **278**, 12 (1996)
- [23] A. I. Stadnichenko, A.M. Sorkin, and A. I. Boronin, *J. Structural Chem.* **49**, 341 (2008)
- [24] C. P. Huggins, and R. M. Nix, *Surf. Sci.* **594**, 163 (2005)
- [25] P. J. Chen, M. L. Colaianne, and J. T. Yates, *Phys. Rev. B* **41**, 8025 (1990)
- [26] G. Binning, H. Rohrer, Ch. Gerber, E. Weibel, *Phys. Rev. Lett.* **49**, 57 (1982)
- [27] P. Avouris and R. Wolkow, *Appl. Phys. Lett.* **55**, 1074 (1989)
- [28] M. F. Crommie, C. P. Lutz, and D. M. Eigler, *Nature* **363**, 524 (1993)

- [29] M. Ternes, A. J. Heinrich, and W. D. Schneider, *J. Phys.: Condens. Matter* **21**, 053001 (2009)
- [30] M. Bode, *Rep. Prog. Phys.* **66**, 523 (2003)
- [31] G. Rojas, X. Chen, J. Xiao, P.A. Dowben, and A. Enders, *Phys. Chem. Chem. Phys.* **14**, 4971 (2012)
- [32] R. Sonnenfeld and P. K. Hansma, *Science* **232**, 211 (1986)
- [33] R. Sonnenfeld, J. Schneir, and P. K. Hansma, *Modern Aspects of Electrochemistry* **21**, 1 (1990)
- [34] Y. J. Song, A. F. Otte, Y. Kuk, Y. Hu, D. B. Torrance, P. N. First, W. A. de Heer, H. Min, S. Adam, M. D. Stiles, A. H. MacDonald, and J. A. Stroscio, *Nature* **467**, 185 (2010)
- [35] D. Peterka, A. Enders, G. Haas, and K. Kern, *Rev. Sci. Instrum.* **74**, 2744 (2003)
- [36] R. Schaub, E. Wahlström, A. Ronnau, E. Lagsgaard, I. Stensgaard, F. Besenbacher, *Science* **299**, 377 (2003)
- [37] J. Tersoff and D. R. Hamann, *Phys. Rev. Lett.* **50**, 1998 (1983)
- [38] A. Selloni, P. Carnevali, E. Tosatti, and C. D. Chen, *Phys. Rev. B* **31**, 2602 (1985)
- [39] C. J. Chen, *Introduction into Scanning Tunneling Microscopy* (Oxford University Press, 2008)
- [40] http://depts.washington.edu/nanolab/NUE_UNIQUE/Lab_Units/5_Lab_Unit_STM.pdf
- [41] M. Ternes, A. J. Heinrich, and W.D. Schneider, *J. Phys.: Condens. Matter* **21**, 053001 (2009)
- [42] O. Pietzsch, A. Kubetzka, M. Bode, and R. Wiesendanger, *Phys. Rev. Lett.* **92**, 057202 (2004)

- [43] L. Diekhöner, M. A. Schneider, A. N. Baranov, V. S. Stepanyuk, P. Bruno, and K. Kern, *Phys. Rev. Lett.* **90**, 236801 (2003)
- [44] A. L. Vazquez de Parga, F. J. Garcia-Vidal, and R. Miranda, *Phys. Rev. Lett.* **85**, 4365 (2000)
- [45] O. Jeandupeux, L. Bürgi, A. Hirstein, H. Brune, and K. Kern, *Phys. Rev. B* **59**, 15926 (1999)
- [46] J. Li, W.D. Schneider, S. Crampin, and R. Berndt, *Surf. Sci.* **422**, 95 (1999)
- [47] S. Pons, P. Mallet, and J. Y. Veuillen, *Phys. Rev. B* **64**, 193408 (2001)
- [48] J. C. Slonszewski, *Phys. Rev. B* **39**, 6995 (1989)
- [49] M. Sico, O. Kurnosikov, O. A. O. Adam, H. J. M. Swagten, and B. Koopmans, *Phys. Rev. B* **77**, 035417 (2008)
- [50] O. Pietzsch, S. Okatov, A. Kubetzka, M. Bode, S. Heinze, A. Lichtenstein, and R. Wiesendanger, *Phys. Rev. Lett.* **96**, 237203 (2006)
- [51] T. Hänke, S. Krause, L. Berbil-Bautista, M. Bode, and R. Wiesendanger, *Phys. Rev. B* **71**, 184407 (2005)
- [52] M. Kleiber, M. Bode, R. Ravlic, and R. Wiesendanger, *Phys. Rev. Lett.* **85**, 4606 (2000)
- [53] H. Hövel, I. Barke, *Prog. Surf. Sci.* **81**, 53 (2006)
- [54] U. Kreibig, W. Vollmer, Optical Properties of Metal Clusters, in: Springer Series Materials Science, Vol. 25, Springer, Berlin, 1995
- [55] N. Nilius, *Surf. Sci. Rep.* **64**, 595 (2009)
- [56] P. A. Cox, Transition Metal Oxides, Clarendon Pr., Oxford, 1992

- [57] T. Maroutian, S. Degen, C. Becker, K. Wandelt, and R. Berndt, *Phys. Rev. B* **68**, 155414 (2003)
- [58] G. Binnig, K. H. Frank, N. Garcia, B. Reihl, H. Rohrer, F. Salvan, and A. R. Williams, *Phys. Rev. Lett.* **55**, 991 (1985)
- [59] M. R. Castell, P. L. Wincott, N. G. Condon, C. Muggelberg, G. Thornton, S. L. Dudarev, A. P. Sutton, G. A. D. Briggs, *Phys. Rev. B* **55**, 7859 (1997)
- [60] F. Esch, S. Fabris, L. Zhou, T. Montini, C. Africh, P. Fornasiero, G. Comelli, R. Rosei, *Science* **309**, 752 (2005)
- [61] U. Diebol, *Surf. Sci. Rep.* **48**, 53 (2003)
- [62] Y. Wang, B. Meyer, X. Yin, M. Kunat, D. Langenberg, F. Träger, A. Birkner, C. Wöll, *Phys. Rev. Lett.* **95**, 266104 (2005)
- [63] D. A. Bonnell, *Prog. Surf. Sci.* **57**, 187 (1998)
- [64] A. Gruverman, D. Wu, H. Lu, Y. Wang, H. W. Jang, C. M. Folkman, M. Ye. Zhuravlev, D. Felker, M. Rzechowski, C.-B. Eom and E. Y. Tsymbal, *Nano Lett.* **9**, 3539 (2009)
- [65] S. Datta, W. Tian, S. Hong, R. Reifenberger, J. I. Henderson, C. P. Kubiak, *Phys. Rev. Lett.* **79**, 2530 (1997)
- [66] S. W. Wu, G. V. Nazin, X. Chen, X. H. Qui, W. Ho, *Phys. Rev. Lett.* **93**, 236802 (2004)
- [67] R. M. Feenstra, *Phys. Rev. B* **50**, 4561 (1994)
- [68] G. Kresse, M. Schmid, E. Napetschnig, M. Schshkin, L. Köhler, P. Varga, *Science* **308**, 1440 (2005)
- [69] I. Sebastian, H. Neddermeyer, *Surf. Sci.* **454**, 771 (2000)

- [70] K. H. Hansen, T. Worren, E. Laegsgaard, F. Besenbacher, I. Stegsgaard, *Surf. Sci.* **475**, 96 (2001)
- [71] K. Meinel, A. Eichler, K. M. Schindler, H. Neddermeyer, *Surf. Sci.* **562**, 204 (2004)
- [72] T. Bertranms, A. Brodde, H. Neddermeyer, *J. Vac. Sci. Technol. B* **12**, 2122 (1994)
- [73] T. Bertranms, Ph.D. thesis, Ruhr-Univeristät, Bochum, 1996
- [74] <http://www.omicron.de/en/products/low-temperature-spm/downloads>
- [75] SPIPTM software, Image Metrology A/s (Denmark), www.imagemet.com
- [76] J. Stohr, H.C. Siegmann, *Magnetism--from Fundamentals to Nanoscale Dynamics*, vol. 152, Springer, Berlin, 2006
- [77] B.T. Thole, P. Carra, F. Sette, G. V. D. Laan, *Phys. Rev. Lett.* **68**, 1943 (1992)
- [78] C. T. Chen, Y. U. Idzerda, H. J. Lin, N. V. Smith, G. Meigs, E. Chaban, G. H. Ho, E. Pellegrin, F. Sette, *Phys. Rev. Lett.* **75**, 152 (1995)
- [79] C. Ederer, M. Komelj, and M. Fähnle, *Phys. Rev. B* **68**, 052402 (2003)
- [80] C. Ederer, M. Komelj, and M. Fähnle, *Phys. Rev. B* **68**, 052402 (2003)
- [81] R. Ramesh and N. A. Spaldin, *Nature Materials* **6**, 21 (2007)
- [82] M. Bibes, *Nature Materials*, **11**, 354 (2012)
- [83] C.G. Duan, S. S. Jaswal, and E.Y. Tsymlal, *Phys. Rev. Lett.* **97**, 047201 (2006)
- [84] C.G. Duan, J. P. Velez, R. F. Sabirianov, W.N. Mei, S. S. Jaswal, and E. Y. Tsymlal, *Appl. Phys. Lett.* **92**, 122905 (2008)

- [85] T. Dimopoulos, V. Costa, C. Tiusan, K. Ounadjela, H. A. M. van den Berg, *Appl. Phys. Lett* **79**, 3110 (2001)
- [86] T. Shimitzu, H. Bando, Y. Aiura, Y. Haruyama, K. Oka, and Y. Nishimura, *Jpn. J. Appl. Phys.* **34**, L1305 (1995)
- [87] H. Bando, T. Shimitzu, Y. Aiura, Y. Haruyama, K. Oka, and Y. Nishimura, *J. Vac. Sci. Technol. B* **14**, 1060 (1996)
- [88] A. M. Kolpak, D. Li, R. Shao, A. M. Rappe, and D. A. Bonnell, *Phys. Rev. Lett.* **101**, 036102 (2008)
- [89] G. Rakotovelo, P. S. Moussounda, M. F. Haroun, P. Legaré, A. Rakotomahevitra, and J. C. Parlebas, *Eur. Phys. J. B* **57**, 291 (2007)
- [90] X. Y. Xue, C. L. Wang, and W. L. Zhong, *Surf. Sci.* **550**, 73 (2004)
- [91] L.A. Wills, Bruce W. Wessels, D.S. Richeson, and Tobin J. Marks, *Appl. Phys. Lett.* **60**, 41 (1992)
- [92] J. Shin, V. Nascimento, A.Y. Borisevich, E.W. Plummer, S. V. Kalinin, and A. P. Baddorf, *Phys. Rev. B* **77**, 245437 (2008)
- [93] H. Shigetani, K. Kobayashi, M. Fujimoto, W. Sugimura, Y. Matsui, and J. Tanaka, *J. Appl. Phys.* **81**, 693 (1997)
- [94] Y. Yoneda, K. Sakaue, and H. Terauchi, *Surf. Sci.* **529**, 283 (2003)
- [95] G.H. Lee, B. C. Shin, and I.S. Kim, *Mater. Lett.* **50**, 134 (2001)
- [96] F. Niu, and B. W. Wessels, *J. vac. Sci. Technol. B* **25**, 1053 (2007)
- [97] Y. S. Kim, D. H. Kim, J. D. Kim, Y. J. Chang, T. W. Noh, J. H. Kong, K. Char, Y. D. Park, S. D. Bu, J.-G. Yoon, and J.-S. Chung *Appl. Phys. Lett.* **86**, 102907 (2005)

- [98] A. Visinoiu, M. Alexe, H.N. Lee, D.N. Zakharov, A. Pignolet, D. Hesse, and U. Goesele, *J. Appl. Phys.* **91**, 10157 (2002)
- [99] A. Gruverman, and A. Kholkin, *Rep. Prog. Phys.* **69**, 2443 (2006)
- [100] V. Garcia, S. Fusil, K. Bouzehouane, S. Enouz-Vedrenne, N. D. Mathur, A. Barthelemy, and M. Bibes, *Nature* **460**, 81 (2009)
- [101] X. Chen, S. Yang, J. H. Kim, H. D. Kim, J.S. Kim, G. Rojas, R. Skomski, H. Lu, A. Bhattacharya, T. Santos, N. Guishinger, M. Bode, A. Gruverman, and A. Enders, *New J. Phys.* **12**, 083037 (2012)
- [102] B.J. Rodriguez, C. Callahan, S.V. Kalinin, and R. Proksch, *Nanotechnology* **18**, 475504 (2007)
- [103] W. F. Brinkman, R. C. Dynes, J. M. Rowell, *J. Appl. Phys.* **41**, 1915 (1970)
- [104] L.T. Hudson, R. L. Kurtz, S. W. Robey, D. Temple, and R. L. Stockbauer *Phys. Rev. B* **47**, 10832 (1993)
- [105] G. Ertl, and J. Küppers, VCH, Weinheim pp39 – 40 (1985)
- [106] S. Mróz, *Prog. Surf. Sci.* **46**, 377 (1994)
- [107] M. Cai, Y. Zhang, Z. Yin, and M. Zhang, *Phys. Rev. B* **72**, 075406 (2005)
- [108] R. Courths, *Phys. Stat. Sol. B* **100**, 135 (1980)
- [109] M. Bender, D. Ehrlich, I. N. Yakovkin, F. Rohr, M. Baumer, H. Kuhlenbeck, H-J Freund, and V. Staemmler, *J. Phys.: Condens. Matter* **7**, 5289 (1995)
- [110] F. Rohr, M. Baumer, H-J Freund, J. A. Mejias, V. Staemmler, S. Muller, L. Hammer, and K. Heinz, *Surf. Sci.* **372**, L291 (1997)
- [111] V. Maurice, S. Cadot, and P. Marcus, *Surf. Sci.* **458**, 195 (2000)
- [112] L. Zhang, M. Kuhn, and U. Diebold, *J. Vac. Sci. Technol. A*, **15**, 1576 (1997)

- [113] L. Zhang, M. Kuhn, and U. Diebold, *J. Vac. Sci. Technol. A*, **15**, 1576 (1997)
- [114] A. Maetaki, and K. Kishi, *Surf. Sci.* **411**, 35 (1998)
- [115] A. Maetaki, M. Yamamoto, H. Matsumoto, and K. Kishi, *Surf. Sci.* **445**, 80 (2000)
- [116] W.A.A. Priyantha, and G.D. Waddill, *Surf. Sci.* **578**, 149 (2005)
- [117] X.G. Wang, and J. R. Smith, *Phys. Rev. B* **68**, 201402 (2003)
- [118] A. Rohrbach, J. Hafner, and G. Kresse, *Phys. Rev. B* **70**, 125426 (2004)
- [119] O. Bikondoa, W. Moritz, X. Terrelles, H. J. Kim, G. Thornton, and R. Lindsay, *Phys. Rev. B* **81**, 205439 (2010)
- [120] A. L. Wysocki, S. Shi, and K. D. Belashchenko, *Phys. Rev. B* **86**, 165443 (2012)
- [121] L. Bocher, A. Gloter, A. Grasous, V. Garcia, K. March, A. Zobelli, S. Valencia, S. E. Vedrenne, X. Moya, N. D. Marthur, C. Deranlot, S. Fusil, K. Bouzehouane, M. Bibes, A. Barthelemy, C. Colliex, and O. Stephan, *Nano Lett.* **12**, 376 (2011)
- [122] H.L. Meyerheim, F. Klimenta, A. Ernst, K. Mohseni, S. Ostanin, M. Fechner, S. Parihar, I. V. Maznichenko, I. Mertig, and J. Kirschner, *Phys. Rev. Lett.* **106**, 087203 (2011)
- [123] A. Zenkvich, R. Mantovan, M. Fanciulli, M. Minnekaev, Y. Matveyev, Y. Lebedinshii, S. Thiess, and W. Drube, *Appl. Phys. Lett.* **99**, 182905 (2011)
- [124] A. Zenkvich, R. Mantovan, M. Fanciulli, M. Minnekaev, Y. Matveyev, Y. Lebedinshii, S. Thiess, and W. Drube, *Appl. Phys. Lett.* **99**, 182905 (2011)
- [125] P. Luches, M. Liberati, S. Valeri, *Surf. Sci.* **532**, 409 (2003)
- [126] R. Abrudan, J. Miguel, M. Bernien, C. Tieg, M. Piantek, J. Kirschner, and W. Kuch, *Phys. Rev. B* **77**, 014411 (2008)
- [127] J. H. Weaver, G. D. Waddill, *Science* **255**, 1444 (1991)

- [128] L. Huang, S. J. Chey, and J. H. Weaver, *Phy. Rev. Lett.* **80**, 4095 (1998)
- [129] J. Zhang, *Eur. Phys. J. D* **45**, 515 (2007)
- [130] P. Luches, M. Liberati, S. Valeri, *Surf. Sci.* **532**, 409 (2003)
- [131] T.J. Regan, H. Ohldag, C. Stamm, F. Nolting, J. Lüning, J. Sthör, and R. L. White, *Phy. Rev. B* **64**, 214422 (2001)
- [132] D. H. Kim, H. J. Lee, G. Kim, Y. S. Koo, J. H. Jung, H. J. Shin, J.-Y. Kim, and J.-S. Kang, *Phys. Rev. B* **79**, 033402 (2009)
- [133] C. T. Chen, Y. U. Idzerda, H.J. Lin, N. V. Smith, G. Meigs, E. Chaban, G. H. Ho, E. Pellegrin, and F. Sette, *Phys. Rev. Lett.* **75**, 152 (1995)
- [134] P. Bruno, *Phys. Rev. B* **39**, 865 (1989)
- [135] J. T. Lau, A. Föhlisch, R. Nietubyc, M. Reif, and W. Wurth, *Phys. Rev. Lett.* **89**, 057201 (2002)
- [136] C. Haley, J. H. Weaver, *Surf. Sci.* **518**, 243 (2002)
- [137] D. Sander, R. Skomski, C. Schmidthals, A. Enders, and J. Kirschner, *Phys. Rev. Lett.* **77**, 2566 (1996)
- [138] A. Enders, D. Peterka, D. Repetto, N. Lin, A. Dmitriev, and K. Kern, *Phys. Rev. Lett.* **90**, 21 (2003) 217203
- [139] A. Enders, D. Sander, and J. Kirschner, *J. Appl. Phys.* **85**, 5279 (1999)
- [140] D. Weller and T. McDaniel, in *Advanced Magnetic Nanostructures*, edited by D. Sellmyer and R. Skomski (Springer, Berlin, 2006), pp. 295–324.
- [141] S. Sun, C. B. Murray, D. Weller, L. Folks, and A. Moser, *Science* **287**, 1989 (2000).

- [142] K. Bromann, C. Felix, H. Brune, W. Harbich, R. Monot, J. Buttet, and K. Kern, *Science* **274**, 956 (1996).
- [143] J. V. Barth, G. Constantini, and K. Kern, *Nature* **437**, 671 (2005)
- [144] A. Enders, P. Gambardella, and K. Kern, in *The Handbook of Magnetism and Advanced Magnetic Materials*, Fundamentals and Theory Vol. 1, edited by H. Kronmüller and S. Parkin (Wiley, Chichester, UK, 2006), pp. 577–598
- [145] O. Fruchart, P.-O. Jubert, C. Meyer, M. Klaua, J. Barthel, and J. Kirschner, *J. Magn. Magn. Mater.* **239**, 224 (2002)
- [146] H. Brune, M. Giovannini, K. Bromann, and K. Kern, *Nature* **394**, 451 (1998)
- [147] J. A. Theobald, N. S. Oxtoby, M. A. Phillips, N. R. Champness, and P. H. Beton, *Nature* **424**, 1029 (2003)
- [148] W. Chen and A. T. S. Wee, *J. Phys. D* **40**, 6287 (2007)
- [149] J. H. Weaver and V. N. Antonov, *Surf. Sci.* **557**, 1 (2004)
- [150] G. Kerner and M. Asscher, *Surf. Sci.* **557**, 5 (2004)
- [151] S. Berner, M. Corso, R. Widmer, O. Groening, R. Laskowski, P. Blaha, K. Schwarz, A. Goriachko, H. Over, S. Gsell, M. Schreck, H. Sachdev, T. Greber, and J. Osterwalder, *Angew. Chem. Int. Ed.* **46**, 5115 (2007)
- [152] I. Brihuega, C. H. Michaelis, J. Zhang, S. Bose, V. Sessi, J. Honolka, M. A. Schneider, A. Enders, and K. Kern, *Surf. Sci.* **602**, L95 (2008)
- [153] R. Laskowski, P. Blaha, T. Gallauner, and K. H. Schwarz, *Phys. Rev. Lett.* **98**, 106802 (2007)
- [154] J. Zhang, V. Sessi, C. H. Michaelis, I. Brihuega, J. Honolka, and K. Kern, R. Skomski, X. Chen, G. Rojas, and A. Enders, *Phys. Rev. B.* **78** (2008) 165430

- [155] S. Brunauer and L. E. Copeland, in Handbook of Physics, edited by E. U. Condon and H. Odishaw (McGraw-Hill, New York, 1958), Pt. 5, Chap. 7